Evaluation of Porosity and Corrosion Protection Ability of Sol-Gel Deposited Oxide Thin Films on Magnesium

Vom Fachbereich Material- und Geowissenschaften

der Technischen Universität Darmstadt

zur Erlangung des akademischen Grades eines
Doctor rerum naturalium (Dr. rer. nat.)
genehmigte

Dissertation

eingereicht von
Mehdi Yekehtaz, M. Sc.
aus Tehran (Iran)

Referent:	Prof. Dr. rer. nat. Wolfgang Ensinger
Korreferent:	Prof. Dr. -Ing. Clemens Müller
Tag der Einreichung:	27.08.2010
Tag der mündlichen Prüfung:	08.10.2010

Darmstadt 2010

D17

Dedicated to

My Loving Family

Acknowledgement

First and foremost I would like to express my deepest gratitude to my supervisor Prof. Dr. Wolfgang Ensinger whose sincere and valuable guidance helped me in bringing this thesis work to a successful completion. I am particularly grateful for the degree of freedom he left me.

I would like to thank Prof. C. Müller for accepting to be the second referee of this work.

This work could not have been carried out without the help and support of Dr. Falk Sittner who initially introduced me to the field of corrosion and for his always availability to discuss any problem related to research work.

I am grateful for the assistance provided by: Dr. Stefan Flege for SIMS measurements, Dr. Joachim Brötz for XRD measurements, Dr. Sigrid Benfer from DECHEMA e.v. for her scientific comments and reviewing my thesis, Dr. Christian Schmitt for his helpful discussion about the XRD results and Mr. Mouner A. Abdalslam for his helpful discussion about the impedance results.

Many thanks go to all my colleagues in Materialanalytik Group for fine and warm working atmosphere.

At this moment I wish to acknowledge the blessings and good wishes of my family members. My biggest and deepest gratitude goes to my mother for her constant inspiration, support and encouragement. I am always indebted to my brother, Mohammad, who is always a source of strength and courage for me and helped me in any manner. I would like to express my gratitude to my brother and sisters whom their supports helped me along the way. Without you, I would not have been able to go through all this.

Finally, I wish to express my gratitude to my love, Raheleh, who made the years of PhD work much nicer, supporting me to overcome any emerging task.

Abstract

Some valuable properties of magnesium like high strength-to-weight ratio, high thermal conductivity, good electromagnetic shielding and machinability have made it an excellent material for various applications in automobile and aerospace components, sporting goods and household equipments. Despite of these valuable properties, poor corrosion and wear resistance restrict its application. The deposition of a protective film acting as a barrier between the material and its environment is an effective solution to preserve the metal from a corrosive attack. Good adhesion, uniformity and freedom from defects are necessary properties to ensure a good protection performance. Sol–gel deposition can provide ceramic-like films with high density and hardness at very low temperatures in a fast and inexpensive way. The low reaction temperature and the mixture of organic and inorganic materials lead to the formation of coatings containing both inorganic and organic moieties. The inorganic component enhances hardness, durability and adhesion to the metal substrate while the organic component leads to an increased flexibility and density. The major challenge of sol–gel deposited films is the prevention of pinholes and open porosities arising from the deposition process. Local porosities can produce direct paths between the corrosive environment and the substrate and increase the susceptibility of the materials to corrode. Despite of huge effort on resolving of this drawback, there is still no systematical manner to overcome this problem.

In this work, several thin films obtained from sol-gel solutions containing silicon and zirconium were deposited on magnesium samples. Effect of sol solution parameters such as the amount of catalyst, stabilizing agent, water, co-solvent and heat treatment temperature on the porosity of the final film was investigated. Electrochemical methods such as potentiodynamic scans and electrochemical impedance spectroscopy were applied. It was shown that along with other parameters, the structure of precursor also plays an important role on the porous nature of the resulting film. It was also shown that these films are able to increase the corrosion resistance of magnesium in several environments. Film characterization methods proved the formation of an inter-diffusion

layer between substrate and the coating which could be responsible for corrosion resistance enhancement.

Zusammenfassung

Viele nützliche Eigenschaften von Magnesium, wie dessen hohes Zugfestigkeits/Gewicht Verhältnis, seine hohe thermische Leitfähigkeit und die gute elektromagnetische Abschirmeigenschaft sowie dessen sehr gute Verarbeitungsmöglichkeiten, machen es zu einem exzellenten Material für unterschiedlichste Anwendungen in der Luft- und Raumfahrt und bei Automobilkomponenten, Sportartikeln sowie Haushaltsprodukten. Trotz dieser wertvollen Eigenschaften schränken sein schlechtes Korrosionsverhalten und seine geringe Verschleißfestigkeit dessen Anwendung ein. Die Abscheidung einer schützenden Schicht, die als Sperre zwischen dem Material und seiner Umgebung dient, ist eine wirkungsvolle Lösung, um das Metall vor einem korrosiven Angriff zu schützen. Gute Adhäsion, Gleichförmigkeit und Defektfreiheit sind die notwendigen Eigenschaften, um einen guten Schutz zu gewährleisten. Sol-Gel-Abscheidung ermöglicht keramikähnliche Schichten mit hoher Dichte und Härte bei sehr niedrigen Temperaturen in einer schnellen und kostengünstigen Weise. Die niedrige Reaktionstemperatur und die Mischung organischer und anorganischer Materialien führen zur Anordnung von Schichten, welche anorganische und organische Anteile enthalten. Der anorganische Bestandteil erhöht die Härte, Haltbarkeit und Adhäsion zum Metallsubstrat, während der organische zu einer erhöhten Flexibilität und Dichte führt. Die Hauptherausforderung der mittels Sol-Gel abgeschiedenen Schichten ist die Entstehung von Löchern und offenen Poren zu verhindern, welche durch den Abscheidungsprozess entstehen. Lokale Porosität kann direkte Wege zwischen der korrosiven Umgebung und dem Substrat erzeugen und die Anfälligkeit der Materialien erhöhen. Trotz der sehr großen Bemühung, diese Beeinträchtigung zu beheben, wurde noch keine Systematik erarbeitet, dieses Problem zu überwinden. In dieser Arbeit wurden dünne Schichten, bestehend aus Silizium und Zirkonium, mittels Sol-Gel-Lösungen auf Magnesiumproben abgeschieden. Der Einfluss unterschiedlicher Parameter der Sol-Gel-Lösung, wie die Menge des Katalysators, des Stabilisierungsmittels, des Wassers, des Ko-Lösungsmittels und der Sintertemperatur auf die Porosität des abgeschiedenen Films wurde untersucht. Elektrochemische Methoden wie potentiostatische Scans und elektrochemische Impendanzspektroskopie wurden angewendet.

Es wurde gezeigt, dass zusammen mit anderen Parametern die Struktur des Precursors eine wichtige Rolle für die Porosität des resultierenden Filmes spielt. Es wurde nachgewiesen, dass diese Filme in der Lage sind, die Korrosionsbeständigkeit des Magnesiums in einigen Umgebungen zu erhöhen. Schichtcharaktersierende Methoden belegten die Ausbildung einer Zwischendiffusionsschicht zwischen Substrat und der Schicht, welche für die Verbesserung der Korrosionsbeständigkeit verantwortlich sein könnte.

Table of Contents

Table of Figures

List of Tables

1. Introduction and Motivation

Magnesium is the 8th most abundant element on earth making up approximately 1.93% mass of the earth's crust and 0.13% mass of the oceans. [1] Some properties of magnesium such as high strength-to-weight ratio, high thermal conductivity, high dimensional stability, good electromagnetic shielding and good machinability have made it valuable in a number of applications including automobile and computer parts, aerospace components, mobile phones, sporting goods, handheld tools and household equipment. [2] Although the discovery of magnesium was credited to Sir H. Davy as long ago as 1808, it was only in the 20th century that the metal was produced in significant industrial quantities. From a total of only ~10 t y^{-1} at the beginning of the last century, production increased with many fluctuations to ~400 kt y^{-1} in 2000. Despite of all these properties, high chemical reactivity of magnesium has restricted its application in many areas. Owing to the low standard electrode potential, magnesium is one of the most reactive metals. It will readily form a galvanic corrosion system with another metal in an aqueous environment.

The deposition of a protective film is an effective solution to protect the metal from a corrosive attack. Coatings can protect a substrate providing a barrier between the metal and its environment and/or through the presence of corrosion inhibiting chemicals in them. In order for a coating to provide adequate corrosion protection, the coating must be uniform, well adherent and pore free. Different coating methods have been applied on magnesium and its alloys such as electrochemical plating, [3-4] chemical conversion, [5-6] anodizing [7-8] and chemical and physical vapor deposition. [9-10] All these methods have their own advantages and drawbacks. Sol-gel method is one of the most promising methods to achieve this purpose. The sol–gel deposition can provide chemically stable ceramic-like films with high density and hardness at very low temperatures in a fast and inexpensive way. The low reaction temperature and the mixture of organic and inorganic materials lead to the formation of coatings containing both inorganic and organic moieties. [11-13] The inorganic component enhances hardness, durability and adhesion to the metal substrate while the organic component leads to an increased flexibility and density.

The major challenge of sol–gel deposited protective films is the prevention of pinholes and open porosities arising from the deposition process. [14-16] These porosities can produce direct paths between the corrosive environment and the substrate which in turn results in an increase of the corrosion rate of the substrate.

In sol-gel process, several parameters such as the type of catalysts, stabilizing agent, water content and heat treatment temperature can affect the porous nature of the final deposited film. The goal of this work is to find a systematic procedure on sol-gel process to reduce the porosity of the film for protection purposes.

2. Magnesium and Corrosion

2.1 Properties of Magnesium:

The need for fuel efficiency and increased performance in transportation systems continually places new demands on the materials used. For transportation purposes, material has to meet several criteria including density, strength, stiffness and corrosion resistance. Magnesium which was firstly produced by Humphrey Davy in 1808 and its alloys are a promising alternative to aluminum alloys currently dominating the transportation industry. The density of magnesium is 35 % lower than that of aluminum and typical magnesium alloy weigh approximately 25 % less than their aluminum counterparts at equal stiffness. Another important advantage of magnesium is the high strength attainable through proper alloying, leading to the high strength/weight ratio desirable for transportation applications. Key features influencing the development and use of magnesium as a structural metal is the atomic diameter of magnesium (0.32 nm) which allows its combination with a wide range of solute elements such as aluminum, zirconium, zinc, silver and cerium. [17] The limited use of magnesium in engineering applications results mainly from the shortcoming of its corrosion properties. Magnesium dissolution in aqueous environment generally proceeds by electrochemical reaction with water to produce magnesium hydroxide and hydrogen gas: [18]

Anodic Reaction: $Mg \longrightarrow Mg^{2+} + 2\,e^-$

Cathodic reaction: $2\,H_2O + 2\,e^- \longrightarrow H_2 + 2\,OH^-$

Product Formation: $Mg^{2+} + 2\,OH^- \longrightarrow Mg\,(OH)_2$

The overall reaction is:

$$Mg + 2\,H_2O \longrightarrow Mg(OH)_2 + H_2$$

As corrosion proceeds, the metal surface experiences a local pH increase due to the formation of $Mg(OH)_2$ film, whose equilibrium pH is about 11. This film can thus protect magnesium in alkaline environments and poorly buffered solution where the surface pH can increase. Presence of anion such as chloride, sulphate and nitrate and impurities will destroy this film and increase the corrosion rate of magnesium.

2.2 Thermodynamics:

In spite of the standard reduction potential of magnesium (-2.4 V vs. normal hydrogen electrode, NHE), the open circuit potential of magnesium in neutral aqueous environment falls below -1.5 V. In aqueous solution magnesium forms magnesium hydroxide film (or probably magnesium oxide) unless the pH is kept higher than 11. Formation of this protective film results in the difference between standard and open circuit potential of magnesium. Several structures have been suggested for this film on magnesium.

The thermodynamics that governs the formation of this protective film can be conveniently described by Pourbaix diagram. Pourbaix and his coworkers [19,20] have shown that plotting electrode potentials of electrochemical reactions against pH can be applied in identifying regions of stability of various chemical species in solution. They have expressed the possible phases of Metal/H_2O system at 298 K at equilibrium in the form of diagrams which provide a thermodynamic basis for the study of corrosion reactions. They showed that depending on the acidity of the environment (pH) and the activity of the species involved in the corrosion reaction, different situations can be observed. Three different zones are recognizable in Pourbaix diagrams:

- Corrosion, where a soluble corrosion products exits. Pourbaix has defined a concentration of 10^{-6} M as a lower threshold. Higher concentration indicates the susceptibility of the system toward the corrosion process.
- Passivation, when an insoluble oxide or hydroxide is formed on the metal surface. In this area, the metal tends to become coated with an oxide or hydroxide layer which provides corrosion resistance against the environment.

- Immunity, where the concentration of metal ions is less than 10^{-6} M. In this region the metal is considered to be totally immune from corrosion attack and safe to use.

The Pourbaix diagram of magnesium is shown in Figure 2.1. [21]

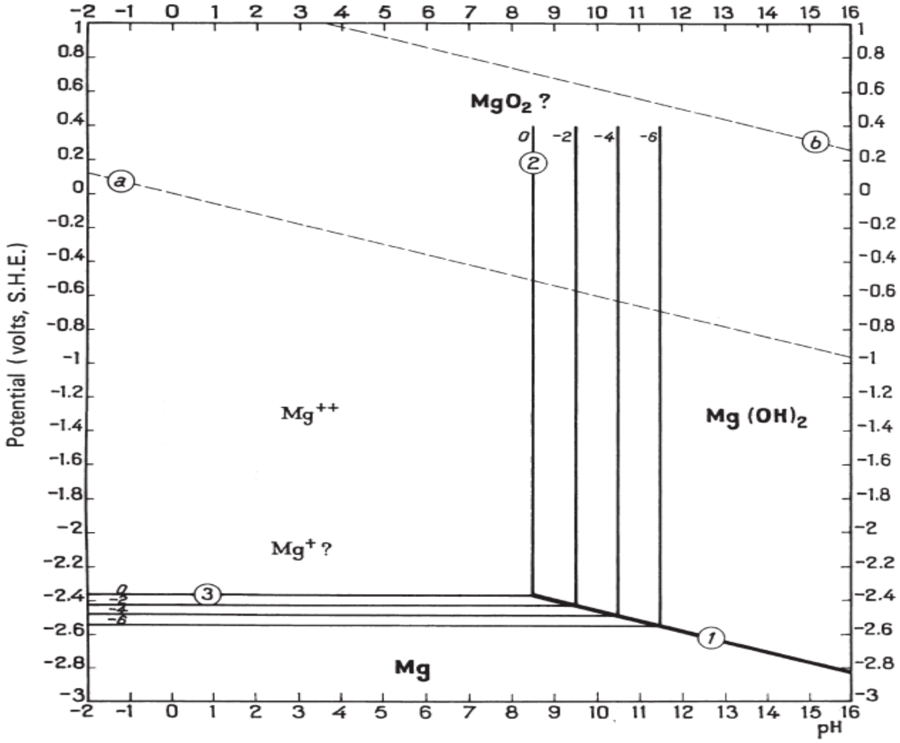

Figure 2.1: Pourbaix diagram for magnesium-water system at 25° C

The lines with the ringed numbers correspond to the following reactions between magnesium and H_2O at 25° C:

1) $Mg + H_2O \xrightarrow{-H_2} MgO$

2) $Mg^{2+} + H_2O \longrightarrow MgO + 2\,H^+$

3) $Mg \longrightarrow Mg^{2+} + 2\,e^-$

Equation 1 and 2 show the formation of MgO even though the diagram given by Pourbaix indicate the formation of $Mg(OH)_2$. Pourbaix points out that this is so because $Mg(OH)_2$ is thermodynamically more stable than MgO in presence of water. The horizontal and vertical lines of 3 and 2 give the concentration of magnesium as a power of 10. As shown in Figure, the ringed number lines separate the regions of corrosion (dissolved cation, Mg^{2+}), immunity (unreacted metal) and passivation (corrosion products, $Mg(OH)_2$). Further investigation by Perrault resulted in the development of a theoretical potential-pH diagrams which are able to provide a much better fit to the value of the rest potential of magnesium anode (Figure 2.2). [22]

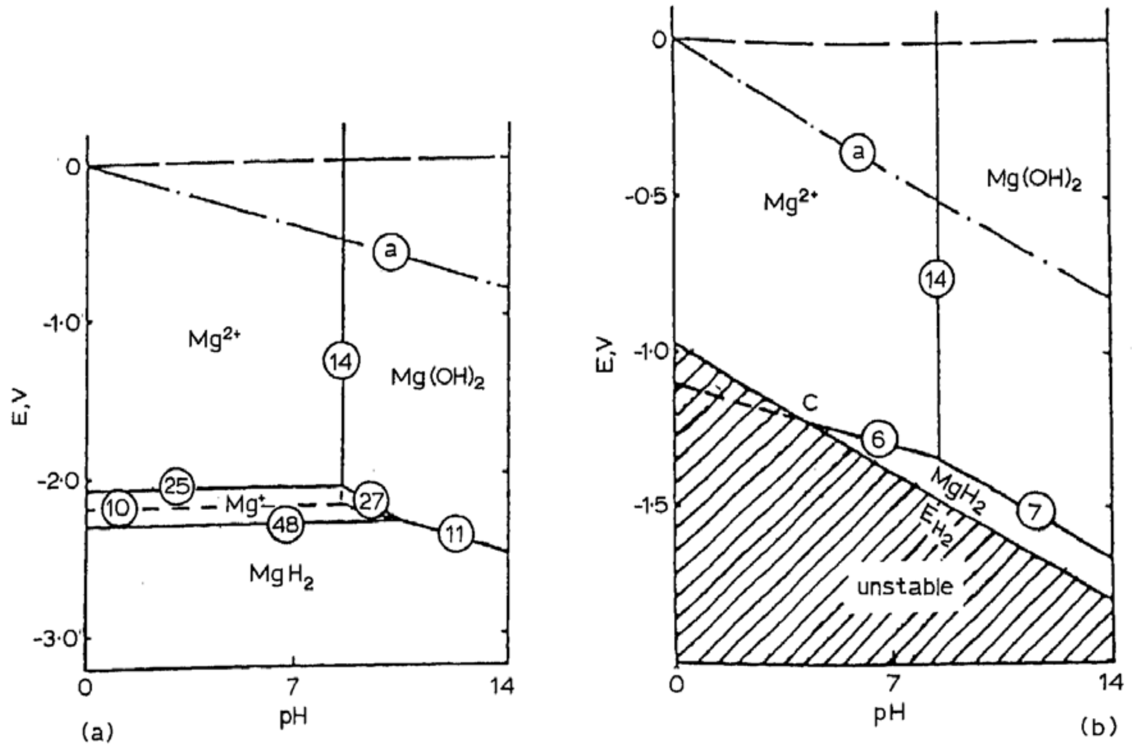

Figure 2.2: a) equilibrium of Mg-H_2O system in presence of H_2 molecules and b) stability domains of magnesium compounds in aqueous solution with hydrogen overpotential of 1 V

Perrault pointed out that Pourbaix diagram could not provide the correct rest potential value because Pourbaix did not have the thermodynamic data of magnesium hydride and monovalent magnesium ion (shown in Figure 2.1 with a question mark). Taking into consideration the formation of MgH_2 and Mg^+, Perrault concluded that a thermodynamic equilibrium cannot exist for a magnesium electrode in contact with aqueous solution unless the hydrogen overpotential is about 1 V and the pH is greater than 5. The ringed number in Figure 2.2 corresponds to the following reactions:

6) $MgH_2 \longrightarrow Mg^{2+} + 2\ H^+ + 4\ e^-$

7) $MgH_2 + 2\ OH^- \longrightarrow Mg(OH)_2 + 2\ H^+ + 4\ e^-$

10) $MgH_2 \longrightarrow Mg^{2+} + H_2 + 2\ e^-$

11) $MgH_2 + 2\ OH^- \longrightarrow Mg(OH)_2 + H_2 + 2\ e^-$

14) $Mg^{2+} + 2\ OH^- \longrightarrow Mg(OH)_2$

25) $Mg^+ \longrightarrow Mg^{2+} + e^-$

27) $Mg^{2+} + 2\ OH^- \longrightarrow Mg(OH)_2 + 2\ e^-$

$Mg^+ + 2\ H_2O \longrightarrow Mg(OH)_2 + 2\ H^+ + e^-$

48) $MgH_2 \longrightarrow Mg^+ + H_2 + e^-$

2.3 Kinetics:

Like most metals and alloys, magnesium corrosion is governed by the characteristic of its surface film. This film is crucial in controlling the kinetics of corrosion and its nature determines the effectiveness of this control. A good passive film improves corrosion resistance by reducing the cation flow out or anion flow in, providing resistance to breakdown by aggressive species or promoting rapid repair of a damaged film. The nature of this quasi-passive film on magnesium is not fully understood but as predicted by the thermodynamic calculations, it is believed to be composed mainly of $Mg(OH)_2$. Ono [23] suggested a three layers film structure on magnesium with a hydrated inner layer closest to the magnesium metal, a thin and dense middle layer and a porous outer zone. Jones et al [24] suggested the formation of a $Mg(OH)_2$-like layer which differs slightly from bulk $Mg(OH)_2$ and acts as an electrical insulator to protect magnesium. Frühwirth et al [25] also suggested that an initial layer of MgO is quickly replaced by the more stable hydroxide, because MgO inherently lacks the qualities of hardness and insolubility.

Hydrogen reduction and its overpotential also play an important role in magnesium corrosion because low overvoltage facilitates corrosion. Overpotential can be defined as a displacement of an electrode from its equilibrium value due to the applying of an external potential. In an electrochemical system, the total overpotential amount can be obtained as sum of three separate overpotentials:

$$\eta_{total} = \eta_{act} + \eta_{conc} + iR$$

Where η_{act} is the activation overpotential, η_{conc} is the concentration overpotential and iR is the Ohmic drop.

2.3.1 Activation Overpotential:

This overpotential shows the ability of the reactant to overcome the energy barrier of its lattice and move toward the solution. An important example of this type is the evolution of hydrogen gas during the corrosion process which proceeds in two steps:

1. Reduction of the hydrogen ions results in the formation of atomic hydrogen on the cathode surface:

$$H^+ + e^- \longrightarrow H_{ads}$$

2. Combination of atoms to molecules of gaseous hydrogen:

$$2\,H_{ads} \longrightarrow H_2$$

The rate of this reaction depends on several factors including the rate of electron transfer from metal to hydrogen ions. As a result, the rate of hydrogen evolution from different metal surfaces can vary greatly. The exchange current density, i_0, is an important parameter in electrochemical kinetics that explains the difference of hydrogen production rate on different metal surfaces.

2.3.2 Concentration Overpotential:

Concentration polarization is the polarization component which is caused by a concentration gradient in the solution near to the metal/electrolyte interface as illustrated in Fig. 2.3 in which the concentration of dissolved oxygen limits the cathodic reaction rate. [26]

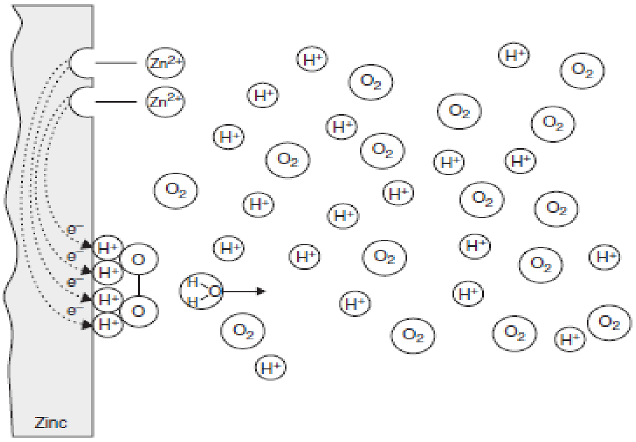

Figure 2.3: Schematic presentation of concentration polarization in the vicinity of an electrode

In this situation the mass transport of species to the surface controls the rate of the corrosion. As shown in Figure 2.4, the mass transport is governed by three different forces which are diffusion, migration and convection. [26]

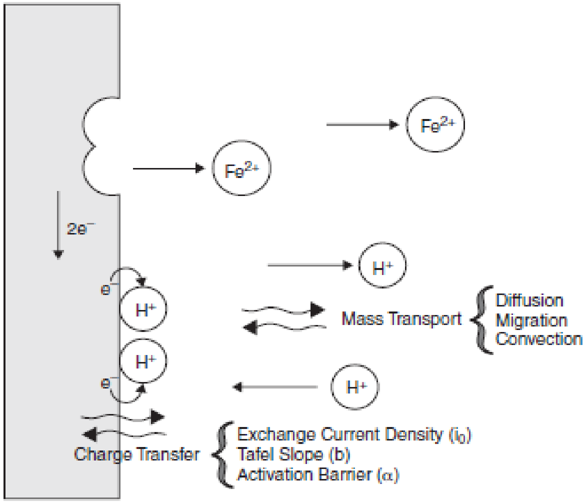

Figure 2.4: Graphical representation of the processes on the metallic surface

2.3.3 Ohmic Overpotential:

This overpotential is a simple product of a resistance and a current between the anodic and cathodic sites of a corrosion process. The resistance overpotential can be expressed as:

$$\eta_R = I(R_{sol.} + R_f)$$

where $R_{sol.}$ is the resistance of the solution and R_f is the resistance of the film or coating formed on the surface of the substrate.

Activation overpotential is the controlling factor in corrosion of metals in strong acids while the concentration overpotential dominates on corrosion rate when the concentration of active species is limiting the corrosion rate e.g. at dilute acids. When there is a separation between the anodic and cathodic sites, ohmic drop plays an extremely important role in the studying of corrosion phenomena.

The kinetic of an electrode reaction can be explained by the well known Butler-Volmer equation for polarizing an electrode from the open circuit potential under steady-state conditions:

$$i = i_0 \left\{ \exp\left[\beta \frac{zF}{RT} \eta \right]_a - \exp\left[-(1-\beta) \frac{zF}{RT} \eta \right]_c \right\}$$

In this equation i_0 is the exchange current density at equilibrium and β is the symmetry coefficient (→ 0.5). The first term in the equation shows the forward (metal dissolution, anodic) reaction whereas the seconds term describes the backward (metal deposition, cathodic) reaction. Figure 2.5 shows a schematic current-potential curve of a redox system at β = 0.5.[27]

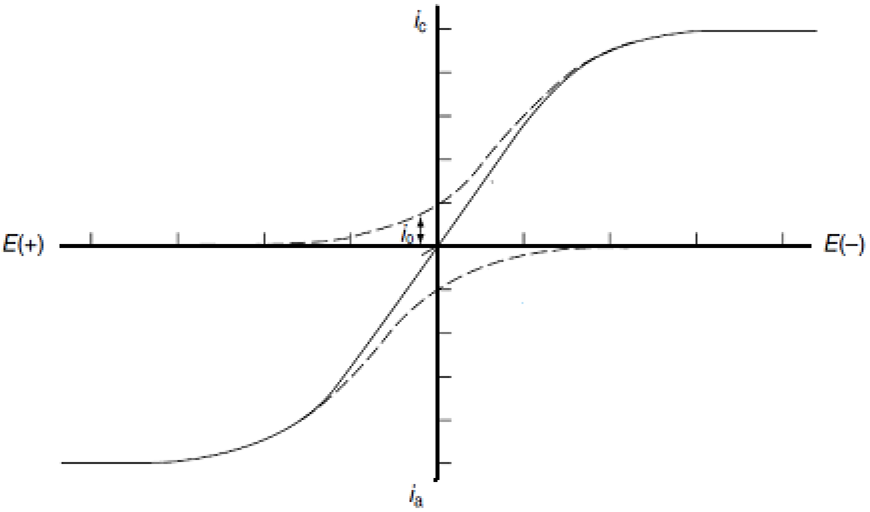

Figure 2.5: A schematic plot of current-potential curve for a redox system at β = 0.5

At sufficiently high overpotential, one of the exponential terms in Butler-Volmer equation is negligible. For example for metal dissolution ($i_a >> i_c$):

$$i_a = i_0 \exp\left(-\beta \frac{zF}{RT} \eta_a \right)$$

Logarithm of this equation results in the Tafel equation:

$$\ln i_a = \ln i_0 - \beta \frac{zF}{RT} \eta_a$$

According to this equation, the anodic and cathodic Tafel amount can be calculated by:

$$b_a = \frac{2.303RT}{\beta zF} \qquad b_c = -\frac{2.303RT}{(1-\beta)zF}$$

The corrosion current can then be calculated by Stern-Geary equation using anodic and cathodic Tafel slopes: [28]

$$I_{corr} = \frac{1}{2.303R} \left(\frac{b_c b_a}{b_c + b_a} \right)$$

The corrosion current density may then be combined with Faraday's law:

$$W = \frac{A_w Q}{zF}$$

where W is the mass of material removed, A_w is the atomic weight of the sample, Q is the total charge passed through the system and z is the number of electron transferred in the reaction. The corrosion rate can be calculated by:

$$\text{Corrosion Rate} = W * SA / \rho$$

Where SA is the exposed surface area and ρ is the density of the sample.

2.4 Corrosion Types:

2.4.1 Galvanic Corrosion:

Magnesium and magnesium alloys are highly susceptible to galvanic corrosion. Galvanic corrosion or dissimilar metal corrosion refers to the corrosion damage induced by the contact between two metals or conductors with different potentials. In the electrochemical series of elements, magnesium is found near to the top which means all structural metals are cathodic towards magnesium and lead to the magnesium corrosion. According to Ohm’s law, the galvanic corrosion current can be expressed by:

$$I_{corr} = \frac{\left(E_{p-c} - E_{p-Mg}\right)}{\left(R_e + R_m\right)}$$

E_{p-c} and E_{p-Mg} are the polarized potentials for the cathode material and the magnesium, R_e is the electrolyte resistance and R_m is the resistance in the metal-metal contact between anode and cathode. According to the equation above, galvanic corrosion current can be minimized by either minimizing the potential difference between magnesium and the cathode or maximizing the resistance of the circuit. Metals with low hydrogen overvoltage such as copper, nickel, and iron results in the severe galvanic corrosion of magnesium. Conversely, metals with high hydrogen overvoltage are much less damaging.

2.4.2 Pitting Corrosion:

Magnesium undergoes pitting corrosion in the presence of chloride ions in non-oxidizing media. [29] Pitting corrosion is the most common type of localized corrosion in which pits form from dissolution of the specific areas of the material surface. The initiation of pits starts at defects of the passive film such as pores and scratches which are anodic compared to their vicinity and result in the dissolution of metal. As shown in Figure 2.6, active metal immersed in oxygenated solution of NaCl dissolves inside the pits. [30] The positive charges of dissolved cations attract the negative chloride ions from the solution which result in the formation of metal chloride. Hydrolysis of this compound in the pits accelerates the metal dissolution and pitting process by formation of chloride ions:

$$M^{+}_{(aq)} + Cl^{-}_{(aq)} \longrightarrow MCl$$

$$MCl + H_2O \longrightarrow M^{+}_{(aq)} + Cl^{-}_{(aq)}$$

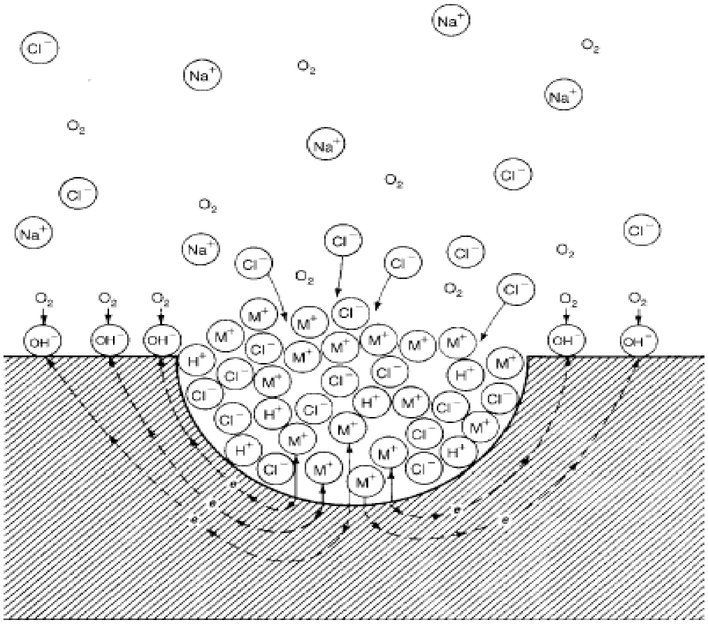

Figure 2.6: Mechanism of pitting corrosion

2.4.3 Stress Corrosion Cracking (SCC):

SCC is a mechanical-chemical process which leads to the formation of cracks on certain alloys at stresses below their tensile strength. The driving force of this type of corrosion is related to the potential difference between the grain boundaries and the bulk material. Pure magnesium can be considered immune to stress corrosion cracking (SCC) in both atmospheric and aqueous environments. The addition of Al and Zn promote SCC on magnesium alloys whereas alloys containing zirconium are free from SCC. [31] In alkaline media with a pH above 10.2, magnesium alloys appear to be very resistant against SCC.

2.5 Corrosion Protection:

Corrosion prevention of a base material can be achieved by either the modification of the surface through chemical or physical methods or by applying additives to the environment to slow down the corrosion reactions. Deposition of a protective thin film on the substrate in order to isolate the material from its environment is one of the most successful methods for this purpose. Several methods have been applied on magnesium and its alloys in order to enhance their resistance against corrosion.

2.5.1 Anodic Oxidation:

Anodizing is an electrolytic process to produce a thick oxide layer on metals and alloys. The film consists of a thin barrier layer at the metal-coating interface which is followed by a cellular structure layer. The pore size of this layer is determined by the type of electrolyte and its concentration, temperature and applied voltage. [32] Increasing the magnesium resistance by anodization was given firstly by Huber in 1953 [33] who investigated the relationship between the applied voltage and the characteristics of a film formed on Mg in 1 M NaOH. He showed that at voltage up to 3 V, the current density remained low and a light grey protective film of $Mg(OH)_2$ formed. At intermediate voltages, i.e. 3–20 V, oxygen was evolved, and a thick dark film of $Mg(OH)_2$ was found.

Above 20 V, a thin protective coating was again produced. The formation of a compact anodic film was shown to be limited by the breakdown phenomenon accompanied by intensive sparking (above 50 V). Khaselev and Yahalom [34-35] found that four different regions of anodic potentials can be distinguished on the polarization curves of magnesium: primary passivity; breakdown of primary passivity and metal dissolution; secondary passivity; and the breakdown of the secondary passivity. They showed that the process parameters, the electrolyte composition and the substrate can also influence the corrosion properties of magnesium.

2.5.2 Conversion Coating:

In this process, a part of the metal is converted to a coating to enhance its resistance against corrosion. Conversion coatings produced by chemical or electrochemical treatment of the surface, are superficial layers of metal oxides, chromates or other compounds that are chemically bonded to the surface. [36] This method can be used for several purposes such as corrosion protection, surface hardening and as paint primers. Conventional conversion coatings are based on chromate compounds. In this process, the dissolution of the metal surface with a corresponding reduction of water or oxygen to form a hydroxyl ion causes an increase of the pH of liquid-metal interface which in turn causes the precipitation of a thin complex chromium-metal gel on the surface that contains both hexavalent and trivalent chromium compounds. [37] Phosphate/permanganate and flourozirconate treatments are also used as an alternative to conventional chromate conversion coatings and have been shown to provide corrosion resistance comparable to chromate treatments. [38] Chen et al [39] used tannic acid based conversion coating to provide a dense coating on AZ91. They showed that the main component consists of penta-hydroxy benzamide-magnesium complex, MgF_2 and Al_2O_3 which provide good protection on magnesium AZ91 by producing less current density compared to the bare material. Montemor et al [40] applied two conversion baths consisting of cerium nitrate and lanthanum nitrate solutions on magnesium alloy AZ31 and examined their ability on corrosion protection. They concluded that for cerium nitrate, the thickness of the film is time-dependent whereas for lanthanum nitrate, it was independent on immersion time.

The Phytic acid (PA) conversion coating on AZ61 magnesium alloy was prepared by Pan et al. [41] using immersion-deposition methode. They showed that the formation process is critically dependent on the pH, time and PA concentration and is able to enhance the corrosion resistance of the substrate by positively shifting of the corrosion potential.

2.5.3 Gas Phase Deposition:

In these methods, a thin layer of a protective material is deposited onto the substrate in dimension of atomic scale by e.g. evaporation or sputtering. In evaporation, atoms are removed from the source by heating, whereas in sputtering they are dislodged from a solid target (source) surfaces through impact of gaseous ions. In chemical vapor deposition (CVD), the substrate is exposed to one or more volatile precursors which react with the substrate to produce the desired film. Ability of gas phase deposition methods to enhance corrosion resistance of magnesium and its alloys also investigated by several researchers. Altun et al. [42] investigated the corrosion properties of different magnesium alloys coated by physical vapor deposition (PVD) technique of DC magnetron sputtering. Using several methods such as potentiodynamic polarization diagrams, XRD patterns and SEM micrographs, they showed that this layer is capable of increasing the corrosion resistance of magnesium alloys. In other study, Wu et al. [43] studied the corrosion behavior of ceramic PVD films on magnesium AZ31 alloy with TiO_2 and Al_2O_3 as donors. They showed that the presence of amorphous TiO_x and AlO_x can provide good resistance in NaCl solution with better protection in the case of TiO_x due to the better adhesion. They also used magnetron sputtering to prepare aluminum coating on a mechanically polished AZ31 magnesium alloy and found that a loose oxide film was spontaneously formed on the surface during polishing process and the Al coating grown on this oxide layer had a developed columnar microstructure. The Al coated AZ31 showed a higher corrosion resistance than bare AZ31 in corrosion tests, which was mainly due to the barrier effect of Al coating. [44]

2.5.4 Liquid Phase Deposition:

Another widely used protective coating on magnesium and alloys are organic protective coatings. Organic coatings are a complex mixture of chemical substances that can be divided into four different categories: binders (resins), volatile components, pigments and additives. Binders are materials which form a continuous film onto the substrate and bind the other substances together in the coating. Volatile components are liquids that make the coating fluid enough for application and evaporate during and after application. Pigments are finely divided insoluble solid particles that remain suspended in the binder after film formation. Additives are materials that are included in small quantities to modify some property of a coating. Organic coatings can include a variety of processes such as painting, E-coating (cathodic epoxy electrocoating), powder coating and sol-gel deposition. Paints are a mixture of insoluble particles of pigment suspended in a continuous organic or aqueous vehicle.

E-coating or cathodic epoxy electrocoating is a process for painting metal surfaces by charging the metal part negatively and submerging it in a tank which contains positively charged paint. [45] In powder coating a pigmented resinous coating powder is applied to the substrate and then heated to fuse the particles together in a uniform, pine-hole free film. [46] Sol-gel deposition is based on the hydrolysis and condensation of metal alkoxides. The resulting oxide materials vary in range from nanoparticulate sols to continuous polymer gels with different compositions in the form of glasses, fibers, ceramic powders and thin films. The low reaction temperature and the mixture of organic and inorganic materials lead to a new class of coatings containing both inorganic and organic moieties. [47] The inorganic component enhances hardness, durability and adhesion to the metal substrate whereas the organic component leads to an increased flexibility and density. Other key properties are compatibility and adhesion of thin protective hybrid sol–gel films to the top organic paint systems. Chemical bonding is possible between the sol–gel film and the top coat conferring enhanced adhesion in comparison to chromate pre-treatments where adhesion is based on mechanical interlocking, dispersion forces and hydrogen bonds. Figure 2.7 depicts possible ways to obtain an enhanced chemical compatibility of an epoxy-based or amino-containing paint system to a sol–gel pretreatment by functionalizing the organic component of the hybrid film with epoxy groups. [48]

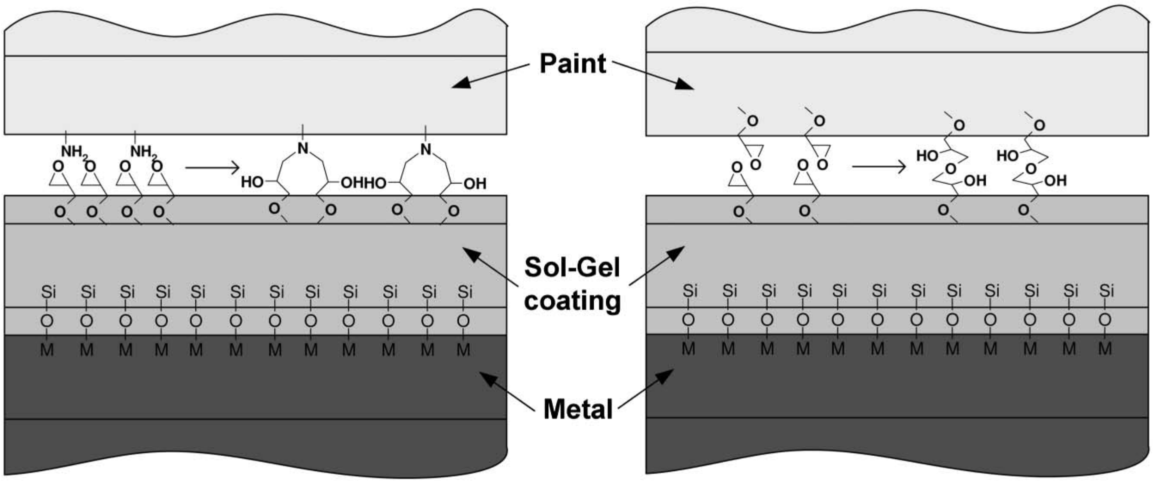

Figure 2.7: Schematic representation of enhanced compatibility of different paint systems with an epoxy-functional hybrid sol–gel coating

Corrosion resistance of magnesium alloy AZ91 was studied by applying a two layer painting consisting of epoxy resin as a first layer and acrylic resin layer as a second layer.[49] The paint coated surfaces showed to have corrosion resistance after 4000 h salt spray testing and a 3-year atmospheric exposure test there revealed no signs of blisters or corrosion. Phani et al. [50] deposited a layer of ZrO_2 sol with and without cerium particles on magnesium AZ91 and AZ31 alloys. The thin film deposited on alloys by dip coating method and sample annealed at different temperature to obtain dense and homogenous thin film. Corrosion resistance of alloys was investigated by salt spray experiments for 96 hours and they showed that the deposited films increase their corrosion resistance. Li et al. [51] used zirconium acetate as a precursor for sol-gel deposition on magnesium AZ91 after chemical pretreatment by stannate conversion coating. Ability of film was investigated by electrochemical methods in 3.5 % NaCl solution. They showed that the ceramic film consists mainly of tetragonal phase ZrO_2 which acts as a good barrier to suppress the corrosion of magnesium AZ91. In another investigation by Li et al. [52] a thin film of cerium oxide/titanium oxide was deposited on magnesium alloy AZ91 by sol-gel method. The electrochemical measurement in 3.5 % NaCl showed a shift of corrosion potential of 150 mV in anodic direction compared to bare material which is attributed to the corrosion resistance of the deposited film.

Simplicity of the sol-gel method compared to the other coating methods with economic impact has spread its application for deposition of thin films in nanometer scales. The main challenge in this method arises from the porous nature of the sol-gel films. These porosities can provide direct paths between the environment and the substrate which result in increasing the corrosion rate of the substrate. It can be supposed that reducing the porosity of the film will result in better protection of the substrate against corrosion because less porous film will act as better barrier against electrolyte diffusion. In this work, effect of several parameters on the porosity of the sol-gel films has been investigated by means of electrochemical methods.

2.6 Electrochemical Methods:

Porosity evaluation of the film can be investigated using several methods. Among them, electrochemical methods have been widely used for this purpose. [15-16] evaluation can be done either by comparison of the polarization resistance of bare and coated substrate or by potential concept in which current densities of bare and coated material can be used. In this case using higher scan rates and a mild environment avoid any unnecessary damage to the coating.

Electrochemical methods have been widely used to investigate the mechanisms of corrosion processes. These methods are able to provide useful information about the corrosion mechanisms, corrosion rate and susceptibility of specific materials to corrosion in designated environments. A typical electrochemical experiment comprises an electrochemical cell containing the electrolyte, a reference electrode, an auxiliary and a working electrode of the metal under test. When a metal is immersed in the electrolyte in the absence of an external current, the obtained potential is called the open circuit potential (OCP). This potential can provide valuable information about the potential distribution of the corroding surface, the starting point for application of suitable electrochemical method and controlling the protection potential during electrochemical experiments. Changing the potential of the corroding metal from its equilibrium potential value, results in the polarization. According to the position of the working potential to the corrosion potential, these methods can be divided in two categories:

- Measurements in the vicinity of the corrosion potential which are used for the determination of the polarization resistance and Tafel slopes.
- Measurements far away from the corrosion potential (>100 mV) which are used for example for determination of pitting potential, passivation and repassivation potentials.

Polarization scans refer to a polarization technique in which the potential of the working electrode is varied over a potential range at a selected rate and the current is monitored as a function of potential. In anodic polarization, the potential is swept in anodic (or more positive direction) which causes the working electrode to behave as anode whereas in cathodic polarization, the working electrode becomes more negative. In cyclic polarization which is a very common test for localized corrosion resistance, both anodic and cathodic polarizations are performed in a cyclic manner. In this case, the potential is swept in a single cycle from oxidation potential (or slightly below it) to the cathodic one.

Another widely used method for the investigation of corrosion phenomena is electrochemical impedance spectroscopy. An important advantage of EIS over other electrochemical techniques is the possibility of using very small amplitude signals without significantly disturbing the properties being measured (non-destructive method). EIS data is commonly analyzed by fitting it to an equivalent electrical circuit model which are common electrical elements such as resistor, capacitor and inductor. To be useful, the elements in the model should have a basis in the physical electrochemistry of the system e.g. the solution resistance can be shown by a resistor or the behavior of electrical double layer can be shown by a parallel resistor and capacitor.

In the impedance spectroscopy method, the response of the system to a sinusoidal signal is investigated.

$$E = E_0 \sin(\omega t)$$

where E_0 is the signal amplitude and $\omega = 2\pi f$ is the angular frequency and f is the alternating voltage frequency. By applying of this signal to a series of resistance-capacitance R-C circuit and taking into account the Laplace transform for a sine wave as:

$$L[\sin(\omega t)] = \frac{\omega}{s^2 + \omega^2}$$

The responding current can be written as:

$$i_{(s)} = \frac{E_0\omega}{s^2 + \omega^2} \frac{1}{R + \frac{1}{sC}} = \frac{E_0\omega}{R} \frac{1}{s^2 + \omega^2} \frac{1}{R + \frac{1}{sC}}$$

The steady-state equation may be rearranged into a simpler form:

$$i(t) = \frac{E_0}{R\left(1 + \frac{1}{(\omega RC)^2}\right)} \left[\sin(\omega t) + \frac{1}{\omega RC}\cos(\omega t)\right]$$

And by introducing $\varphi = \frac{1}{\omega RC}$, it can be expressed as:

$$i(t) = \frac{E_0}{\sqrt{R^2 + \frac{1}{(\omega C)^2}}} \sin(\omega t + \varphi) = \frac{E_0}{|Z|} \sin(\omega t + \varphi)$$

where φ is the phase angle between current and potential. It is obvious that the current has the same frequency as the applied potential but is phase shifted by the angle φ. The value $\left|Z\right|$ has units of resistance; it is the length of a vector obtained by the addition of two perpendicular vectors: R and $\frac{1}{\omega C}$. Impedance can be shown by complex notation as:

$$Z(j\omega) = Z' + jZ'' = R + \frac{1}{j\omega C} = R - j\frac{1}{\omega C}$$

where Z' and Z'' are the real and imaginary parts of impedance, respectively. In general, the complex impedance may be written for any circuit by taking R for a resistance, $1/j\omega C$ for a capacitance, and $j\omega L$ for an inductance. The variation of the impedance with frequency which allows the measurement of electrochemical reactions with different rates is often of interest and can be displayed in different ways. If the real part of impedance is plotted versus the imaginary part at different ω, the plot is called Nyquist plot. Figure 2.8 shows a Nyquist plot for parallel RC circuit with low frequency data on the right side of the plot and high frequency data on the left side. [53] The shape of the Nyquist plot is representative of the electrochemical processes at the surface of the electrodes and in the bulk of the electrolyte. On the Nyquist plot the impedance can be represented as a vector of length |Z|. The angle between this vector and the x-axis is frequency. The real part of impedance at high frequency can be used for calculation of electrolyte resistance whereas the real part at low frequency shows both electrolyte and substrate resistance.

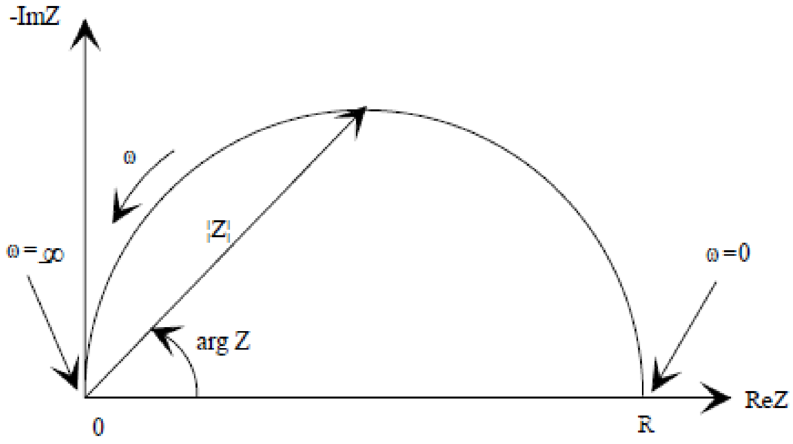

Figure 2.8: Nyquist plot for a parallel RC circuit

Actual real circuit elements show only approximate ideality over a limited frequency range. Thus an actual resistor always exhibits some capacitance and inductance as well and, in fact, acts somewhat like a transmission line. On the other hand, all real elements are actually distributed because they extend over a finite region of space rather than being localized at a point. The first distributed element introduced into electrochemistry was the infinite length Warburg impedance, Z_W, which is obtained from the solution of Fick's second law. [54] The Warburg impedance is a complex quantity with real and imaginary parts of equal magnitude. This impedance is given by the equation:

$$Z_W = \frac{W}{\sqrt{j\omega}}$$

where W is the Warburg parameter:

$$W = \frac{RT}{n^2F^2}\frac{1}{C_0\sqrt{D}}$$

where D is the diffusion coefficient, C_0 is the concentration of diffusive element and n is the number of electrons passes from the circuit.

The general method represented for ideally polarizable electrodes and in the presence of a Faradayic reaction is found experimentally on electrolytes. However, for solid electrodes due to the frequency dispersion, the impedance cannot be represented by the connection of simple R-C-L elements. The impedances may often be represented by an equation without simple electrical representation, through distributed elements.

In such cases the double-layer capacitance may be expressed in terms of a constant phase element (CPE). Its impedance is given by:

$$\overline{Z}_{CPE} = \frac{1}{T(j\omega)^{\varphi}}$$

where T is a constant in $Fcm^{-2}\ s^{\varphi-1}$ and φ is related to the angle of rotation of a purely capacitive line on the complex plane plots: $\alpha = 90° (1 - \varphi)$ as shown in Figure 2.9. [55]

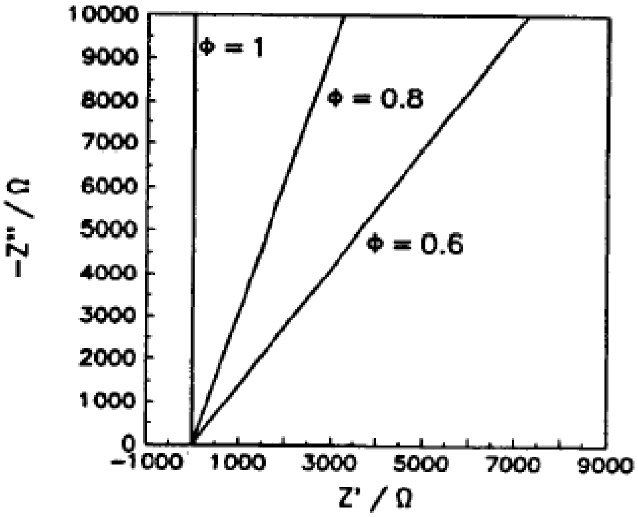

Figure 2.9: Complex plane plot in the presence of constant phase element

In general, the last equation may represent pure capacitance for $\varphi = 1$, infinite Warburg impedance for $\varphi = 0.5$, pure resistance for $\varphi = 0$, and pure inductance for $\varphi = -1$.

One of the most successful applications of EIS has been the evaluation of the properties of polymer coated metals and their changes during the exposure to corrosive environments. The final purpose of EIS characterization of protecting organic coatings is to obtain information about the system properties such as presence of defects, reactivity of interface, adhesion, barrier properties to water etc. which emerges that equivalent electrical circuit will have to be chosen carefully because it is possible to select several circuits which provide same results. One of the more extensive studies of the EIS characterization of organic coatings was published by Mansfeld et al. [56] He suggested a general model of an equivalent electrical circuit from which a large number of other models can be derived (Figure 2.10). This circuit is composed of the electrolyte resistance, followed by a capacitance (coating capacitance C_c) in parallel with a resistance (the coating or pore resistance R_p and finally an element Z_f which represents the electrochemical process at the metal interface.

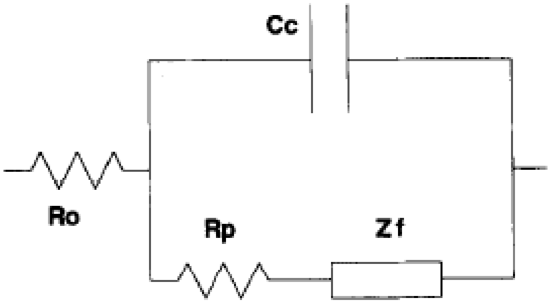

Figure 2.10: General equivalent electrical circuit for coated metals

It is the definition of Z_f which mainly distinguishes the circuits proposed in the literature. The works of Mansfeld et al. proposed two different circuits modeling the corrosion reaction:

1) A capacitance (the double layer capacitance C_{dl}) in parallel with a resistance (the charge transfer resistance R_{ct}) which describes the electrochemical reaction under activation control.

2) The second circuit considers a Warburg (W) element. In this case the diffusion process is suggested as being the controlling step and, with regard to impedance, the electrical behavior of the interface is dominated by the Warburg element.

3. Sol-Gel Method

3.1 Definition:

The sol-gel process is a chemical synthesis method which was initially used for the preparation of inorganic materials such as glasses and ceramics. A sol is a dispersion of colloidal particles suspended in a fluid matrix within Brownian motion. Colloids are suspension of particles of linear dimensions between 1-1000 nm which interact by short-range forces such as van der Waals attraction. A gel is an interconnected, rigid network with pores of submicrometer dimensions and polymeric chains whose average length is greater than a micrometer. In sol-gel process, the starting material or precursor, inorganic metal salts or metal alkoxides, undergoes simultaneous hydrolysis and condensation reactions. The resulting solution (alcogel) can then be converted to a solid material by subsequent aging, drying and heat treatment processes. Depending on the rate of the reactions and subsequent processing steps, materials with different compositions in the form of glasses, fibers, ceramic powders and thin films can be easily produced. Gel transformation to produce the final product can be done either by thermal evaporation of liquid (xerogels) or by replacing the liquid with a gas phase under supercritical condition (aerogels). The main difference between these two types of gels is the density of the resulting materials which is much less for aerogels.

Several advantages have made this process attractive in various fields. The relatively low temperature of this process minimizes the possibility of degradation of materials and the products. By appropriate chemical modification of the precursor, it is possible to control the rate of hydrolysis and condensation reaction, the particle size and the porosity. It also allows scientists to introduce organic groups into the inorganic materials [57-58] to enhance the mechanical and physical properties of the substrates. [59]

3.2 Hydrolysis and Condensation Reactions:

In the absence of acid or base catalyst, the hydrolysis reaction proceeds by nucleophilic addition of water molecules to the metal alkoxide precursor followed by proton transformation from water to the alkoxy group which then leaves as alcohol:

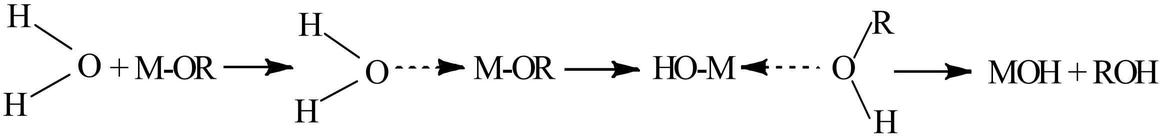

The resulting MOH species can then react with a further alkoxide (alcoxolation) or another MOH species (oxolation) or a solvated metal species (olation):

Alcoxolation:

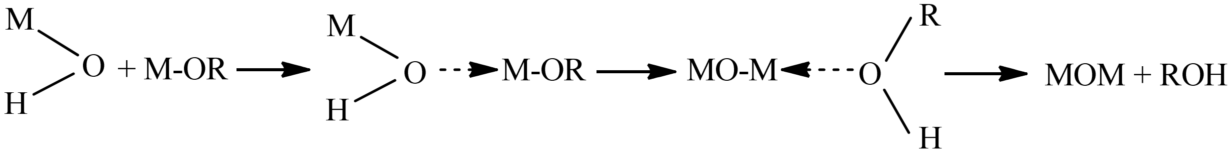

Oxolation:

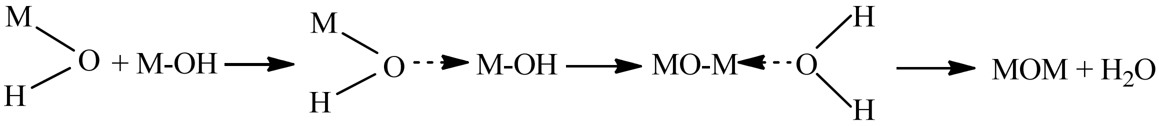

Olation:

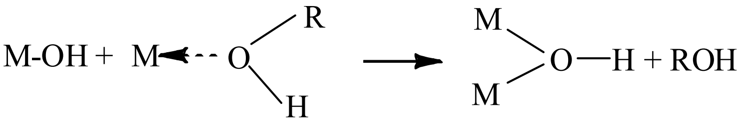

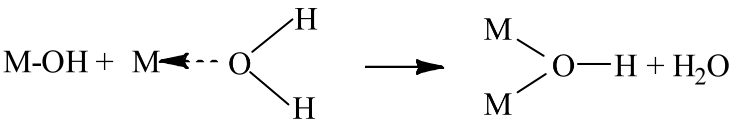

Partial negative charge of the nucleophile in hydrolysis and the partial positive charge of electrophilic metal and leaving group determine the thermodynamics of these reactions. Table 3.1 shows the estimated partial charge, $\delta(M)_r$, of some central atoms in a series of metal alkoxides in comparison to silicon alkoxide:

Ethoxide	$Zr(OEt)_4$	$Ti(OEt)_4$	$Nb(OEt)_5$	$Ta(OEt)_5$	$W(OEt)_6$	$Si(OEt)_4$
$\delta(M)$	+ 0.65	+ 0.63	+ 0.53	+ 0.49	+ 0.43	+ 0.32

Table 3.1: Partial charge of metal atom in a series of metal alkoxides

As the electropositive character of the metal increases, the hydrated metal ions have an increasing tendency toward acid dissociation:

$$[M...OH_2]^{z+} \rightleftharpoons [M\text{—}OH]^{(z-1)+} + H^+ \rightleftharpoons [M{=}O]^{(z-2)+} + 2\,H^+$$

Therefore, depending on the pH of the solution, three different species can be produced in hydrolysis reaction as depicted in Figure 3.1: [60]

$M-(OH_2)$	$M-OH$	$M{=}O$
Aquo	Hydroxo	Oxo

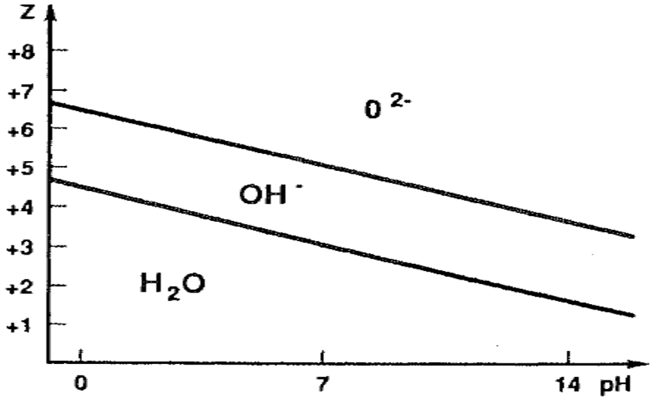

Figure 3.1: Charge versus pH diagram

For oxo-ligands with good nucleophilicity, the condensation reaction occurs when at least one of the reactant species is coordinatively unsaturated. Due to the poor nucleophilicity and absence of attacking group of aquo-ligands, no condensation reaction occurs. Hydroxo- ligands contain both good nucleophiles (O or OH) and good leaving groups (H_2O or OH), therefore condensation occurs as soon as one OH is present in the coordination sphere of M. Thus, it is generally necessary to be in hydroxo domain to generate condensed species.

The R group of the alkoxide precursor plays an important role in the rate of hydrolysis. Chain elongation and in particular chain branching in the alkoxide ligands lead to a dramatic decrease of the reaction rate. [61] The use of co-solvents such as n-propanol results in the substitution of alkoxide ligands with n-propoxide group during the first step of hydrolysis which subsequently leads to the reduction of the rate of second reaction step due to the lower reactivity of n-propoxide group. Therefore the control of reaction rate is achievable.

3.2.1 The Role of Catalysts:

The effect of acid and base catalysts on the rate of both hydrolysis and condensation reactions can be predicted by calculation of the charge of the species at various steps of these reactions. In acid catalysis, the least positively charged species will react faster so chain end sites will be more reactive than center sites. Conversely, for base catalyzed reactions the most positively charged species will react faster which results in higher activity of chain center sites.

An acid catalyst reaction proceeds by an S_N2-type mechanism. The leaving alkoxy group is rapidly protonated and a water molecule performs a nucleophilic attack at the central metal atom. In the case of silicon alkoxides and under acid catalysis, the first step of hydrolysis reaction proceeds rapidly and results in the formation of $(RO)_3Si\text{-}OH$. After removing of one alkoxy group, protonation of the second silanol species will be less favorable and hence the second hydrolysis step will be slower. This results in the competitive condensation reaction between Si-OH and protonated Si-OR groups which plays an important role in the final structure of the solution. Due to the higher reactivity of Si-OR groups, acid catalysis will initially lead to chain elongation and formation of linear polymers. The cross-linking of these chains finally leads to the formation of a homogenous and dense gel with small pore size. [62]

a) Acid catalyzed hydrolysis:

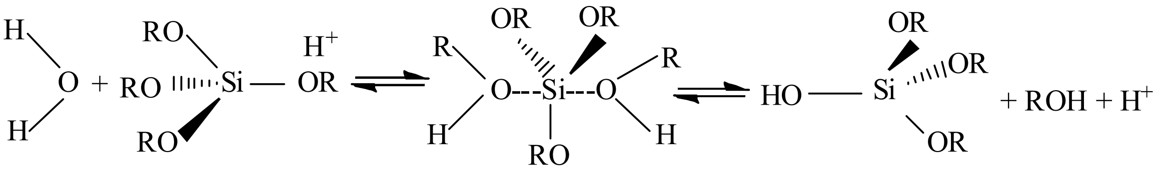

b) Acid catalyzed condensation:

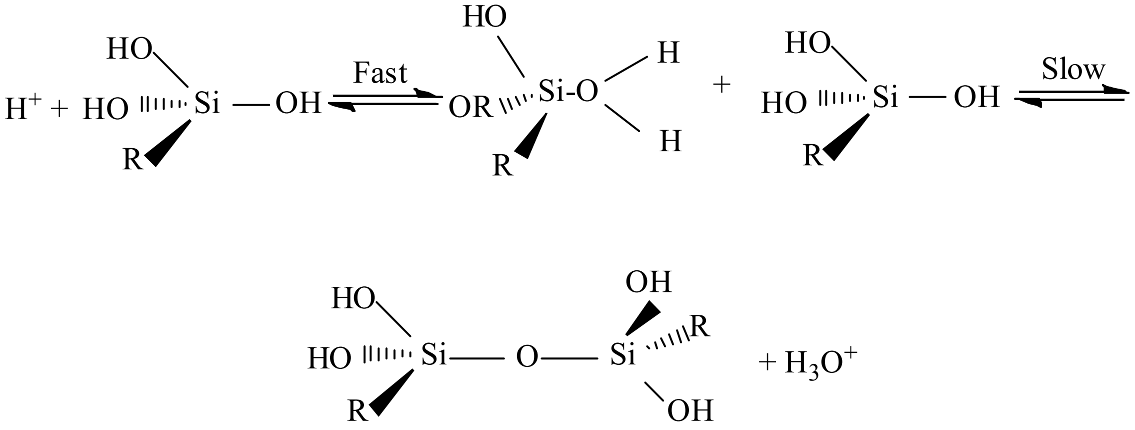

Base catalyst proceeds faster when electron donating –OR groups are removed. It increases the rate of condensation reaction by producing better nucleophiles than water and silanol. This process occurs as a two-step process with the formation of a pentacoordinate intermediate.

a) Base catalyzed hydrolysis:

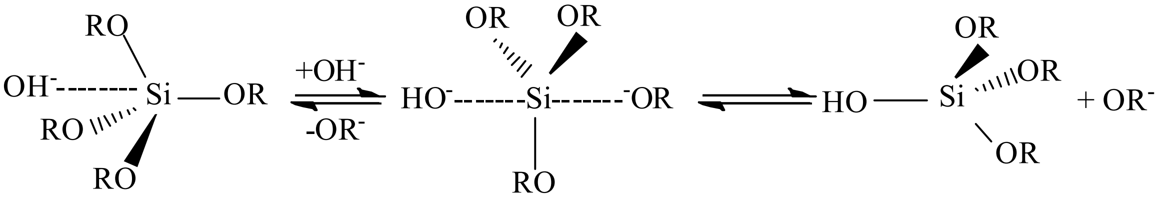

b) Base catalyzed condensation:

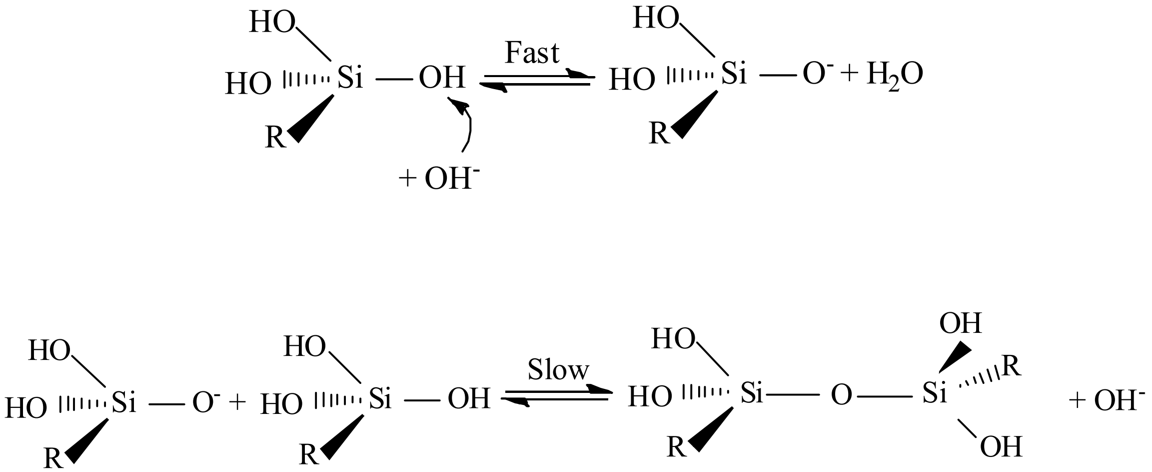

3.2.2 The Role of Water:

The water/alkoxide ratio, known as h, influences the rate of reactions. For a complete hydrolysis, water/alkoxide ratio must be 4:

$$M(OR)_4 + 4\ H_2O \rightleftharpoons M(OH)_4 + 4\ ROH$$

In the presence of small amounts of water and due to the reduced reactant concentration, the hydrolysis rate will decrease. On the other hand, a large amount of water results in a dilution of precursor and an increasing gel time.

It has been shown that the reaction of silicon alkoxide with a low concentration of water (H_2O / Si < 2) leads to the formation of esterified polymeric species. Increasing the water ratio to 4-10 leads to the hydrolysis completion and the formation of polymeric chains in acidic condition. [63] A further addition of water (20-25) leads to the separation of polymeric strands which subsequently hinders the intermolecular condensation reactions. [64] Addition of other solvents such as alcohols and dioxane increases the solvation of H^+

and OH^- by breaking the hydrogen bonds in water molecules. This results in the decrease of acidity or basicity of the solution and consequently the rate of hydrolysis. [65]

As shown in Table 3.2, by controlling the rate of hydrolysis and condensation reactions, different sol-gel products can be obtained: [66]

Hydrolysis rate	Condensation rate	Product
Slow	Slow	Colloids / Sols
Fast	Slow	Polymeric Gels
Fast	Fast	Colloidal Gels or Gelatinous Precipitate
Slow	Fast	Controlled Precipitation

Table 3.2: Products obtained according to the relative rates of hydrolysis and condensation

Due to the high chemical reactivity of the metal alkoxides in the presence of water, they tend to precipitate. In order to prevent phase separation during the process, chemical additives such as glycols, β-diketones and carboxylic acids have been used which form mixed complexes with alkoxide ligands. These mixed ligands are more inert towards displacement and thus provide control of the main condensation pathway.

3.3 Gelation:

Gelation, with characteristic gelation time t_{gel}, can be defined as a process in which a giant cluster is produced as a result of connection between clusters during the condensation reaction. Several attempts have been made to measure the gelation time. For example, it is defined as a point where the gel corresponds to a certain viscosity. The most precise method was developed by Sacks and Sheu which is based on the viscoelastic behavior of the gel as a function of shear rate. [67] As shown in Figure 3.2, the rapid change in the loss tangent near to t_{gel} shows that the sufficient interconnections between particles to support a load of elasticity have been achieved. [66]

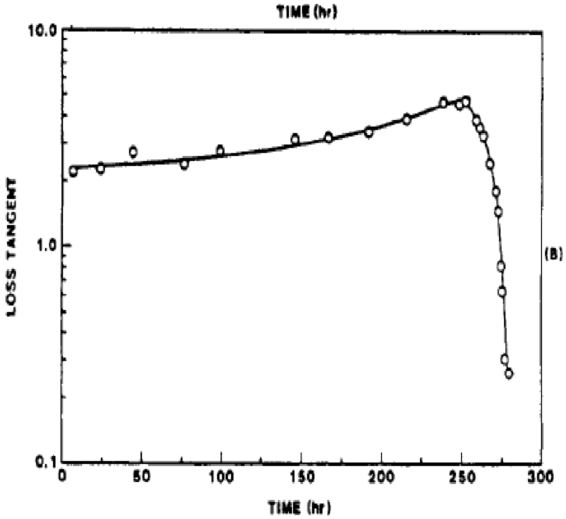

Figure 3.2: Loss tangent as a measure of gelation time

The gelation phenomenon has been explained by several theories. According to the classical or mean field theory which was developed by Flory, [68] the critical condition for the formation of a gel is:

$$P_c = \frac{1}{(z-1)}$$

where z is the functionality number of the polymer. For example, in the case of silica gel for functionality of 4, $P_c = 1/3$ which means that still two-third of the connections are still available for further reactions and play a role in subsequent processing. This theory however is incapable of explaining the ring formation during the gelation.

According to the percolation theory, [69] initial empty sites are randomly filled with monomers and bonding occurs when two circles or particles are adjacent resulting in loops of various sizes during expansion (Figure 3.3).

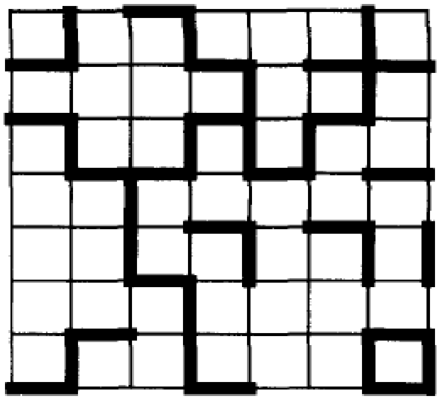

Figure 3.3: A schematic presentation of percolation theory

This model is especially applicable to describe the gel formation by linking the sol particles.

3.4 Aging:

Aging is a procedure in which the liquid in pores is excluded from the gel structure. This step can proceed by four different processes including polymerization, synerisis, coarsening and phase transformation.

During the polymerization process, formation of new bridges between sol particles results in an increase in the structure strength. In the case of silica gel, due to the large concentration of free hydroxyl group, the gelation continues long after the gel point. [70]

Synerisis is the spontaneous shrinkage of the gel network which results in the expulsion of remaining liquid from pores. [71] Driving force for this process is the tendency of the system to reduce the solid-liquid interfacial area of the gel. [72] It has been shown that the rate of this step is dependent on the pH of the electrolyte and has a minimum at the isoelectric point (IEP). [73] Coarsening or ripening is an irreversible decrease in surface area through dissolution or reprecipitation processes. Phase transformation can occur by synerisis or segregation of the liquid into two or more phases.

3.5 Drying:

This process [74-75] can be divided into three stages: during the first stage the liquid evaporation rate, which is driven by capillary forces, is independent of the time and is called constant rate period (CRP). [76] When further shrinkage of the sol is impossible, the second stage begins. During this stage which is governed by gradient in capillary stress, [77] the rate of evaporation, first falling rate period (FRP1), decreases. The time-dependent nature of this gradient favors the flow of liquid towards the outer surface. When the pores are substantially emptied and surface tension becomes too high, stage three begins. At this stage, liquid flow to the outer surface becomes so slow that the liquid is isolated in the pockets, hence the evaporation of liquid proceeds by diffusion of the vapor. At this stage, drying enters the second falling rate period (FRP2). In this period, no further dimensional changes happen and there is just a slow loss of weight until the equilibrium is reached. Dwivedi [78] investigated these three stages on alumina gels (Figure 3.4) and found that 87 % of the initial liquid in the gel are removed in stage 1, 10 % in stage 2 and only 3 % in stage 3.

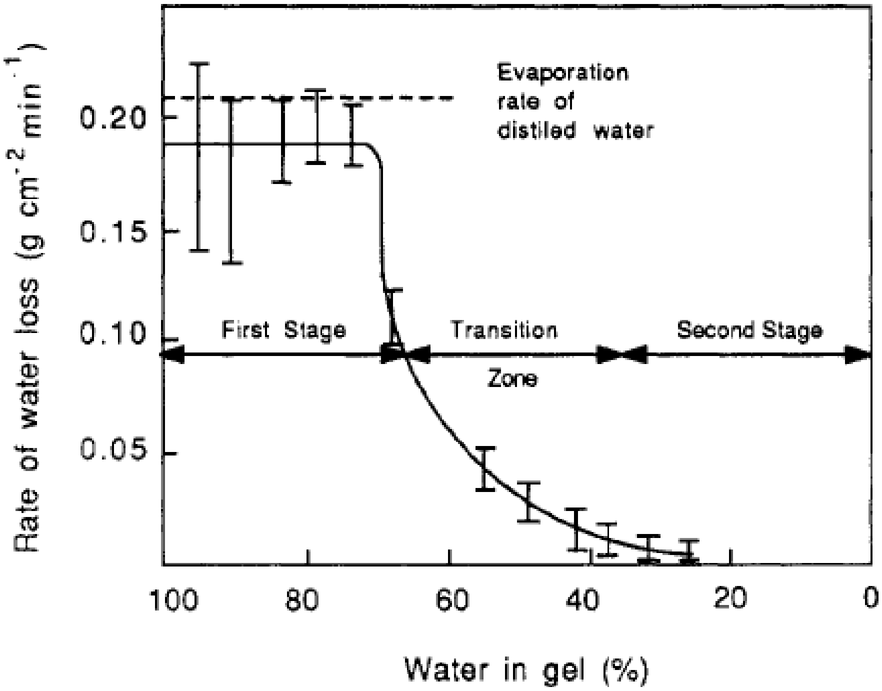

Figure 3.4: Rate of water loss against water in alumina gel at different stages of drying

He also found that cracking almost always occurs at the some point in stage 2 and is strongly dependent on the thickness of the gel.

Cracks appear due to the differential contraction between the exterior and the interior of the gel during the drying step which arises from tensile stress in the sol. This phenomenon is shown schematically in Figure 3.5. [79]

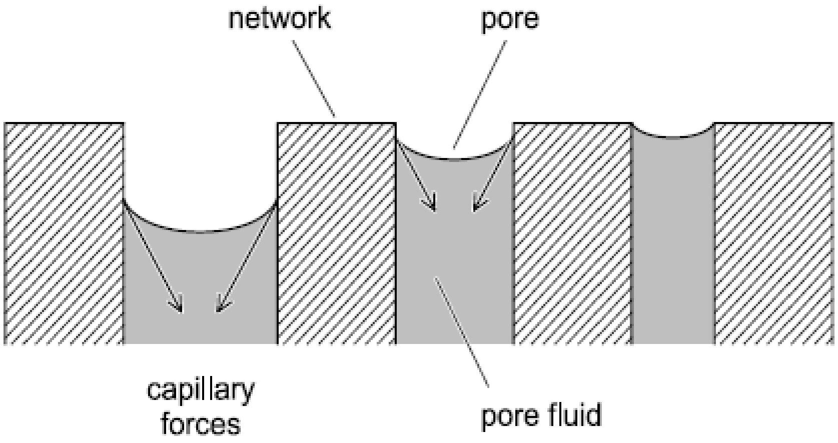

Figure 3.5: Representation of the contracting surface forces in pores of different size during drying

For thin film applications, the coating changes from viscous liquid to elastic solid. The evaporation of the solvent, compositional and structural changes and temperature change bring the coating out of its stress-free region which results in the formation of cracks. Formation of cracks depends on several parameters such as the magnitude of stress, the thickness of the coating, material properties and the presence of voids. Several strategies can be used to avoid crack formation. For example, cracks from low temperature drying can be avoided by choosing a coating solution deposition/drying procedure which favor solidification of the solution with minimum trapped solvent. Controlling the pore size, aging of the gel before drying and addition of chemicals such as surfactants and supercritical drying are other strategies to avoid fracture formation during drying.

3.6 Densification:

Densification is the last treatment of a gel in order to remove the organic residues from the sol-gel product or to evaporate the remaining water from the sol solution to provide a denser and stiffer connected network. The amount of water in the gel is the most important parameter in the heat treatment process because it affects the viscosity which in turn determines the temperature of the beginning of the densification. [80] According to Frenkel's theory [81] at early stages of heat treatment, dissipation of energy during viscous flow is provided by the reduction of surface area. Scherer's model [82] describes the early and intermediate stages of heat treatment which assumes that the microstructure consists of cylindrical intersections in a cubic array. In order to reduce the surface area, they become shorter and thicker. The last stage of heat treatment can be interpreted by the Mackenzie-Shuttleworth model [83] which is based on the Frenkel's theory and can only be applied to systems with closed porosity.

3.7 Application of Sol-Gel Process:

With the right selection of reactants and controlling the parameters, different types of products such as monoliths, fibers, membranes and films can be obtained from the sol-gel process.

Monoliths are defined as bulk gels (smallest dimension $\geq$ 1 mm) cast to shape and processed without cracking. The purity of the products depends strongly on the quality of the precursor gel. The first monolith was produced from alumina gel by Yoldas. [84] Hydrolysis of aluminum alkoxides in a large excess of water (R = 100-200) at 353-373 K, results in the precipitation of boehmite (ALOOH) which converts to a clear solution by peptizing of mineral acids (HNO_3). Gelation is generally achieved by concentration of the gel by boiling or evaporation. Yoldas observed that with an Acid:Al molar ratio of 0.07, the minimum gel volume occurred. The main application of monoliths are optical components such as graded refractive index (GRIN) glasses or transparent aerogels used as Cherenkov detectors or insulators.

Fibers can be produced either directly from the heat treatment of viscous sols at room temperature or by drawing monoliths above their glass softening temperature. Potential applications include reinforcing phases in composites, refractory textiles and high temperature superconductors.

The porosity of sol-gel products recommends them for separation applications. Compared to conventional organic polymer membranes, sol-gel membranes offer several advantages such as operation at higher temperature, resistance against swelling or shrinkage in contact with liquid and more abrasion-resistance. Porous gels, in form of either aerogels or xerogels, have been applied in chromatography, thermal or acoustical insulation and catalysis.

Preparation of thin films is one of the most important aspects of the sol-gel process. It is possible to control the microstructure of the deposited film, i.e., the pore size, pore volume and surface area. Thin films can be obtained through deposition of the sol prior to the gel point by common methods such as dipping, spinning and spraying.

3.7.1 Dip Coating:

Dip coating refers to the immersion of a substrate into a tank containing the coating material with consequent withdrawing the substrate from the tank. This process which is applicable for complex shapes can be divided into five stages as described by Scriven: [85] immersion, start-up, deposition, drainage and evaporation as shown in Figure 3.6.

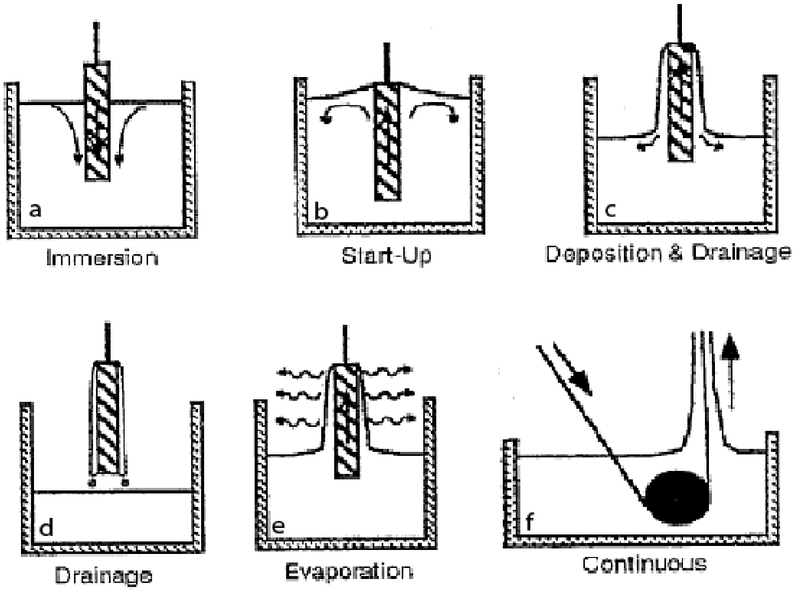

Figure 3.6: Stages of dip coating process, a-e) batch, f) continuous

In this process, the moving substrate is carrying some of the liquid towards the deposition region. The inner layer moves upward with the substrate while the outer layer returns to the bath. The film thickness is controlled by a competition of six forces:

1. Viscous drag upward on the liquid by the moving substrate
2. Gravity force
3. Resultant force of surface tension in the concavely curved meniscus
4. Inertial force of the boundary layer liquid arriving at the deposition region
5. Surface tension gradient
6. Disjoining or conjoining pressure, important for films less than 1 μm thick

The thickness of dip-coated film can be calculated by: [86]

$$h = 0.944\left(\frac{\eta U}{\gamma_{LV}}\right)^{1/6}\left(\frac{\eta U}{\rho g}\right)^{1/2}$$

where η is the liquid viscosity, U is the substrate speed, γ_{LV} is liquid-vapor surface tension and ρg is the gravity force. The thickness of the deposited film is approximately proportional to the $U^{2/3}$. [87] It is possible to deposit thick film up to 1 μm on any substrate shapes by this method but this enhances the possibility of crack formation.

3.7.2 Spin Coating:

The process of applying a solution to a horizontal rotating disc, resulting in ejection and evaporation of the solvent and leaving a liquid or solid film, is called spin coating. Bornside et al. [88] divided the spin coating process into four stages: deposition, spin-up, spin-off and evaporation as shown in Figure 3.7. Initially, an excess of the solution is deposited onto the surface. In the spin-up stage the liquid flows rapidly outwards, driven by centrifugal force generated by the rotating substrate. In the spin-off stage, excess liquid flows to perimeter and leaves as droplets. In the fourth stage, evaporation becomes the primary mechanism of thinning.

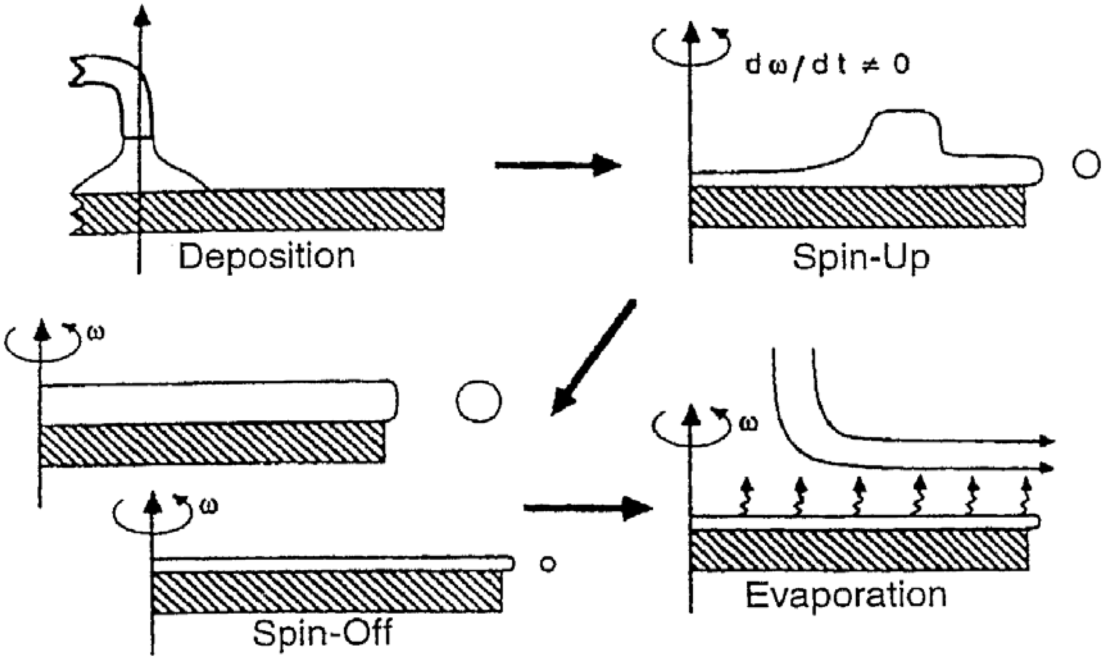

Figure 3.7: Stages of batch spinning process

The final film thickness is given by: [89]

$$h(t) = \frac{h}{\left(1 + 4\rho\omega^2 h_\circ^2 t / 3\eta\right)^{1/2}}$$

where h_0 is the initial thickness, t is time, ω is angular velocity and ρ is the density of the liquid. Theoretically, ω and ρ are assumed to be constant. A spun film reaches its final thickness by evaporation after the film has became so thin and viscous that its flow stops. Meyerhofer [90] found that the final thickness and the total elapsed time to achieve this thickness are:

$$h_{final} = \left(1 - \frac{\rho_A{}^\circ}{\rho_A}\right)\left(\frac{3\eta e}{2\rho^\circ{}_A\omega^2}\right)^{1/3}$$

and

$$t_{f\,inal} = t_{spin-off} + h_{spin-off}\left(\frac{\rho^\circ{}_A}{e\rho_A}\right)$$

where ρ_A is the mass of volatile solvent per unit volume, $\rho^\circ{}_A$ is the initial value and e is the evaporation rate which depends on the mass transfer coefficient. According to these equations, the final thickness of the film is related inversely to $\omega^{2/3}$ and $\eta^{1/3}$. This method can be only applied to flat samples and results in much thinner film than the dip coating method. Therefore, the probability of crack formation in this method is less problematic therefore, this method was used for thin film formation on magnesium sample in our investigation.

3.8 Precursors Properties:

3.8.1 Zirconia Sol:

Zirconia is a multifunctional material which has been successfully applied on different materials to enhance their corrosion resistance. [91-94] The hydrolysis reaction of zirconium alkoxides generally can be expressed as: [95]

$$Zr(OR)_4 + H_2O \longrightarrow ZrO(OR)_2 + 2\ ROH$$

$$2\ ZrO(OR)_2 \longrightarrow ZrO_2 + Zr(OR)_4$$

Due to the high chemical reactivity of zirconium alkoxides and in order to obtain stable sol solution, the additives must be added carefully to strongly restrain both hydrolysis and condensation reaction.

Bradley and Carter [96-97] investigated the hydrolysis reaction of zirconium alkoxides and concluded that the hydrolysis of these alkoxides leads to the formation of polymeric oxide-alkoxide $[ZrO_x(OR)_{4-2x}]_n$ materials. They also showed that the final structure of the product depends strongly to the amount of water-alkoxide ratio. For $h < 1.0$, the resulting product showed the trilinear structure which can extend its dimension during the condensation reaction (Figure 3.8).

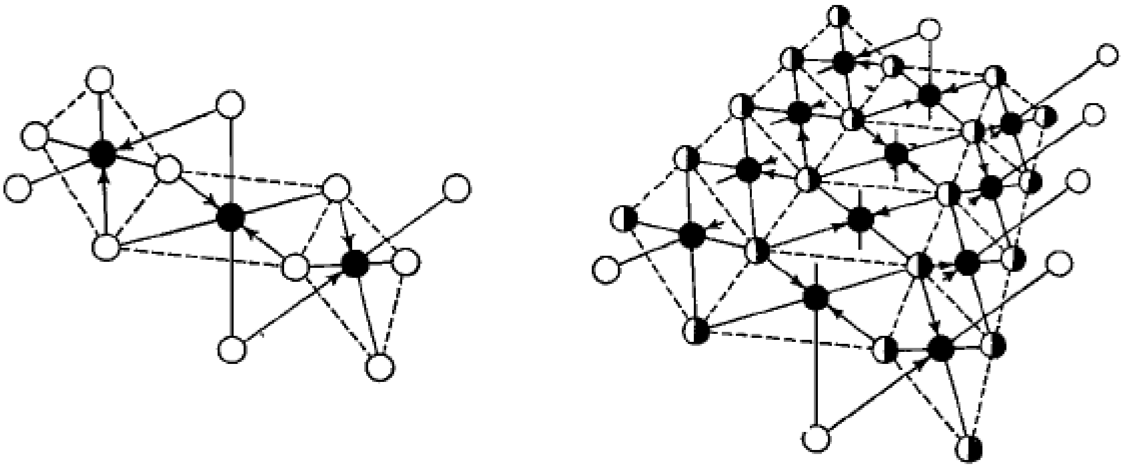

Figure 3.8: Zr$_3$(OR)$_{12}$ (left) and a section of infinite trilinear polymer (right)

For h >1.0, monomers are solvated as dimeric species which result in the formation of bilinear polymers (Figure 3.9).

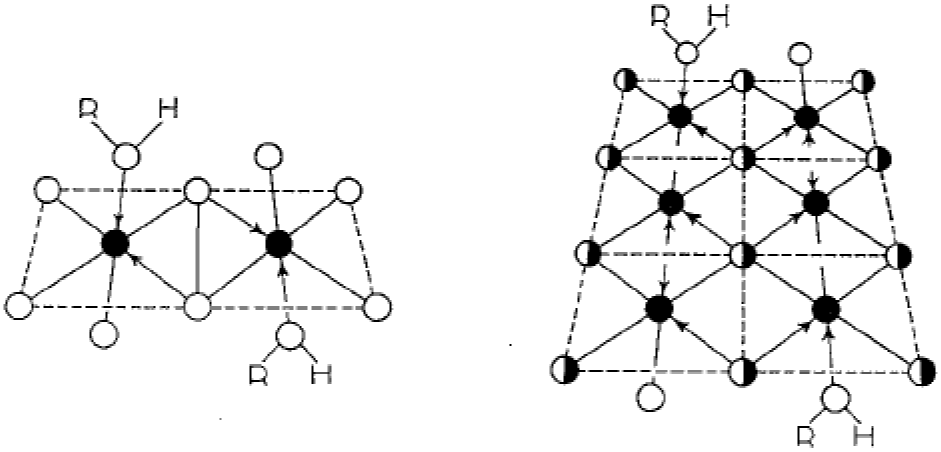

Figure 3.9: Solvated dimer of zirconium alkoxides (left) and a section of infinite bilinear polymer (right)

The amount of stabilizer also plays an important role in the structure of the zirconia sol-gel product. It is well known that in the presence of excess alcohol, zirconium propoxide shows dimeric structure (Figure 3.10a) which in addition of acetylacetone and water will be transformed to a ladder-shaped linear polymer with the general formula unit Zr(acac)O(OH) (Figure 3.10b). [98-99]

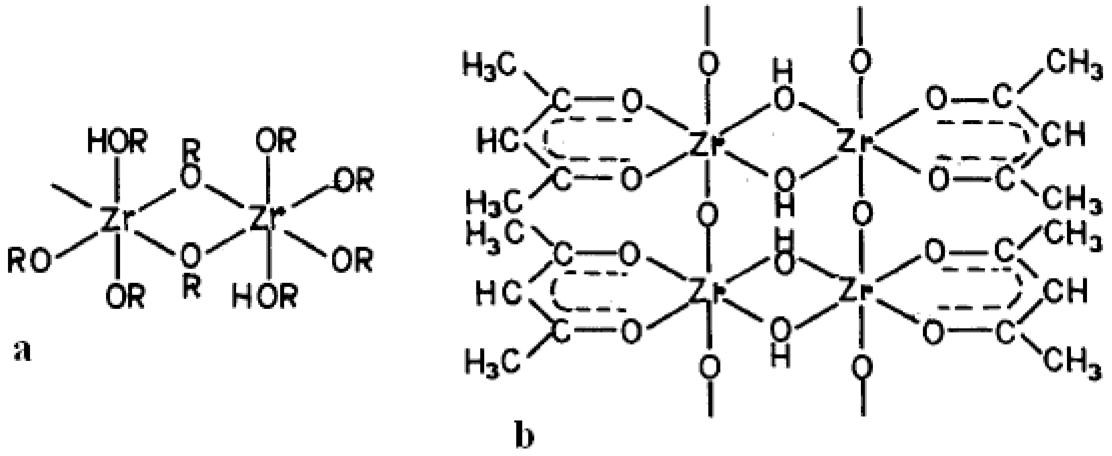

3.10: Different structures obtained during the hydrolysis and condensation reactions of zirconium propoxide in the presence of acetylacetone and water

By controlling the amount of these additives in the sol solution, it is possible to produce highly compact thin films which can provide appropriate protection on metals against corrosion.

3.8.2 Phenyl-triethoxysilane (PTES):

The chemistry of silicon alkoxides has been widely investigated. [100-101] It is well-known that all silicon-containing compounds are constructed from tetrahedral units with silicon as the central atom. These tetrahedral units share the corners; therefore the resulting structures have many degrees of freedom and can adopt a variety of geometries. Organically Modified Silicates (ORMOSILs) introduced by Schmidt [102] have been widely used for different purposes. Generally, the alkoxy groups of the alkoxysilanes are hydrolyzed to form silanol-containing species which leads to the formation of oligomers during the condensation reaction. These oligomers can then build hydrogen bonds to the OH- groups of the substrate which bond covalently to the substrate during drying or curing. [103] Condensation of silanol groups result in the extension of the siloxane structure.

The extent and mode of the condensation reaction in substituted organosilicon compounds is affected by the number of organic groups attached to the silicon. [104] For film deposition purpose, the organic group must be also able to reduce the porosity of the inorganic skeleton.

The hydrolysis reaction of PTES which has used for preparation of modified coatings proceeds through the following equations, where several species are present:

$$PhSi(OR)_3 \xrightarrow[-ROH]{H_2O} PhSi(OR)_2OH \xrightarrow[-ROH]{H_2O} PhSi(OR)(OH)_2 \xrightarrow[-ROH]{H_2O} PhSi(OH)_3$$

Two different mechanisms have been suggested for the hydrolysis of phenylsilane compounds: [105-106]

a) Acid catalysis:

$$PhSi(OR)_3 \underset{fast}{\overset{H^+}{\rightleftharpoons}} PhSi(OH^+R)OR_2 \underset{slow}{\overset{H_2O}{\rightleftharpoons}} PhSi(OH)(OR)_2 + ROH + H^+$$

b) Base catalysis:

$$PhSi(OR)_3 \overset{OH^-}{\rightleftharpoons} PhSi^-(OR)_3(OH) \xrightarrow{-RO^{\ominus}} PhSi(OR)_2(OH) \xrightarrow{-RO^{\ominus}} PhSi(OH)_3$$

It is suggested that the dominant mechanism depends strongly on the composition of the solution and its pH. From the experimental results, they suggested that for acidic pH specific, not general, acid catalysis can be established whereas for basic region of pH the general base catalysis mechanism (attack of water on silicon) can be applied.

3.8.3 3-Glycidyloxypropyltrimethoxysilane (GLYMO):

GLYMO is an organofunctional alkoxysilane monomer that can undergo both the sol-gel polymerization of the alkoxy groups and curing of the epoxy functionality to form a hybrid network with covalent bonds between organic and inorganic phases. [107] The hydrolysis reaction of GLYMO can be expressed as:

$$\text{R-Si(OMe)}_3 + 3/2\ \text{H}_2\text{O} \longrightarrow \text{R-Si(OMe)}_{3/2}\text{(OH)}_{3/2} + 3/2\ \text{MeOH}$$

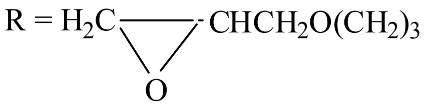

The epoxy group of GLYMO is capable of forming either diol units by hydrolytic ring opening or polyethylene oxide chains by polyaddition. [108] In the presence of H^+ and H_2O, the epoxide ring of GLYMO will open to form hydroxyl (-OH) groups by the hydrolysis reaction. [109-110] The organic chains can be connected with each other through C-O-C bonds by condensation reaction to form polyethylene oxide (PEO) chain. On the other hand, the silicate from GLYMO will form Si-O-Si backbones connected by PEO chains through the sol-gel process. Hence, the hybrid material has the advantage of both the organic and inorganic materials.

Some critical points must be taken into account when working with GLYMO. It has become clear that, there is a competitive process between organic and inorganic polymerization; a faster polycondensation rate of the inorganic network hinders the polymerization of the organic network and vice versa. [111] The presence of water and alcohols in the synthesis can also reduce the formation of polyethylene oxide units and lower the degree of control in the final microstructure. [112-113] The epoxides, in fact, can react with water in acidic condition or, for instance, with alcohol to form diols or methyl ether terminal groups. [114] Figure 3.11 summarizes different reaction pathways of this precursor to provide different products: [115]

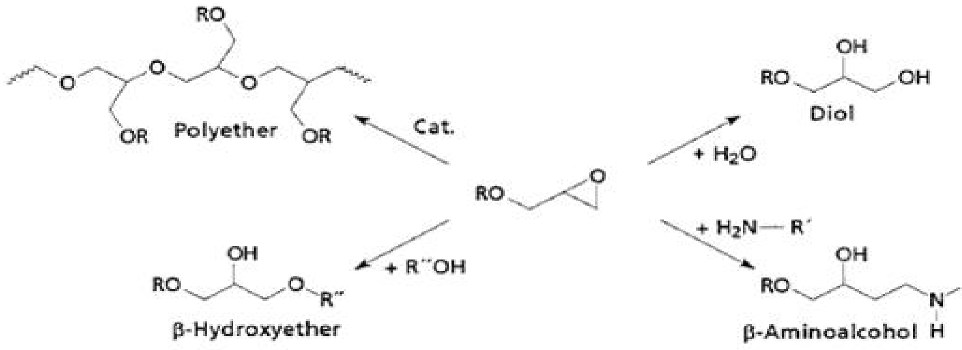

Figure 3.11: Possible reaction pathways of epoxy group

Therefore, the sol-gel reaction must be controlled carefully to result in the best connected network for protection purposes. Using high amount of acid catalysis can also result in the formation of glycol according to the following reaction, which should prevent the formation of PEO network on metal surfaces:

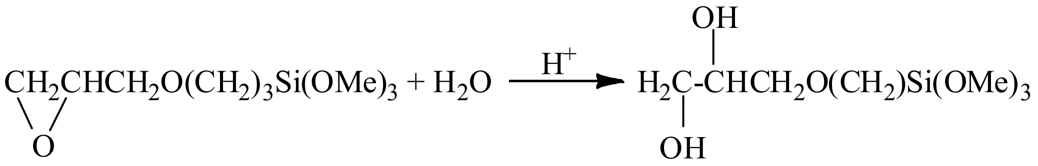

$$\underset{O}{\underset{\backslash\,/}{CH_2CH}}CH_2O(CH_2)_3Si(OMe)_3 + H_2O \xrightarrow{H^+} \underset{OH}{H_2C}\text{-}\overset{OH}{C}HCH_2O(CH_2)Si(OMe)_3$$

This reaction can result in the decrease of the resistance of coated surfaces against moisture which should be prevented. Therefore, an optimized amount of acid should be used in this reaction to prevent any unwanted reactions.

3.8.4 Vinyl-triethoxysilane (VTES):

The organoalkoxy silane containing olefinic moieties (allyl or vinyl) tend to build a polymeric network by thermally or photochemically induced organic polymerization of C=C bonds, simultaneously with the condensation of the silica network. Alkoxysilyl groups of vinyl-triethoxysilane monomers form Si-O-Si bonds upon condensation with other inorganic precursors. Accordingly, the vinyl groups polymerize with other vinyl groups which lead to the formation of inorganic/organic polymers or inorganic/organic copolymers. In other words, vinyltriethoxysilane (VTES) reacts on one end with the substrate and at the other end with the polymer matrix. The ethoxy group in VTES represents a hydrolysable unit and so the silane is hydrolyzed to the corresponding silanol in the presence of water which results in a polysiloxane layer bonded to the surface with an array of vinyl groups oriented outwards. These vinyl groups extend their dimensions during the condensation reaction and provide a film with closer structural properties.

3.8.5 Silica-Zirconia Sol:

Mixed oxide layers have been used to improve the adhesion of the deposited layer onto the substrate. The major problem in this area arises from the different reaction rates of the reactants (metal alkoxides) which make it difficult to produce a suitable solution which can enhance the corrosion resistance of the material. Several strategies can be used to overcome this problem such as pre-hydrolyzing the less reactive precursor to match the reactivity of its counterpart and using a chemical modifier to change hydrolysis/condensation rate of the more reactive precursor. [116] It is shown that the incorporation of zirconium oxide into a silicon oxide matrix to produce hetero-linkages of Zr-O-Si can improve the chemical resistance of the substrate against alkaline attack [117-118], its fracture toughness [119] and surface acidity. [120] Nogami et al. [121] proposed the following linear chain for Zr/TEOS = 0.5 and under acidic catalysis:

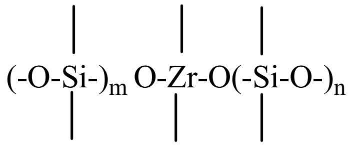

$$(\text{-O-Si-})_m\,\text{O-Zr-O}(\text{-Si-O-})_n$$

They reported that the increasing of the ratio Zr/(Si + Zr) results in the further hydrolysis to develop branches from Zr atoms and form aggregates of three dimensional polymers. Zhan et al. proposed following mechanism for the reaction of Zr-acetylacetone with silicon alkoxide (Figure 3.12): [122]

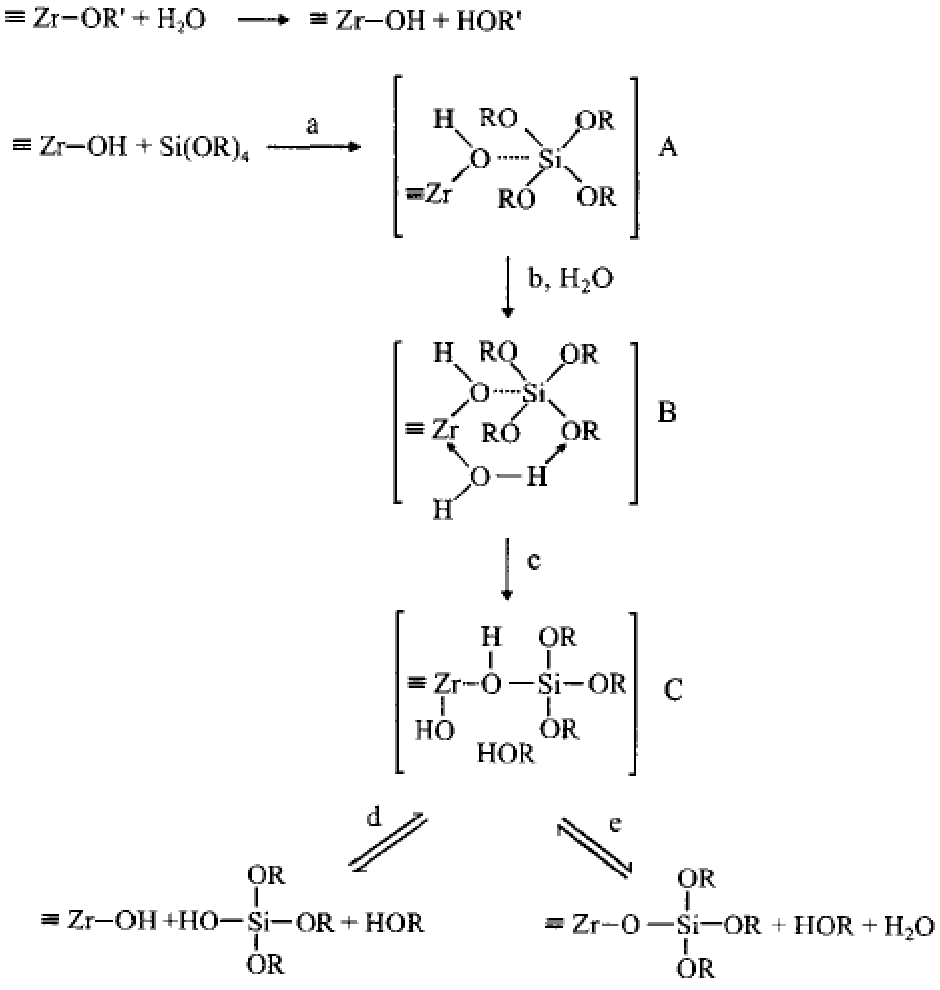

Figure 3.12: Proposed mechanism for Zr-acac-Si in presence of water

They supposed that in addition of water, zirconium undergoes hydrolysis reaction. Resulting species then interact with TEOS through the hydroxyl group of the intermediate which lead to the formation of complex A. Due to the ability of zirconium to increase its coordination number (up to 8), a water molecule can then react with complex A and convert it to intermediate B which decompose to provide intermediate C. This can then convert to two different products via the paths d or e.

4. Experimental

4.1 Sample Preparation:

Magnesium samples were cut from rods (98%, Goodfellow Company) into cylindrical pieces with a thickness of 3 mm and a diameter of 23 mm. To obtain smooth and reproducible surfaces, it is necessary to polish the samples before deposition procedure. As described earlier, the presence of any contamination affects the adhesion of the deposited film and hence deteriorates its ability to provide good corrosion resistance. In our investigation, the samples were grinded by Carbimet P2500 paper. Another problem is the natural oxide layer on magnesium which also affects the adhesion. In order to avoid any contamination, each sample was washed with distilled water and ethanol and dried by pressurized air before deposition.

4.2 Sol Solutions:

Due to the high competition between hydrolysis and condensation reactions in sol-gel process a keen attention must be paid on the amount of each component to obtain a sol-gel solution with best interconnected network. In our experiments, acetic acid and acetylacetone were used as a catalyst and stabilizer, respectively. A mixture of water and propanol was added to the solution to control the rate of hydrolysis reaction. The quantities of catalyst were varied. In the following, one sol composition for each precursor is given as example.

4.2.1 Zirconia Sol:

2.5 ml zirconium (IV) propoxide 70 wt% in 1-propanol (98%, Fluka) was added to a mixture of 1.25 ml glacial acetic acid (99%, Fluka) and 1.25 ml acetylacetone (98% GC-Assay, Sigma-Aldrich) and stirred for 15 minutes. A mixture of distilled water and 1-propanol in the volume ratio of 1:4 was added and the solution was stirred for 1 hour. The resulting sol is a transparent, light yellow and homogeneous solution. Due to the high reactivity of zirconium alkoxide with humidity, its addition has to be handled under argon atmosphere to prevent any precipitation.

4.2.2 Phenyl-triethoxysilane (PTES):

2.1 ml Phenyl-triethoxysilane (98%, Aldrich) was added to 2 ml acetylacetone and stirred for 15 minutes. Then a mixture of propanol and water at a volume ratio of 4:1 was added to the solution and stirred for 1 hour at room temperature to allow the reaction to proceed. Resulting colourless solution was then deposited on magnesium samples.

4.2.3 3-Glycidoxypropyltrimethoxy-silane (GLYMO):

GLYMO (> 97%, Fluka) was added to a solution of 0.5 ml acetic acid (99%, Fluka) and 2 ml acetylacetone (99%, Aldrich). The solution was stirred for 15 minutes at ambient temperature and a mixture of distilled water and propanol in the volume ratio of 1:4 (99%, Fluka) was added and final solution stirred for 1 hour.

4.2.4 Vinyl-triethoxysilane (VTES):

2 ml of VTES were added to a mixture of 1.5 ml acetic acid (99%, Fluka) and 2.5 ml of acetylacetone (99%, Aldrich). The solution was stirred for 15 minutes at ambient temperature. A mixture of water and propanol with a volume ratio of 1:4 was added to the solution and stirred for 1 hour to complete hydrolysis and condensation reactions. The resulting solution was then deposited on magnesium for further investigation.

4.2.5 Mixed Silicon-Zirconium Solutions:

In order to overcome the adhesion problem of zirconium oxide on magnesium, a mixed solution of zirconia-silicon was prepared. For this purpose, a mixture containing of two different sol-gel solutions was prepared. The first sol was the silane sol which was prepared by hydrolysis of silane base precursor (PTES, VTES and GLYMO) in 1-propanol adding diluted aqueous solution of HNO_3 (pH = 0.5) in 1:1:0.2 volume ratios under stirring at room temperature for 1 hour. The second sol containing zirconium was obtained by controlled hydrolysis of zirconium (IV) propoxide with the complexing agent acetylacetone in a 1:1 volume ratio under ultrasonic agitation. Both sols were then mixed and this hybrid solution was stirred for one more hour. The resulting sol was homogeneous, transparent and had a light-yellow color.

4.2.6 Deposition and Heat Treatment:

The resulting sols were deposited onto magnesium substrates with a syringe through a 0.45 μm nylon filter to avoid any contamination or particles on the deposited films. All coatings were deposited with spin-coating at different speeds for 90 s. The temperature of furnace was increased 3° / min until reaching the supposed temperature. The coated samples then underwent a heat treatment at temperature in the range of 473-673 K for 1 hour in a Nabertherm Controller P320 furnace. Mixed oxide layers were heated at 393-473 K for 2 hours. Effect of catalyst and stabilizer amounts were investigated by addition of different molar ratios of each component into the sol solutions.

4.3 Electrochemical Measurements:

A Princeton Applied Research potentiostat “Parstat 2273” and the Power Suite 2.58 Software were used for electrochemical measurements and interpretation. A three electrode setup was used with the coated sample as the working electrode, a platinum counter electrode and a saturated Ag/AgCl reference electrode. Polarization scans were applied between -2 and -1 V with a scan rate of 100 mV/s. As mentioned earlier, porosities act as conductive paths between electrolyte and the substrate. Applying high scan rate can restrict diffusion process and allow the evaluation of the porosity of the film. Current density at 100 mV from OCP ($I_{diss.}$) in anodic direction was selected as a reference point for comparison between uncoated and coated samples as shown in Figure 4.1.

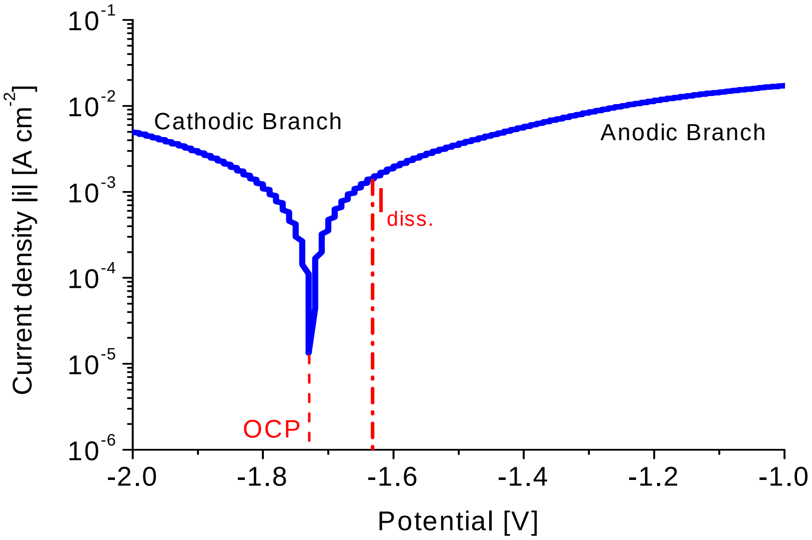

Figure 4.1: Current density vs. potential plot of uncoated magnesium in 0.1 M acetate buffer

In order to evaluate the porosity, a mild environment was chosen. The electrolyte was an acetate buffer containing 0.1 M sodium acetate and 0.1 M acetic acid with a pH of 5.5. To gain information about the resistance of the film in a more aggressive environment, the samples were also measured in a 0.05 M sodium chloride solution.

The corrosion rate of the samples was also investigated by applying Tafel experiments. For this experiment, samples were immersed in the electrolyte for one hour at open circuit potential (OCP) to bring the samples on equilibrium condition. Then a potential scan in the range of -300 mV to +300 mV from OCP at the scan rate of 2 mV/s was applied to the samples and resulting current was monitored. By means of software, a line is calculated for each anodic and cathodic branch of the current density-potential curves.

Using Stern-Geary equation (see 2.3.3) the corrosion current ($I_{corr.}$) can be calculated from the Tafel slopes. $I_{corr.}$ can be then converted into the corrosion rate.

In all impedance experiments, samples were immersed in the electrolyte for different times until equilibrium was established. Electrochemical impedance spectra were then recorded at the OCP after different immersion periods with an AC-amplitude of 20 mV in the frequency range between 200 kHz to 1 mHz. All experiments were carried out at ambient temperature.

4.4 Structure Characterization Methods:

4.4.1 Scanning Electron Microscopy (SEM):

To acquire information about the surface morphology and texture, scanning electron microscopy was used. In this method, the sample is probed by an electron beam scanned across the surface. Different types of radiations from the specimen are displayed. Secondary electron (SE) imaging uses electrons emitted by the specimen with energies between 0 and 50 eV and is the most common mode of operation of the SEM due to several properties:

- These electrons are easy to collect.
- They carry information about the surface topography of the specimen.

Another mode of SEM is backscattered electrons (BSE) which are electrons emitted from the specimen with energies between 50 eV and the incident beam energy E_0. Back scattered electrons carry information about substrates’ atoms and atomic mass.

In our experiment, characterization of surface morphology was done by a high-resolution Scanning electron microscope (HREM) Philips XL FEG and a scanning electron microscope (SEM) ZEISS DSM 962. Both devices are equipped with detectors for secondary electrons (SE) and backscattered electrons (BSE) as well as for energy dispersive X-ray analysis (EDX).

4.4.2 Infrared Spectroscopy:

Infrared spectroscopy is a technique based on the vibrations of the atoms of a molecule. When an infrared radiation passes through of the sample, a fraction of incident radiation absorbed by molecules is converted into energy of either stretching or bending molecular vibration. Different types of bonds and thus different types of functional groups absorb infrared radiation of typical wavelengths which can in turn be used for characterization of material composition. When IR radiation containing a broad range of frequencies passes through a sample, it can be considered as a system of oscillators with resonance frequencies, $\nu_{0,1}$. According to the Bohr rule:

$$\Delta E = h\nu$$

(ΔE is the difference between the ground and excited state, h is Planck's constant and ν the frequency of photons), photons with frequencies $\nu = \nu_{0,1}$ will be absorbed and eliminated from the initial composition of the radiation. Detection of the missing energies as a function of ν enables the identification of excitations. These bands then can be used for obtaining microscopic information about the sample e.g., molecular identity and conformation, intra- and intermolecular interactions and etc.

In our experiments, a Nicolet 5PC spectrometer was used to acquire IR data in the range of 4000-400 cm^{-1}. Dried gel was measured using a potassium bromide (KBr) pellet as matrix.

4.4.3 Secondary Ion Mass Spectrometry (SIMS):

SIMS is a surface technique for the investigation of the chemical composition of solid materials. Under high vacuum, the sample is bombarded with accelerated ions (primary ions). When a primary ion impacts on the surface of the solid, it collides with the sample atoms and loses its energy in a collision cascade until it comes to rest a few tenths of nanometers below the sample surface. The energy released in the collision cascade results in the atom displacements and bonds breaking. Particles at and near the surface can receive sufficient kinetic energy to be emitted as shown in Figure 4.2.[123]

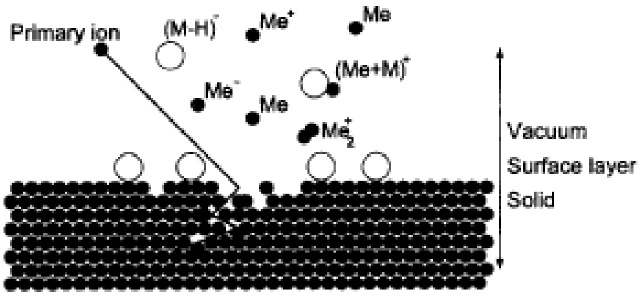

Figure 4.2: The sputtering process which results in releasing positive, negative and neutral particles from the surface

Depending on the intensity, mass, energy and the angle of incident of the primary beam, a thin layer of atoms or molecules of substrate is removed. This sputtering process results in the emission of secondary ions which are separated according to their mass-to-charge ratio by a mass spectrometer, and the mass selected secondary ions are registered by a suitable detector. Resulting graph is the intensity of the sputtered ions versus sputtering time which can be used for characterization of elements of a thin film.

In our experiments, a secondary ion mass spectrometer ims5f type (Cameca, France) was used. The secondary ion masses were analyzed by a double focusing sector field mass spectrometer. The sputter crater size was 150 x 150 µm and the beam diameter was about 20 µm. The measurements were done with O^- or Cs^+ primary ions for positive and negative secondary ions, respectively.

4.4.4 X-Ray Diffraction Analysis (XRD):

X-ray beams are emitted due to the bombardment of a material with high-energy electrons, protons, deuterons, α-particles, or heavier ions. X-rays usually have a wavelength between 0.05 and 100 Å. When X-rays interact with matter, a variety of processes may appear including reflection, refraction, diffraction, scattering, absorption, fluorescence and polarization. Each of these processes can be used to study particular properties of the material. The diffraction of X-rays is a consequence of two different phenomena: (a) scattering at each individual atom and (b) interference of the scattered waves. According to Bragg's law, when the difference between the incident and diffracted waves is an integral multiple of the wavelength of the X-rays, constructive interference occurs and a beam of enhanced intensity is seen which is illustrated in the 2D representation in Figure 4.3. [124]

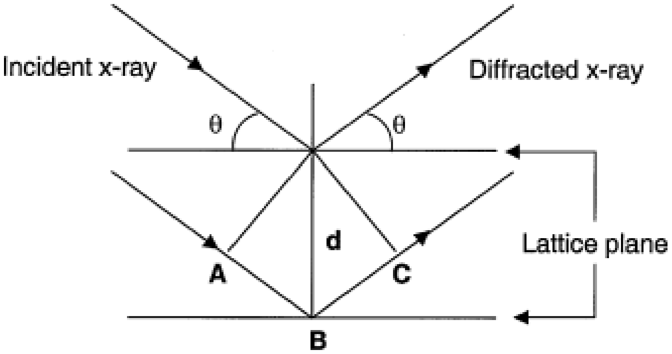

Figure 4.3: The Bragg diffraction condition

The basic step in X-ray crystallography involves measuring the intensity of the diffracted X-rays at various angles. This diffracted intensity depends on the intensity of the incident beam and the concentration of electrons along a given plane in the crystal. It is possible to determine the crystalline structure from this information. In our experiments a SEIFFERT PTS 3003 diffractometer with Cu-K_α radiation was used in 2θ omega geometry to characterize the films.

5. Results and Discussion

5.1 Properties of Bare Magnesium:

In order to receive reliable and reproducible results, the effects of several parameters were firstly investigated on bare magnesium samples. As explained earlier, magnesium dissolution in aqueous environment produces magnesium hydroxide and hydrogen gas. The pH of the buffer solution has a considerable effect on the corrosion rate of magnesium. However, it is very difficult to keep it constant because the corrosion products of magnesium readily dissolve into the solution which results in substantial pH increase. At pH of above 11, a stable and self-healing passive layer develops, which is responsible for the high corrosion resistance in alkaline solutions. The layer varies between a stable and an unstable state for a pH in a range of 10–11. The corrosion rate is controlled by diffusion and depends mainly on the layer thickness. During the dissolution and hydrogen development, the pH rises in the near surface regions. The result is a change in the formation of the layer and a higher stability.

A solution containing buffer agents such as acetate allows pH to remain at a constant value and is expected to enable exact corrosion-resistance measurements. Solution of 0.1 M acetate buffer was used as electrolyte. Electrochemical measurements were done at four different pHs in the range of 5-7. Figure 5.1 shows the resulting current densitiy-potential plots. In acetate buffer and around the neutral pH, formation of natural hydroxide film increases the corrosion resistance of magnesium. On the other hand, low current density of neutral pHs makes it difficult for comparison of coated and bare samples. Therefore, pH = 5.5 was selected as optimal condition for our next experiments. Corrosion of magnesium samples were also tested at two different concentrations of NaCl solution (Figure 5.2). It can be seen that no pitting corrosion occurs on magnesium samples and increasing the concentration of chloride ions into the solution increases the corrosion rate of magnesium.

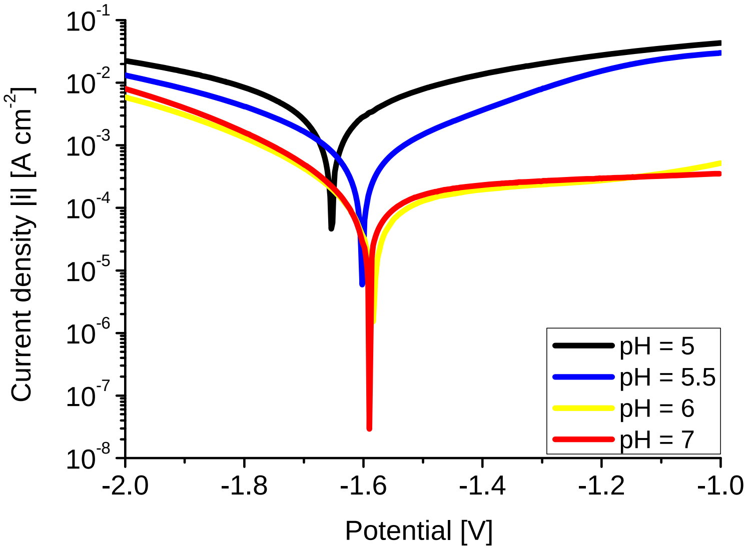

Figure 5.1: Current density-potential curves of uncoated magnesium in 0.1 M acetate buffer at four different pHs

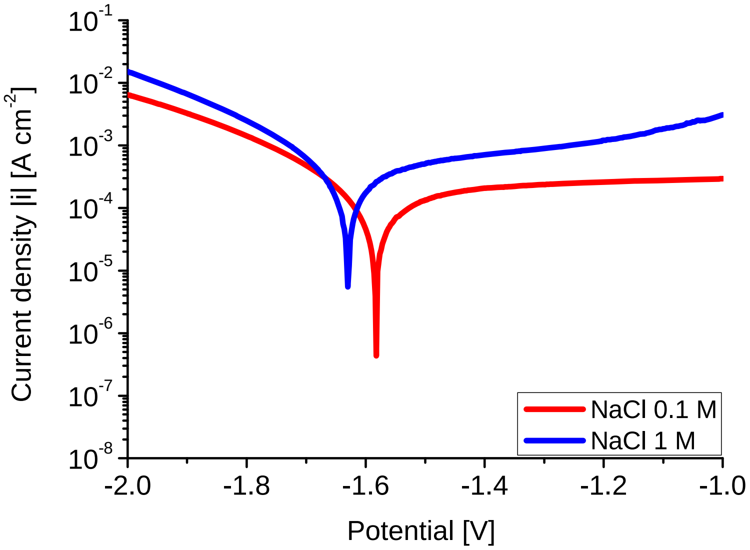

Figure 5.2: Current density-potential curves of uncoated magnesium in two different concentrations of chloride ions

It is also well known that the dissolution of a metal is proportional to the temperature of the environment i.e. at higher temperature, higher corrosion of metal occurs. Effect of the electrolyte temperature on the corrosion of magnesium was investigated at four different temperatures in 0.1 M acetate buffer pH=5.5. Figure 5.3 shows current density-potential plots of these measurements. From plots, it is clear that the temperature of the electrolyte in the investigated range has small effect on the corrosion of magnesium which can be neglected. The same behavior was obtained for 1 M NaCl solution at different temperatures.

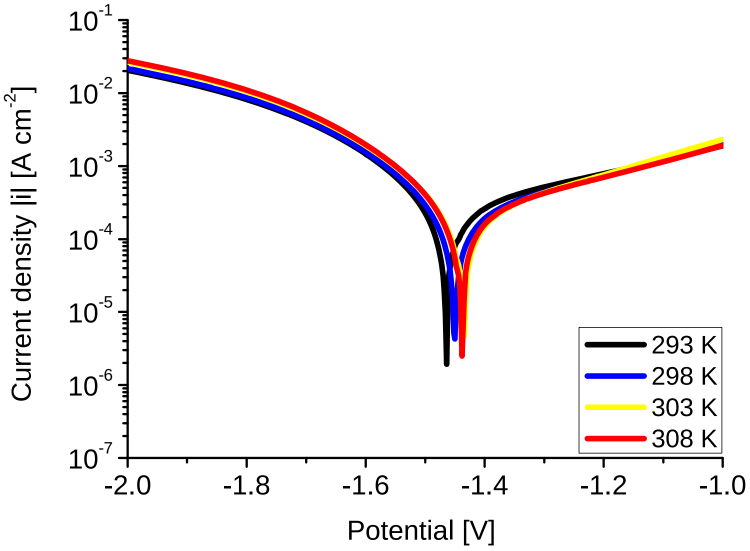

Figure 5.3: Current density-potential plots for magnesium samples immersed in 0.1 M acetate solution at four different temperatures

5.2 Zirconia Sol-Gel:

5.2.1 Effect of Spin Speed:

As described by Bornside [88] for spin-coated films, the thickness of the resulting film depends on the speed of the spinning i.e. at higher speed a thinner film obtains. For corrosion protection purposes, this film behaves as a barrier against environment to prevent the diffusion of electrolyte species onto the metal surface. Generally, one can expect better protection at lower speed because of obtaining a thicker film. On the other hand, weak centrifugal forces at very low speeds make it impossible to obtain homogeneous film. At rather low speed, the sol will adhere to the surface and cannot disperse at the whole area. Therefore, an optimized speed must be applied to the sample to obtain a homogenous film with appropriate thickness. Dependence of the zirconia film thickness on spin speed is shown in Figure 5.4.

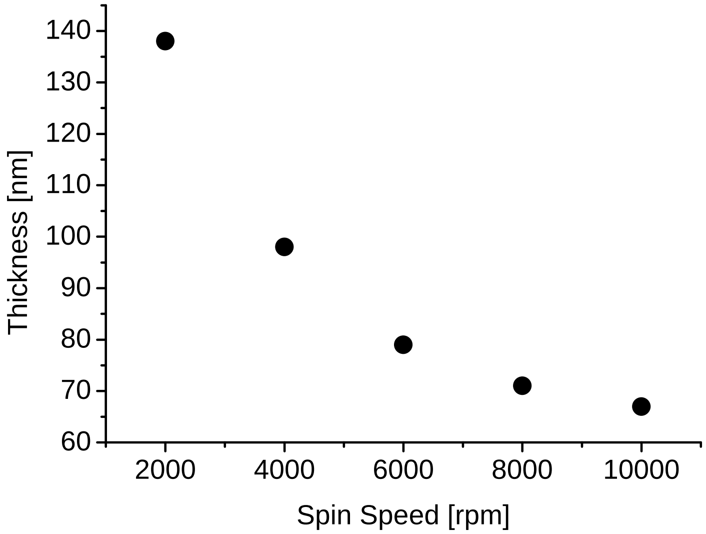

Figure 5.4: Effect of spin speed on the thickness of the deposited film after heat treatment at 573 K

As can be seen, up to 6000 rpm, increasing the speed decreases the film thickness and between 6000-10000 rpm the thickness changes slightly. At 2000 rpm, the weak centrifugal forces results to the formation of inhomogeneous films. In order to obtain a homogenous film with the appropriate thickness, 4000 round per minute (rpm) was selected for further experiments.

Figure 5.5 shows the current density-potential plots of zirconia deposited samples heated at 573 K for 1 hour at four different spin speeds.

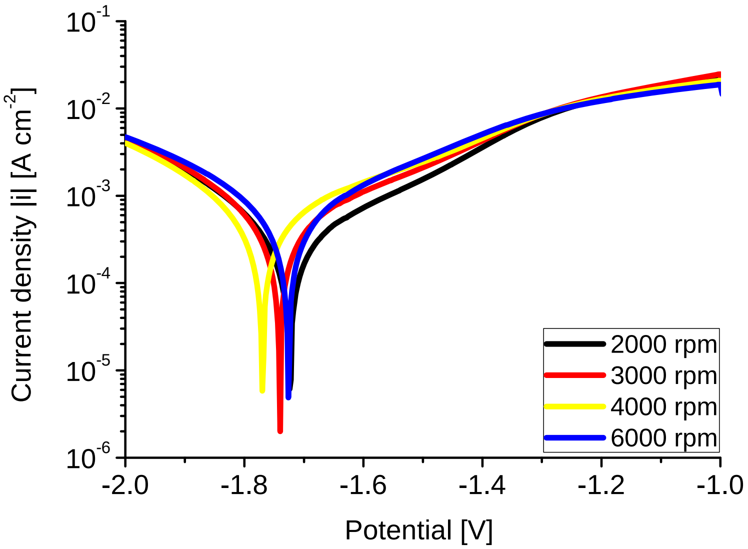

Figure 5.5: Current density-potential plots of zirconia deposited samples in 0.1 M acetate buffer at different spin speeds and heated for 1 hour at 573 K

For comparison, current densities of deposited samples at $I_{diss.}$ of different spin speeds is shown in Table 5.1.

Spin Speed (rpm)	2000	3000	4000	6000
$I_{diss.}$ (Acm^{-2})	$5.53*10^{-4}$	$9.35*10^{-4}$	$8.78*10^{-4}$	$4.63*10^{-4}$

Table 5.1: Current density of zirconia coated samples at $I_{diss.}$ of different spin speeds measured in 0.1 M acetate buffer after heat treatment for 1 hour at 573 K

From the similar plots and $I_{diss.}$, it is obvious that the thickness of the coating makes no significant difference on the corrosion ability of the zirconia film on magnesium.

5.2.2 Effect of Heating Temperature:

The annealing temperature has a strong effect on the final structure of the sol-gel film. It defines the density and interconnectivity (porosity) of the system which at last shows its ability to suppress the corrosion of a metal. The melting point of magnesium at 773 K restricts higher temperatures application. In order to obtain the best film by sol-gel process, temperature has to be adjusted in the range that results in the formation of denser film with good adhesion to the substrate.

Figure 5.6 shows the dependence of the thickness on annealing temperature for samples deposited at 4000 rpm.

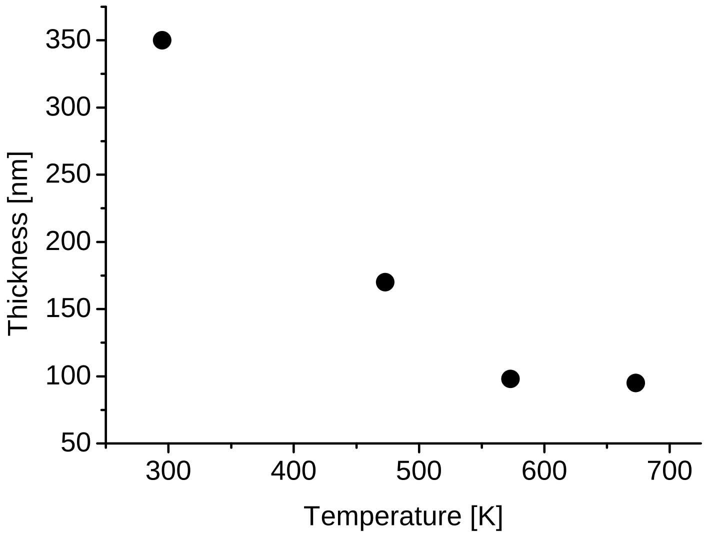

Figure 5.6: Effect of heating temperature on the thickness of zirconia deposited film on magnesium

As can be seen, denser film obtains at higher temperatures. Figure 5.7 shows the electrochemical measurements of magnesium samples coated with zirconia after heat treatment at three different temperatures.

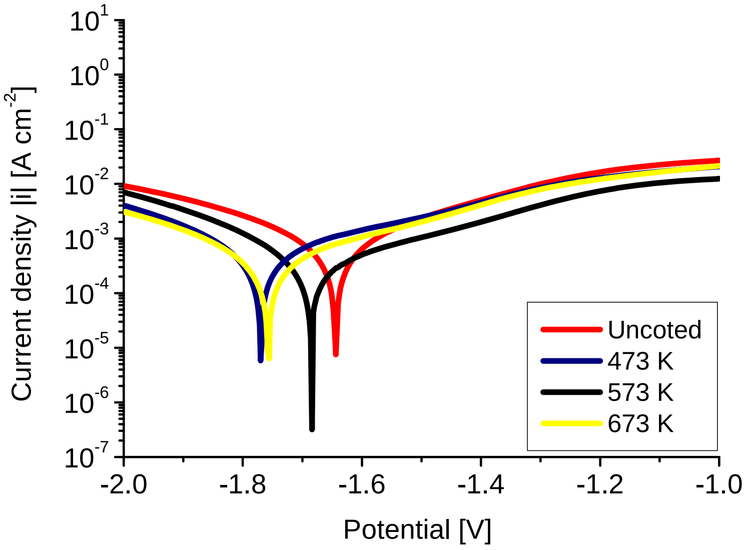

Figure 5.7: Current density-potential plots of magnesium samples coated with zirconia annealed at three different temperatures for 1 hour

At higher temperature, evaporation of organic residues results in the formation of denser film structure with lower porosity. From the porosity evaluation, one would expect that at higher temperature a better protection is achieved.

However, from the electrochemical results, it can be concluded that the coating provides no distinct enhancement on the corrosion prevention of magnesium. For comparison, the Magnesium dissolution current densities ($I_{diss.}$) at different temperatures are shown in Figure 5.8.

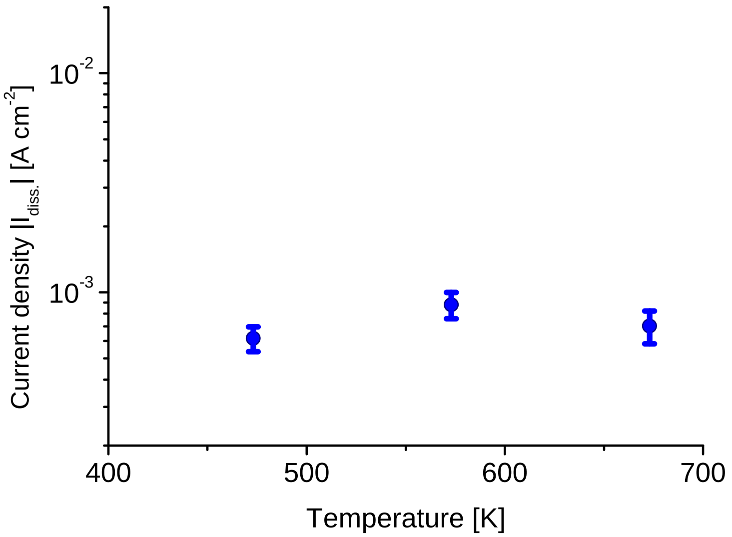

Figure 5.8: Effect of heating temperature on the corrosion protection of zirconia-coated samples in 0.1 M acetate buffer

Despite its larger thickness, the sample formed at 473 K does not show lower porosity. There is only a minor improvement found for intermediate temperature. The main reason for this finding can be referred to the adhesion of the deposited film on magnesium, presumably due to the thermal mismatch between the coating and substrate. During the heat treatment process, thermal mismatch between magnesium and zirconia leads to an increase in stress within the film which at last causes the film to peels off from the substrate. It has been shown that a zirconia film formed on iron samples is able to improve the corrosion resistance of iron samples. [125] To compare adhesion of zirconia film on magnesium and iron samples, similar sol-gel solution was deposited onto the magnesium, iron and silicon wafers and surface characterization methods were used to characterize the properties of the coating.

5.2.3 Scanning Electron and Optical Microscopy Pictures:

Figure 5.9 shows scanning electron microscope pictures of uncoated iron and magnesium samples. It is clear that in the case of uncoated samples, surfaces are very smooth and there are no holes or scratches on the surfaces.

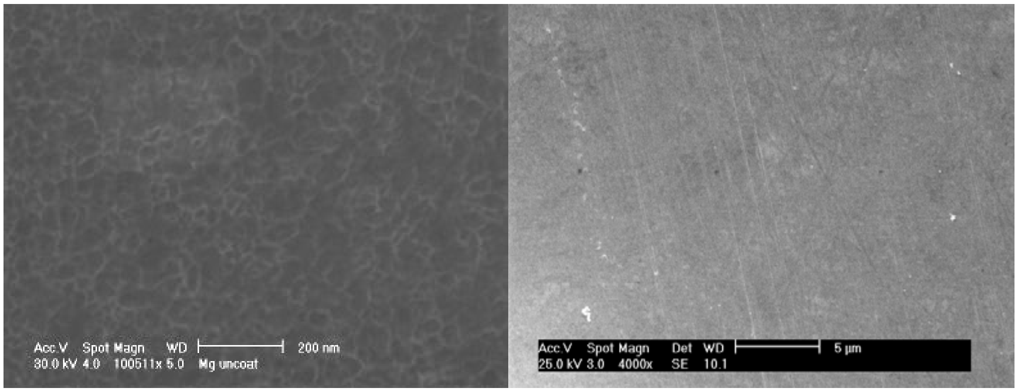

Figure 5.9: SEM pictures of uncoated magnesium (left) and Iron (right) samples

Figure 5.10 shows SEM pictures of zirconia coated samples heated at 573 K for 1 hour. Despite of the iron in which the coated layer is smooth and crack-free, in the case of magnesium, coating is not homogeneous and there are a lot of spaces with no coating. These areas can act as the starting point for magnesium corrosion and can explain the absence of protection on magnesium coated samples.

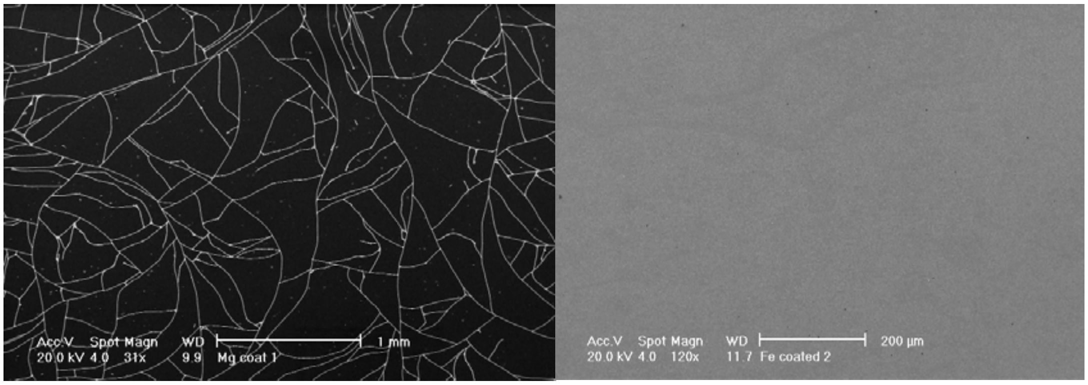

Figure 5.10: SEM pictures of coated magnesium (left) and Iron (right) samples

Figure 5.11 shows optical microscopy pictures of zirconia coated silicon wafer, Fe and Mg samples. Both iron and silicon wafer samples show good adhesion between substrate and the coating. In contrast, in the case of magnesium samples, the coating has spalled from the substrate. This behavior can be attributed to the weak adhesion between the coating and substrate which is not sufficient to resist the intrinsic film stress.

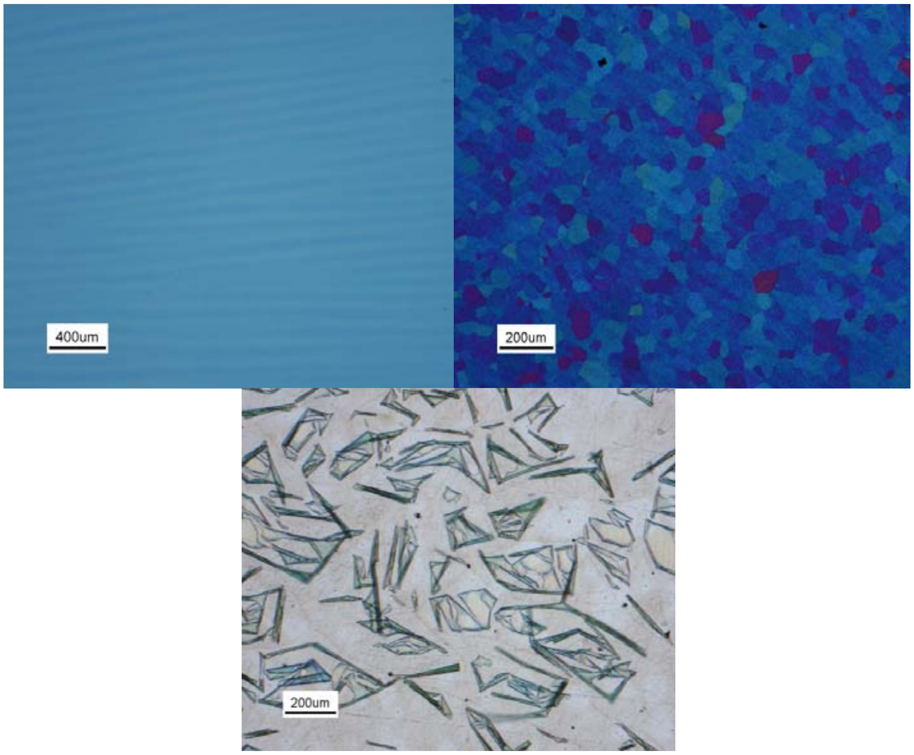

Figure 5.11: Optical microscope pictures of zirconia coated silicon (left), iron (right) and magnesium (middle) heated at 573 k for 1 hour

SIMS results also backed up the inhomogeneous distribution of zirconia on magnesium surface in which 2 types of magnesium depth profile relating to the coated and uncoated parts is obtained. Figures 5.12 and 5.13 show the SIMS depth profiles of iron and magnesium samples coated with zirconia and heat treated at 573 K for 1 hour. In the case of iron sample, two separate layers are recognizable. From the surface, a zirconium oxide layer followed by a mixed iron and zirconium oxide layer has been built on iron. Decreasing the intensity of oxygen and zirconium at around 1500 s shows the end of the coating where by reaching to the substrate, the intensity of iron stays constant. Contrary, in the case of magnesium (Figure 5.13), a higher intensity of magnesium compared to the iron shows that from the very beginning of the sputtering, magnesium is detectable which proves the partial coverage of the magnesium sample with the coating.

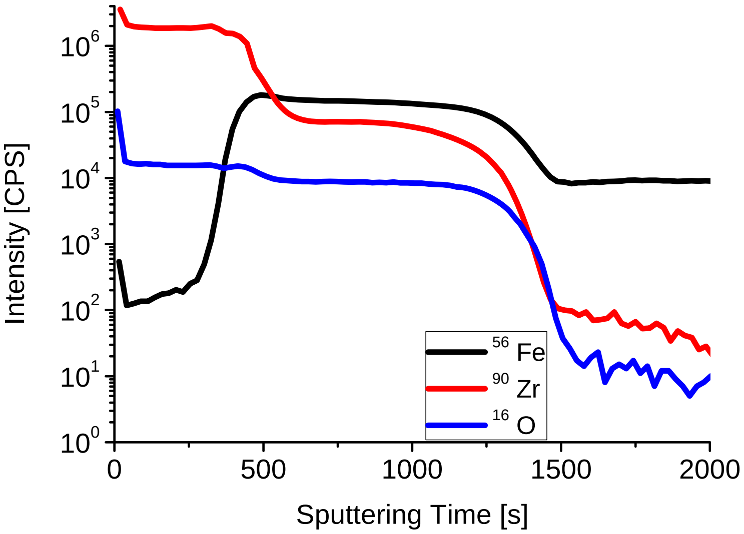

Figure 5.12: SIMS depth profile of iron sample coated with zirconia and heat treated at 573 K for 1 hour

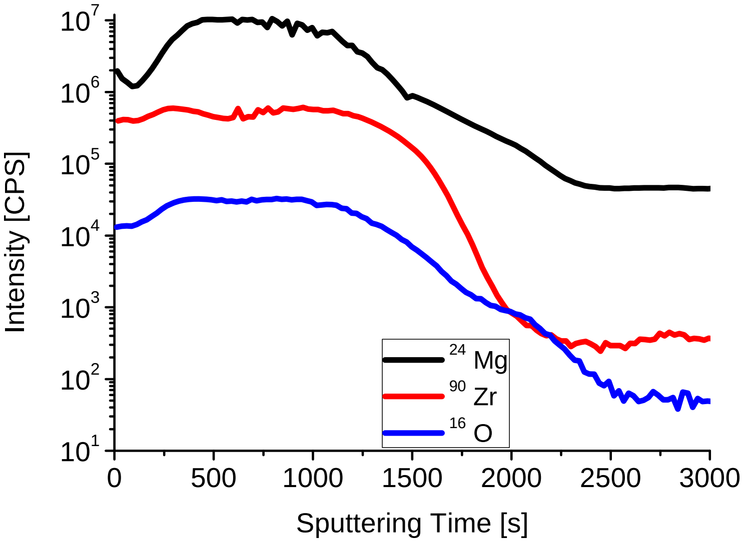

Figure 5.13: SIMS depth profile of magnesium sample coated with zirconia and heat treated at 573 K for 1 hour

The distribution of the coating on magnesium samples can be divided to two parts. Uncoated parts where no zirconium signal can be detected and coated part where a weak intensity of zirconium can be recognized. Figure 5.14 shows the linear scale distribution of zirconia for the sample annealed at 573 K. It can clearly be seen that just small portion of magnesium has been covered by zirconia and most areas are susceptible to corrosion attack.

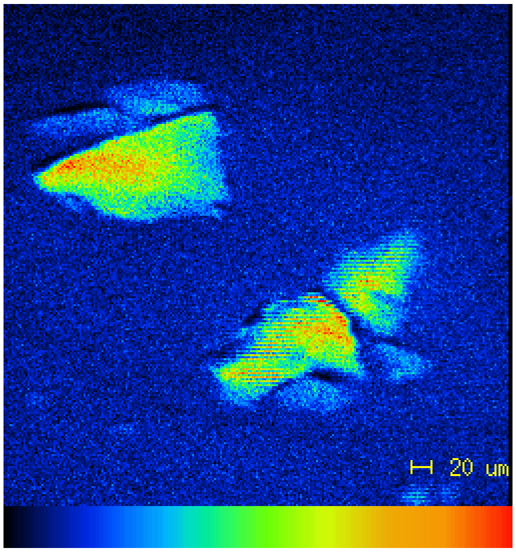

Figure 5.14: Linear scale distribution of magnesium sample deposited with zirconia after 1 hour heat treatment at 573 K (black bar the lowest and the red one the highest intensity)

Bad adhesion between the film and substrate can be related to the discrepancy between the expansion coefficient of magnesium substrate (26.1 x 10^{-6} K^{-1}) and the zirconia coating (5.6 x 10^{-6} K^{-1}). During thermal treatment, the high volume alteration of the substrate results in stresses with and within the coating material which leads to the formation of cracks. As the film solidifies, shrinkage can no longer be relieved by flow and tensile stress is developed in the plane of the substrate. The critical thickness for crack propagation or the growth of pinholes for well adherent film is given by: [126-127]

$$h_c = \left(\frac{K_{Ic}}{\sigma\Omega} \right)^2$$

where K_{Ic} is the critical stress intensity and Ω is a function that depends on the ratio of the elastic modulus of the film and substrate. When the thickness exceeds the critical value, cracking occurs which consequently results in the delaminating of the film. The thermal mismatch between the film and substrate increases the amount of the stress which in turn reduces the critical thickness amount. Several strategies have been used in order to overcome this problem such as reducing the volume fraction of solvent at the solidification point and reducing the film thickness. However, none gave satisfying results. Therefore, in the next step, a combination of two precursors was tried.

Silane coupling agents (with the general formula of R_3SiX) belong to a class of organosilane compounds having at least two reactive groups of different types bonded to the silicon atom in a molecule. One of the reactive groups of different types (R for example methoxy, ethoxy and silanolic hydroxy groups) is reactive with various inorganic materials such as glass, metals, silica sand and the like to form a chemical bond with the surface of the inorganic material while the other reactive groups (X for example vinyl, epoxy, methacryl, amino and mercapto groups) is reactive with various kinds of organic materials or synthetic resins to form a chemical bond. As a result of possessing these two types of reactive groups, silane coupling agents are capable of providing chemical bonding between an organic material and an inorganic material. [128]

For the next step and in order to improve the adhesion of zirconia to the magnesium sample, silane coupling agent containing phenyl group was mixed to the zirconia sol solution and its effect on porosity and corrosion resistance of the film was investigated.

5.2 Phenyl-triethoxysilane (PTES):

5.2.1 Combination of zirconium with PTES:

The effect of silicon addition on adhesion of zirconia to the substrate was investigated by providing a hybrid sol-gel containing both components. Figure 5.15 shows the current density-potential plots of magnesium samples coated with hybrid solution at different zirconium ratios in 0.1 M acetate buffer after heat treatment at 573 K for 1 hour.

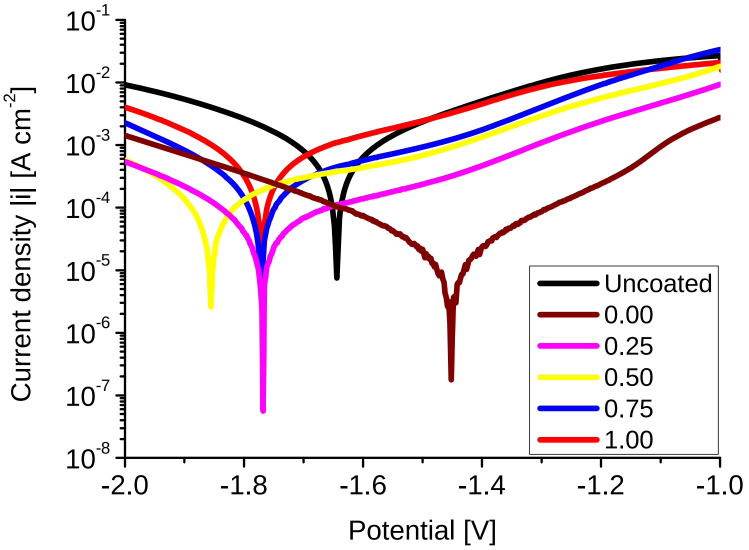

Figure 5.15: Current density-potential plots of magnesium samples coated with hybrid solution in 0.1 M acetate buffer heat treated at 573 K for 1 hour

Figure 5.16 shows the current densities at I_{diss}. for five different zirconium molar ratios. As can be seen, addition of silicon to the zirconia sol solution decreases the current density. It turned out that any content of zirconium in the sol lead to higher current density than the Si-based sol alone. The best result was obtained in the absence of zirconium precursor. At this stage, experiments on zirconium were given up and the work was concentrated on Si-based precursors.

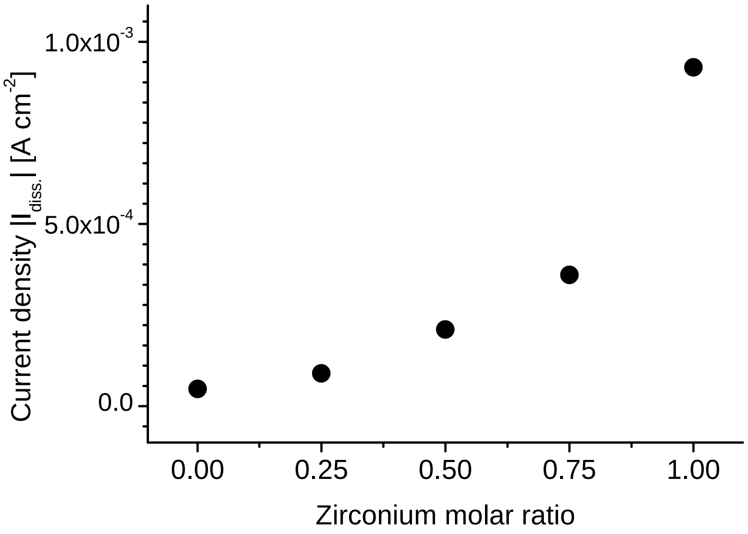

Figure 5.16: Effect of zirconium molar ratio on the current density of sols in 0.1 M acetate buffer after heat treatment at 573 K for 1 hour

5.2.2 Optimization of PTES Sol Solution:

Acid is often used in sol-gel chemistry to accelerate the rate of hydrolysis reaction. Its effect can be easily explained in terms of protonation of alkoxy groups and providing better leaving groups which leads to the substitution of OR groups by OH group. [129] Metal alkoxides react with organic acids according to the reaction:

$$M(OR)_n + x\,RCOOH \longrightarrow M(OR)_{n-x}\,(OOCR)_x + x\,ROH$$

It has been shown that acetate groups behave as bidendate ligands which attacks the alkoxy groups on the alkoxide before water and cannot be removed by water. This enables the control of both hydrolysis and condensation reaction. [130] Reaction of acetic acid with silicon alkoxides can be shown as:

$$Si(OR)_4 + n\,AcOH \rightleftharpoons Si(OR)_{4-x}(OAc)_x + x\,ROH + (n-x)\,AcOH$$

However in the access of acetic acid, it can react with alcohol to form the ester:

$$C_2H_5OH + CH_3COOH \rightleftharpoons CH_3\text{-}COO\text{-}C_2H_5 + H_2O$$

Consequently, water can prompt further hydrolysis of silicon alkoxide which can result in the formation of unwanted products. Therefore, an optimized amount of acid has to be added to the solution to control the rate of hydrolysis and condensation reactions and to inhibit unwanted reactions to occur. In order to investigate the effect of acid catalyst, several sol solutions containing different molar ratios of acetic acid were prepared and added to the solution of PTES. Table 5.2 summarizes the relative molar ratio of sol solution constituents.

Sol	PTES	AcAc	Propanol	Water	AcOH
A	1	2	4	1	0
B	1	2	4	1	1
C	1	2	4	1	2
D	1	2	4	1	3

Table 5.2: The molar ratio of different sols containing different amount of acetic acid (AcOH)

Figure 5.17 shows the current density-potential plots of PTES-coated samples after heating at 573 K for 1 hour. As can be seen, the addition of acetic acid to the sol-gel solution in the range of 1-3 molar ratios compared to the bare magnesium does not improve the porosity situation of the coating on magnesium since all current densities are in the similar high range. Indeed, the protection performance is even better without any acetic acid addition. In this case, the current density is decreased by 3 orders of magnitude. This means that acetic acid is detrimental for the porosity of the coating. Without the presence of acetic acid the risk of acidic corrosion reactions on the metal surface during the deposition process can also be eliminated. Pratt et al.[105] explained this behavior by the fact that in the presence of acetate and at the pH below 6 buffers catalysis is impossible to detect. Therefore they suggested the hydrolysis reaction proceeds by base catalysis mechanism and showed that acetate buffer has no effect on hydrolysis reaction rate.

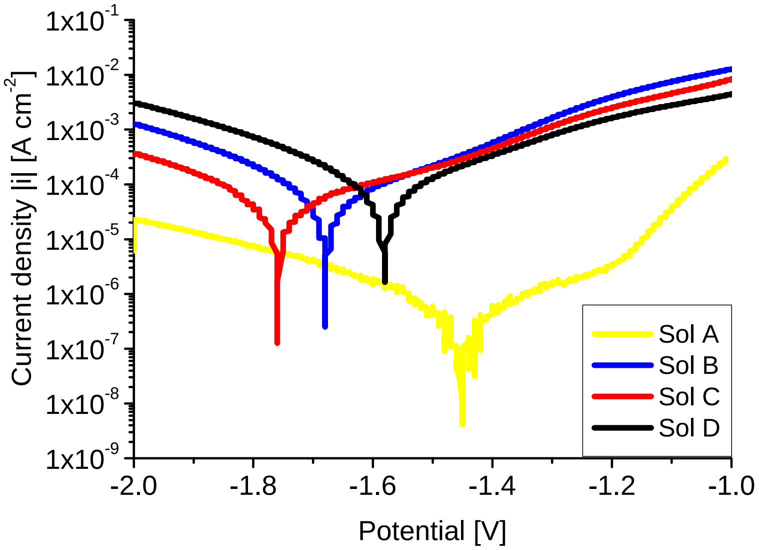

Figure 5.17: Effect of acetic acid molar ratio on the current density of PTES-coated samples in 0.1 M acetate buffer solution after heating for 1 hour at 573 K

The effect of acetylacetone (AcAc) on the final structure of the sol solution was investigated by providing different solutions containing different acetylacetone molar ratios (Table 5.3).

Sol	PTES	Propanol	Water	AcAc
E	1	4	1	0
F	1	4	1	1
G	1	4	1	2
H	1	4	1	3

Table 5.3: The molar ratio of different sols containing different amount of acetylacetone

β-diketons exhibit keto-enol tautomerism:

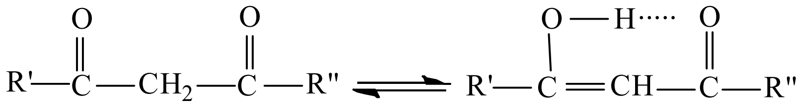

The enol form contains a reactive hydroxyl group which reacts readily with alkoxides providing a structure where the enol form of the β-diketons is stabilized by chelating of the metal ion. In acetylacetone, the metal alkoxide is stabilized by the formation of a six-member ring which is very stable toward the nucleophilic attack.

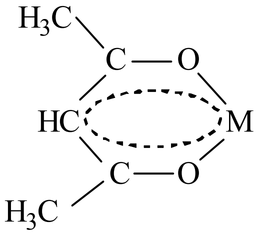

Figure 5.18 shows current density-potential curves of sols E-H for PTES-coated samples heat treated at 573 K. Increasing the amount of acetylacetone decreases the porosity of coated magnesium samples. The best result is obtained at 1:2 PTES:AcAc molar ratio evaluating from its minimum current density. For a better illustration, in Figure 5.19 the magnesium dissolution current densities taken at $I_{diss.}$ vs. the molar content of AcAc is shown. This behavior can refer to the role of acetylacetone to decrease the rate of hydrolysis reaction and to provide denser and better connected network which decreases the porosity of the deposited film. Higher concentration of acetylacetone can result in the formation of bulker material during the sol-gel process which results in the formation of films with larger porosities. Therefore, the corrosive medium has easier access to the substrate which enhances the susceptibility of material to corrode.

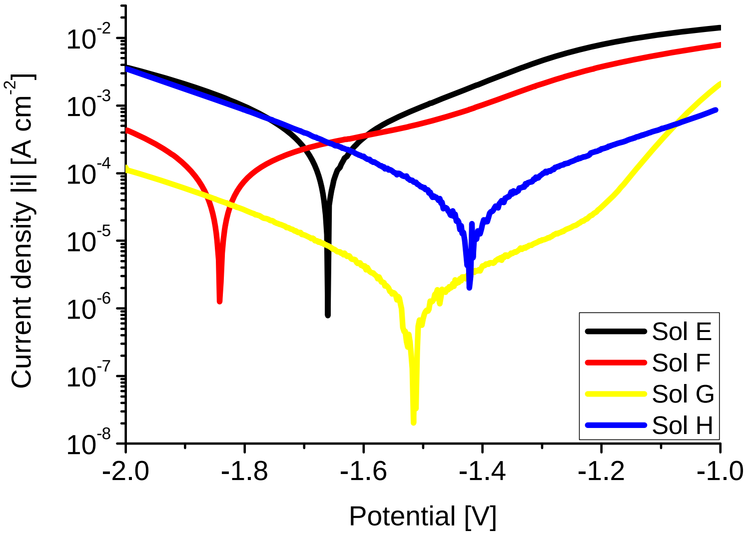

Figure 5.18: Effect of acetylacetone on the current densities of PTES-coated samples in 0.1 M acetate buffer after heating for 1 hour at 573 K

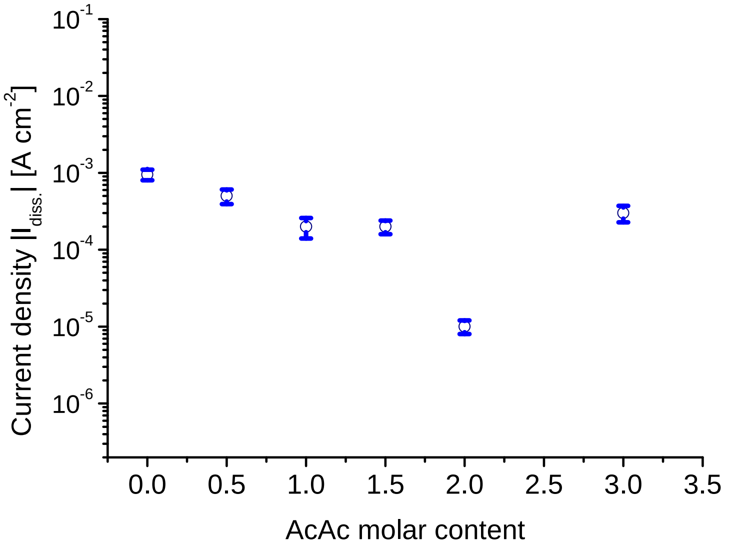

Figure 5.19: Current densities at $I_{diss.}$ for sols with different acetylacetone molar content treated at 573 K for 1 hour

The effect of water content on the porosity of the film was also investigated. Figure 5.20 shows the current density-potential plot of deposited samples prepared with different water-propanol molar ratios.

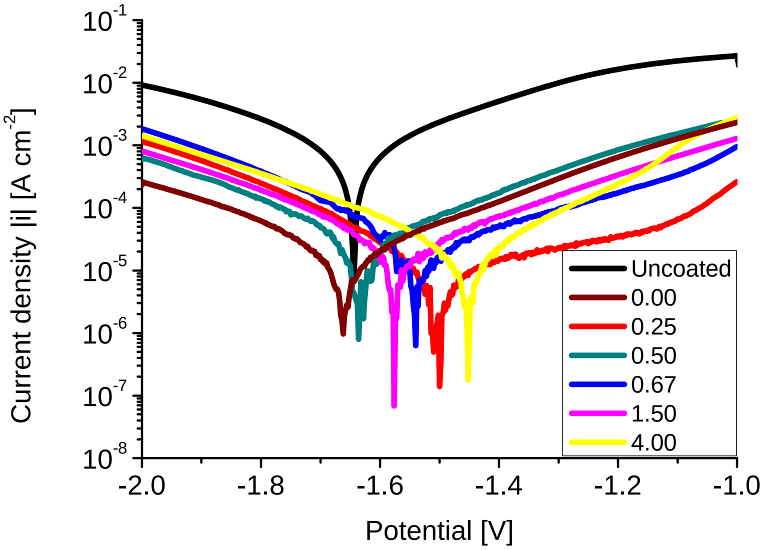

Figure 5.20: Current density-potential plots of PTES-coated samples prepared at different water-propanol molar ratios in 0.1 M acetate buffer after heat treatment at 573 K for 1 hour

Figure 5.21 shows the current densities ($I_{diss.}$) of samples prepared at different water-propanol molar ratios.

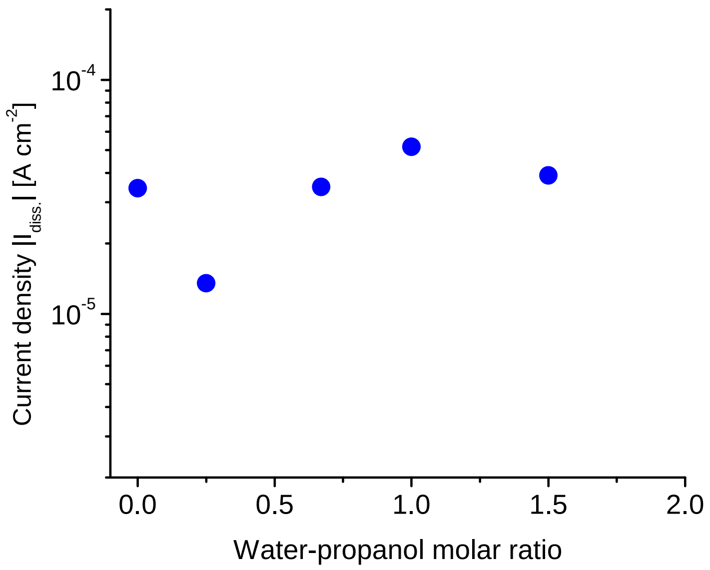

Figure 5.21: Current densities at $I_{diss.}$ for PTES-coated samples prepared with different water-propanol molar ratios treated at 573 K for 1 hour

It is well established that the hydrolysis reaction rate is first order with respect to the water amount under acidic catalysis. [131] Comparison between current densities shows that the addition of higher amount of water leads to an increase of porosity due to the higher hydrolysis rate which prevents the formation of a highly cross-linked coating and leads to the less protection performance. Therefore an optimized amount of water must be added to the solution to balance the hydrolysis and condensation reaction in which the best protection can be obtained. From graphs, it is clear that the solution containing 0.25 water-propanol molar ratio provides the best protection.

Figure 5.22 shows current densities ($I_{diss.}$) of coated samples heat treated at different temperatures in the range of 523 to 673 K for solution made at optimized amount of acetic acid, acetylacetone and water-propanol molar ratios.

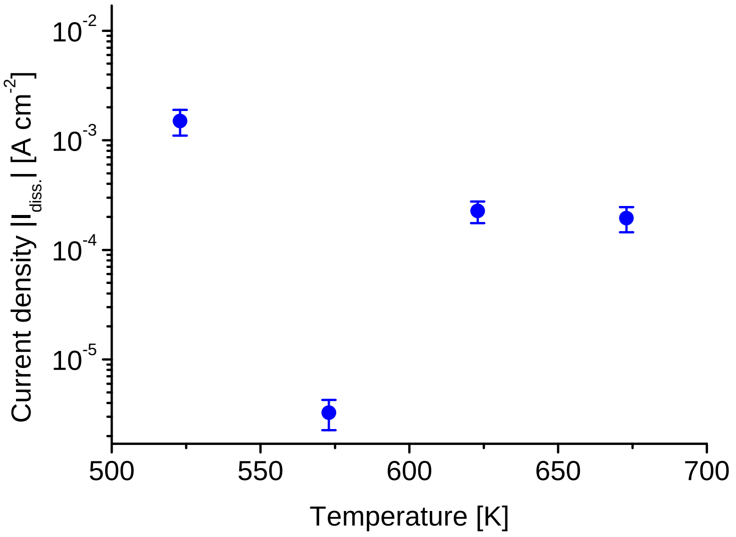

Figure 5.22: Effect of heating temperature on corrosion protection of PTES-coated sample in 0.1 M acetate buffer

The ideal process temperature should be as low as possible to prevent the sample from suffering structural damage and as high as necessary to ensure enough density and mechanical stability of the coating. Porosity of the film after heating at 523 K is very poor. At 573 K the current density of the coated sample decreases strongly but then increases again for higher heat treatment temperatures. On one hand in sol-gel processes, high temperatures can provide films with lower porosity and higher density. On the other hand, a mismatch of coefficients of thermal expansion of substrate and coating can cause stress during the heat treatment and results in crack formation or poor adhesion between the metal surface and the protective film. In our case obviously 573 K represents the optimum process temperature with the lowest porosity.

Ability of our system at optimized parameters against corrosion was also examined in a more aggressive chloride environment. The higher aggressiveness of chloride against oxide layer leads to the local attack and the dissolution of the oxide. As shown in Figure 5.23 the current density of the coated sample is about 2 orders of magnitude lower than the current density of bare sample which proves good protection ability of the coating in the chloride medium.

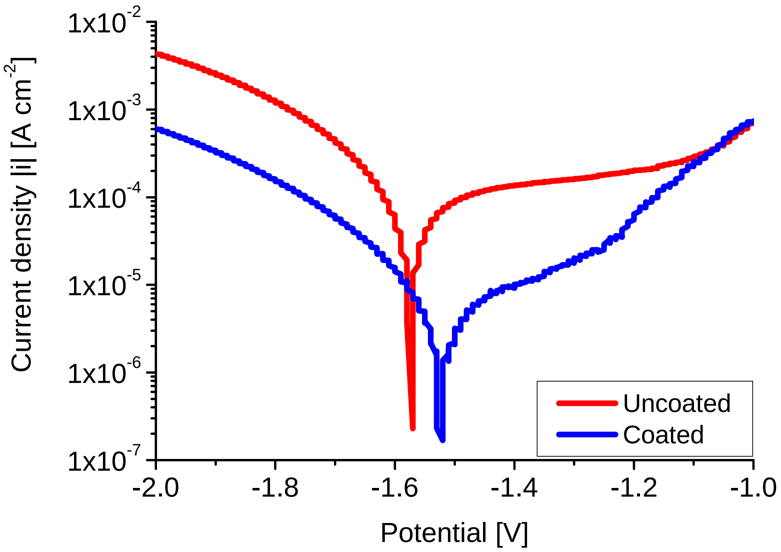

Figure 5.23: Electrochemical measurements of bare and PTES-coated magnesium samples in 0.05 M sodium chloride solution after heat treatment at 573 K for 1 hour

The scanning electron microscope pictures of PTES-deposited magnesium samples in both acetate and chloride solutions after one hour immersion is shown in Figure 5.24. It is clear that the adhesion between the coating and substrate is reasonable also after one hour immersion time with more severe deterioration in chloride solution due to its aggressiveness.

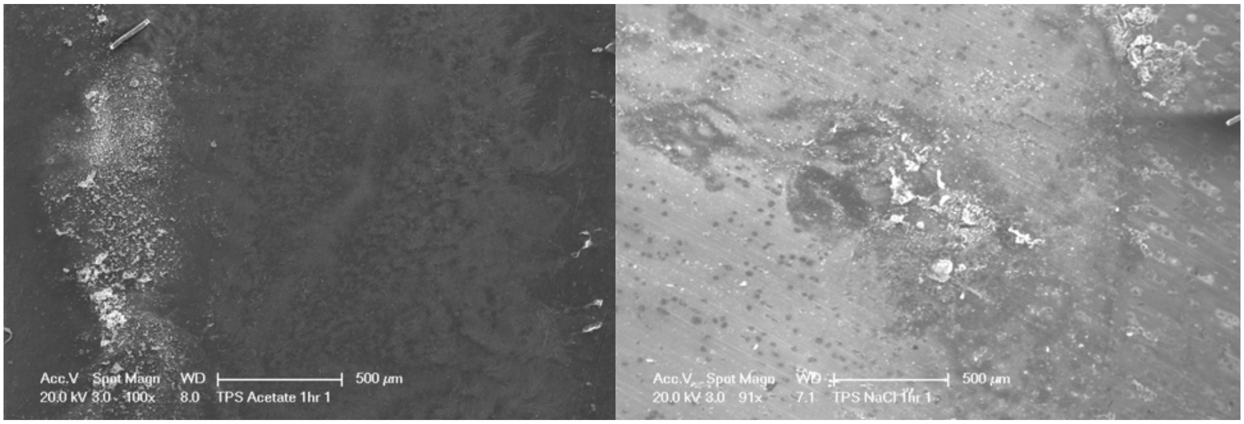

Figure 5.24: Scanning electron microscope pictures of PTES deposited magnesium samples in Acetate (left) and Chloride (right) after one hour immersion

5.2.3 Characterization of Sol-gel Solution:

Figure 5.25 shows the IR spectra of pure PTES, PTES sol and dried gel after heat treatment for 1 hour at 573 K.

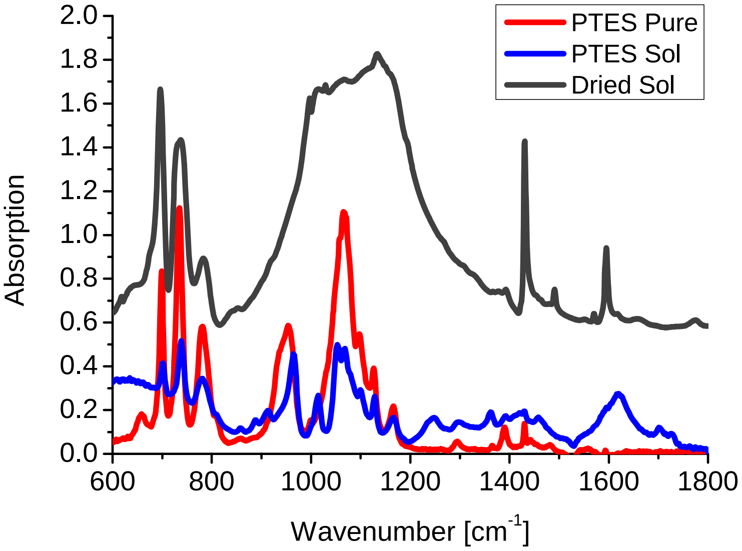

Figure 5.25: Infrared absorption spectra of Pure, Sol and Dried PTES after one hour heat treatment at 573 K

The peaks at 1590 cm^{-1} and 1566 cm^{-1} relate to the ring modulus of the phenyl group with little interaction with CH group. The peaks at 1486 cm^{-1} and 1423 cm^{-1} can be assigned to the ring modulus involving C-C bonds which mix strongly with C-H group. [132] The strong peaks at 784, 738 and 700 Cm^{-1} are also related to the C-C vibration of the phenyl ring. The two strong bands at about 1100 cm^{-1} and 960 cm^{-1} can be assigned to the Si-O-C stretching vibration. [133] Decreasing the intensity of these latter peaks during the sol-gel reaction indicate the formation of Si-O-Si bonds. On the other hand, the weak peak at 660 cm^{-1} disappears during the sol-gel reaction. This weak band can be attributed to the SiOH vibration and its disappearance can be related to the completion of condensation reaction. A similar assignment has been given to the phenylsilanetriol. [134] In the case of dried sol-gel, the absence of the band at 960 cm^{-1} indicated the completion of condensation reaction whereas the presence of the broad band at 1000-1200 cm^{-1} indicated that the solid material contains mostly of Si-O-Si skeleton. The presence of other peaks in dried gel has been related to the residual phenyl group which is stable until 1173 K. [132]

Figure 5.26 shows a depth profile of magnesium ($^{25}Mg^{2+}$, $^{24}Mg^{+}$), silicon ($^{28}Si^{+}$) and oxygen ($^{16}O^{+}$) for a sample treated at 573 K.

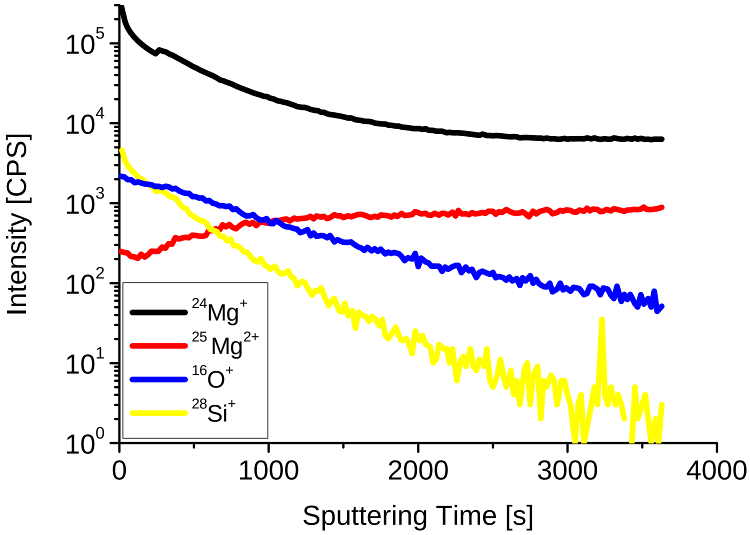

Figure 5.26: SIMS-depth profile of a PTES-coated magnesium sample after heating at 573 K for 1 hour

From the magnesium signal starting at the very beginning of the depth profile with a subsequent slow decrease, it can be concluded that there is not a single homogenous silicon oxide layer on top of the substrate but rather a kind of strong diffusion between Si and Mg. The $^{24}Mg^{+}$ signal also decreases with depth– this, however, is due to the well known dependence of the ionization probability of singly positive charged metal ions on the oxygen content. The $^{25}Mg^{2+}$ signal is more likely to resemble the concentration of Mg in the diffusion layer than the $^{24}Mg^{+}$.

It is well known that SIMS suffers from artifacts and restrictions such as knock-on of atoms effect by energetic ions, leading to an interface broadening, and roughening due to the sputtering. The presence of interlayer can be proved by examining three factors:

- The knock-on effect due to the bombardment with 5.5 keV Cesium (Cs) which will be in the order of a few nm only.

- The surface roughness of the initial surface of about 30 nm limits the depth resolution that is achievable; there might be some roughening during sputter profiling, but usually only with larger depths; so the 30 nm initial roughness cannot explain the signal decrease of Si and O that extends over the whole profile.

- The initial surface roughness of the Mg samples is also not in a region sufficient to affect the profile in this way. Especially the occurrence of Mg right at the beginning of the profile is a clear sign for inter-diffusion. The only other possibility for Mg at the start of the profile would be a partial covering of the substrate which was not observed in the measurements and would also not harmonize with the electrochemical results.

Figure 5.27 shows X-ray diffraction analysis (XRD) for a PTES-coated sample at 573 K in 2 θ omega symmetric scans.

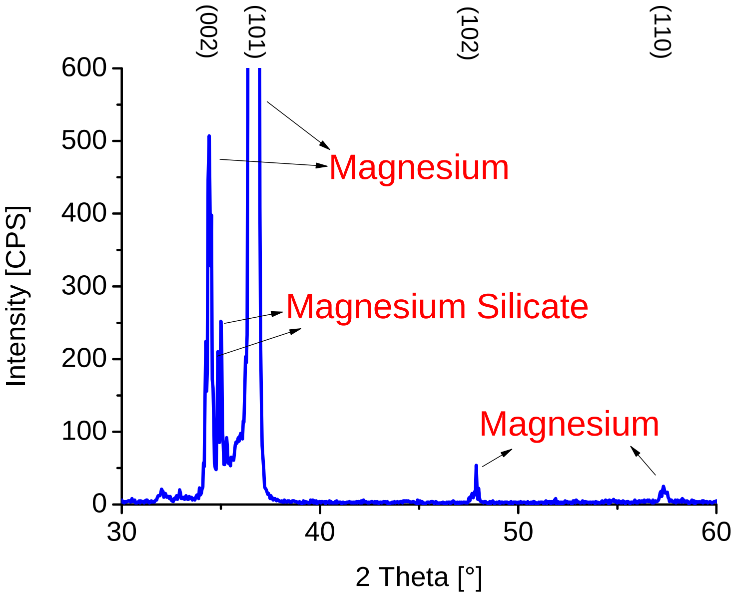

Figure 5.27: XRD analysis of a PTES-coated sample after heating at 573 K for 1 hour using 2 θ omega symmetric scan

Magnesium reflections appear at 35° and 37° with strong intensity. Two additional peaks which can be assigned to magnesium silicate appear after the heat treatment. The appearance of the $MgSiO_3$ phase in correlation with the SIMS results prove a strong diffusion between magnesium and the coating material during the heat treatment resulting in the formation of a mixed oxide layer rather than a pure silicon oxide coating. This interdiffusion layer can act as a good barrier to prevent magnesium corrosion in both mild and chloride solutions.

5.3 3-Glycidyloxypropyltrimethoxysilane (GLYMO):

For the next step, another organofunctional silane compound containing epoxy group was used as precursor and its sol solution deposited on magnesium samples. As explained earlier, the epoxy group of GLYMO undergoes ring opening during the hydrolysis reaction and can act as second functional group to provide better cross-linked network which at last results in a less porous film.

5.3.1 Optimization of Sol-Gel Solution:

Effect of acetic acid amount on the porosity of the final sol-gel film was investigated by preparation of several sols containing different acid molar ratio. (Table 5.4)

Sol	GLYMO	AcAc	Water	Propanol	AcOH
A	1	2	1	4	0
B	1	2	1	4	1
C	1	2	1	4	2
D	1	2	1	4	3

Table 5.4: The molar ratio of different sols containing different molar ratio of acetic acid (AcOH)

Figure 5.28 shows the current density-potential plots of resulting film from different acid molar ratios in 0.1 M acetate buffer after 1 hour heat treatment at 573 K.

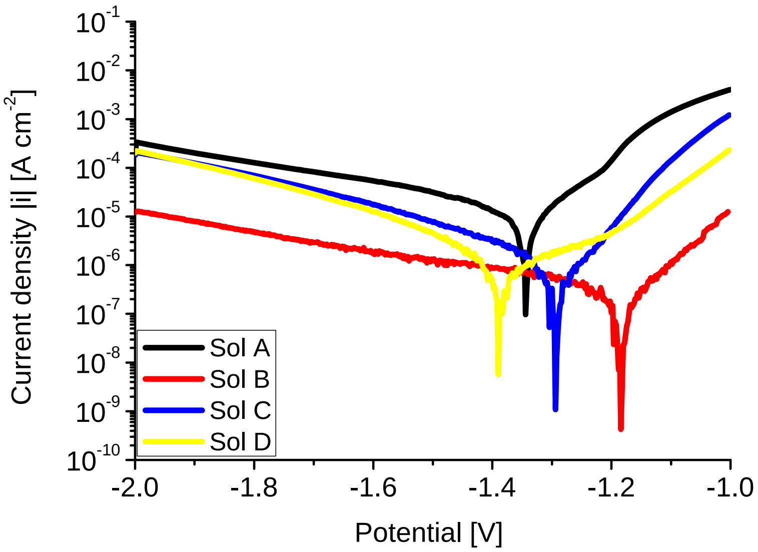

Figure 5.28: Effect of acetic acid molar ratio on the current densities of GLYMO-coated magnesium samples in 0.1 M acetate buffer after heating for 1 hour at 573 K

For better comparison, Figure 5.29 shows the current density ($I_{diss.}$) of samples with different acetic acid molar ratios.

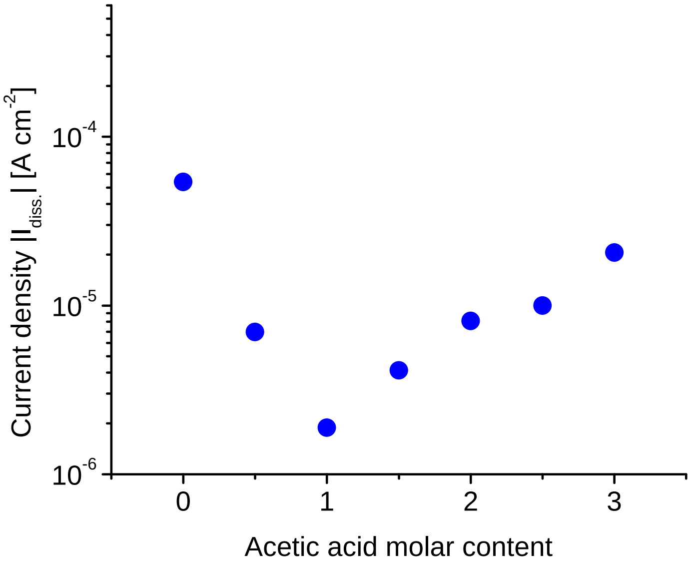

Figure 5.29: Current density at $I_{diss.}$ for GLYMO-coated samples containing different acetic acid molar ratio in 0.1 M acetate buffer after heating for 1 hour at 573 K

As can be seen, adding of 1 molar ratio of acetic acid decreases the current density by 2 orders of magnitude. Higher amount of acid results in the increasing of the current density. From the figure, it can be concluded that at 1 molar ratio of acid the porosity of the film has the minimum amount compared to other sols.

The effect of water-propanol ratio on the final structure of the sol solution was investigated by preparing sols containing different amount of water (Table 5.5).

Sol	GLYMO	AcOH	AcAc	Water	Propanol	Water-propanol molar ratios
E	1	1	2	4	1	4
F	1	1	2	3	2	1.5
G	1	1	2	1	1	1
H	1	1	2	2	3	0.67
I	1	1	2	1	4	0.25

Table 5.5: The molar ratio of different sols containing different amount of water

Figure 5.30 shows current density-potential plots for GLYMO-coated samples in 0.1 M acetate buffer.

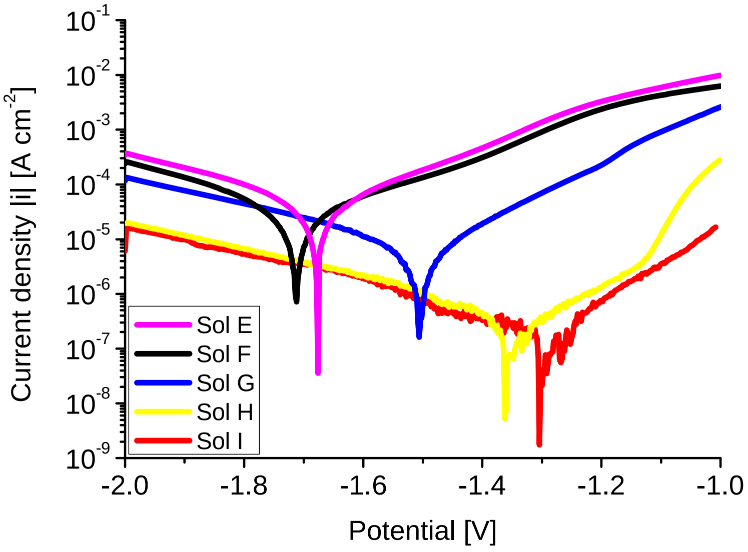

Figure 5.30: Effect of water-propanol molar ratio on the current density of GLYMO-coated samples in 0.1 M acetate buffer after heating for 1 hour at 573 K

Figure 5.31 also shows the current density at $E_{corr.}$ + 100 mV ($I_{diss.}$) of GLYMO-coated samples at different water molar ratio after heat treatment at 573 K for 1 hour.

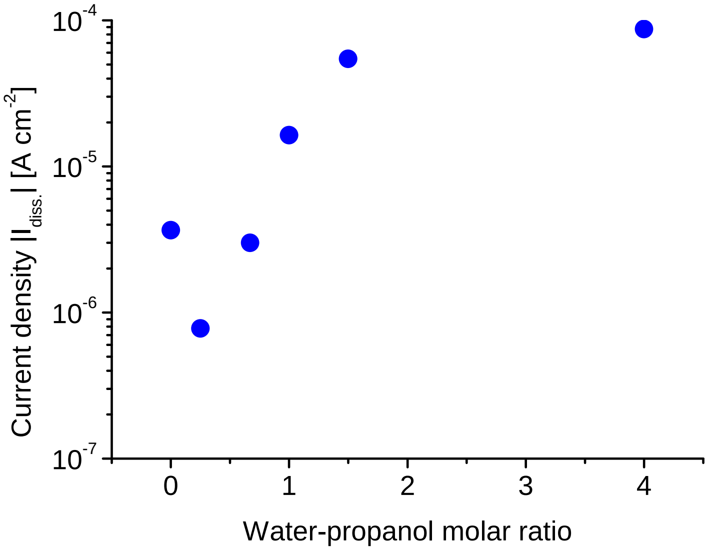

Figure 5.31: Current density of GLYMO-coated samples containing different water-propanol molar ratio in 0.1 M acetate buffer after heating for 1 hour at 573 K

As mentioned earlier, addition of higher amount of water leads to an increase of porosity due to the higher hydrolysis rate which results in the formation of a loose cross-linked coating and leads to the less protection performance. The solution containing 1:4 molar ratio of water-propanol provides the best protection with the lowest current density.

The effect of heating temperature on sol C coated samples is shown in Figure 5.32 at four different temperatures.

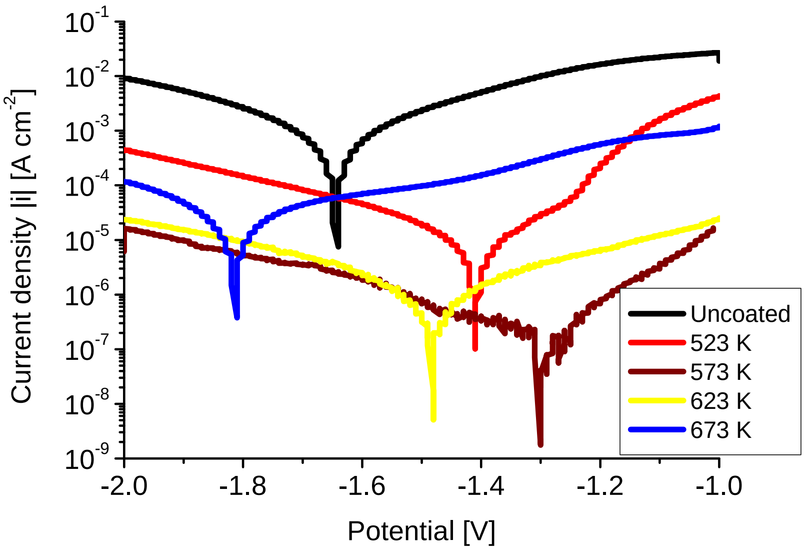

Figure 5.32: Effect of heating temperature on electrochemical corrosion protection performance of GLYMO-coated samples in 0.1 M acetate buffer

As shown, compared to the uncoated sample, increasing the heating temperature provide less porous film until 573 K. In our case obviously 573 K represents the optimum process temperature for good protection results. Beyond these temperature current densities of the coated samples increase again. This behavior can be related to the induced stress during the shrinkage of the coating at higher temperature which results in the formation of cracks in the coating.

Corrosion ability of the coating in 0.05 M sodium chloride solution is shown in Figure 5.33. As discussed earlier, solutions containing chloride ions represent a very aggressive environment for magnesium samples because they can accelerate its corrosion. The current density for coated magnesium sample is 2 orders of magnitude lower than that of the uncoated sample. This shows the improvement of the corrosion resistance by the sol-gel coating.

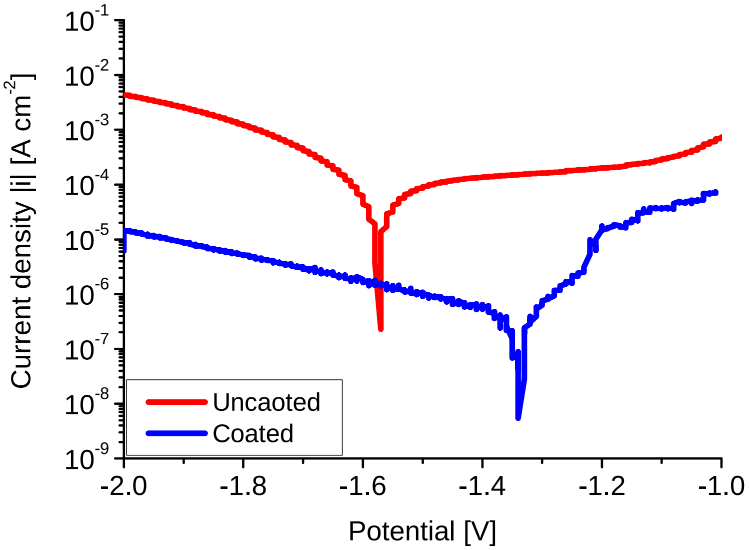

Figure 5.33: Electrochemical measurements of bare and GLYMO-coated magnesium sample in 0.05 M sodium chloride solution after 1 hour heat treatment at 573 K

Figure 5.34 shows the scanning electron microscope pictures of coated magnesium samples with GLYMO after the heat treatment for 1 hour at 573 K (left) and immersed for 15 minutes in chloride solution (right).

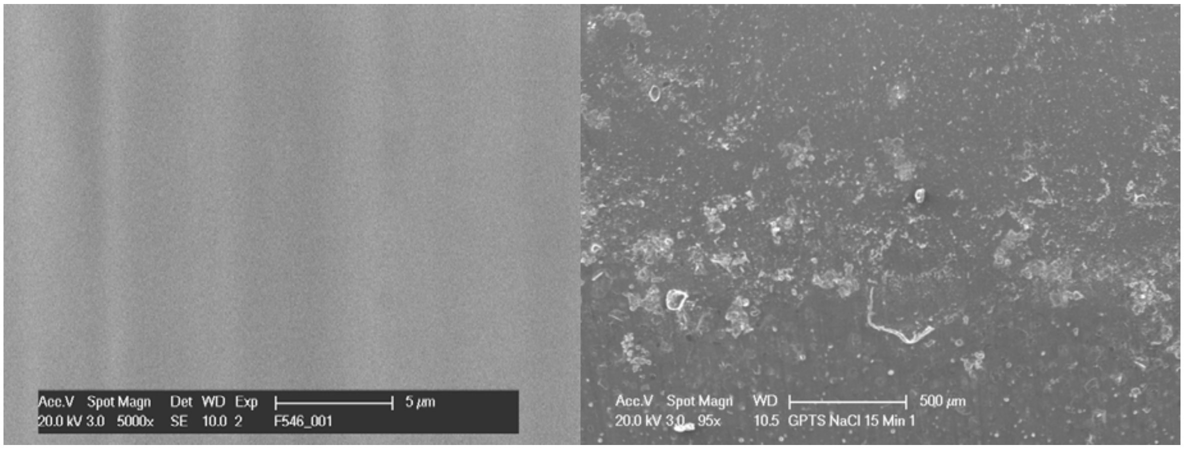

Figure 5.34: SEM pictures of GLYMO coated sample after heat treatment at 573 K for 1 hour (left) and exposed to chloride solution for 15 minutes (right)

Adhesion between the coating and the sample is good, but the coating is strongly attacked by the chloride solution (Figure 5.34 right). Nevertheless, the current density–potential plot showed a certain protection compared to the uncoated system.

5.3.2 Characterization of Sol-Gel Solution:

Figure 5.35 shows the IR spectra of Pure GLYMO and sol C after 1 hour reaction in acidic solution.

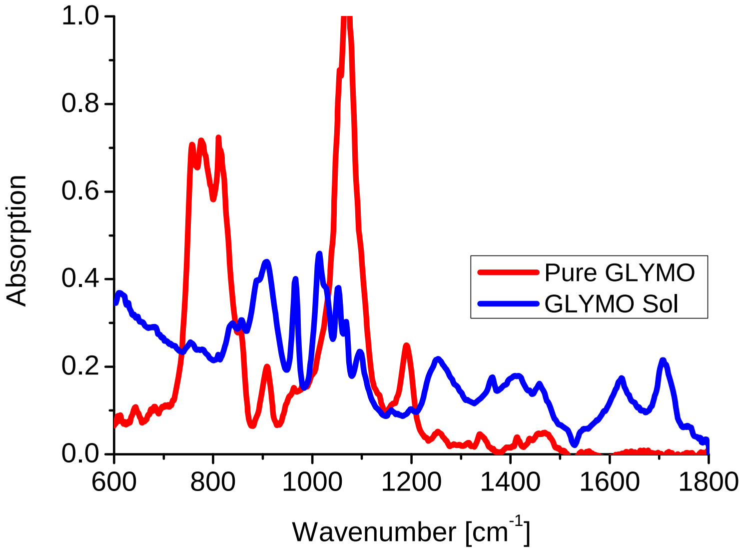

Figure 5.35: Infrared spectrum of Pure GLYMO and its sol after one hour reaction in acidic condition

The epoxy group in GLYMO has characteristic IR absorption bands at 1280-1260 cm^{-1}, 980-950 cm^{-1} and 865-785 cm^{-1} due to the C-H stretch in the epoxy group. [135] It is known that a decrease in the intensity of these bands can be attributed to the ring opening of epoxy group. [136-138] It is clear from the above figure that during the sol-gel process the intensities of these bands has been drastically decreased which proves the ring opening during the reaction. For pure GLYMO, the bands at 1410 cm^{-1}, 1075 cm^{-1} and 815 cm^{-1} corresponds to the C-H stretching vibration of CH_2 group, C-O stretching vibration of epoxy ring and Si-O stretching vibration respectively. As the reaction proceeds, the intensity of the Si-O band decreases which can be attributed to the Si-O-Si bond formation. During the reaction, a peak at 1050 cm^{-1} appears which can be assigned for Si-O-C formation. [139]

Figure 5.36 shows the IR spectra of dried gel heated at 573 K for one hour.

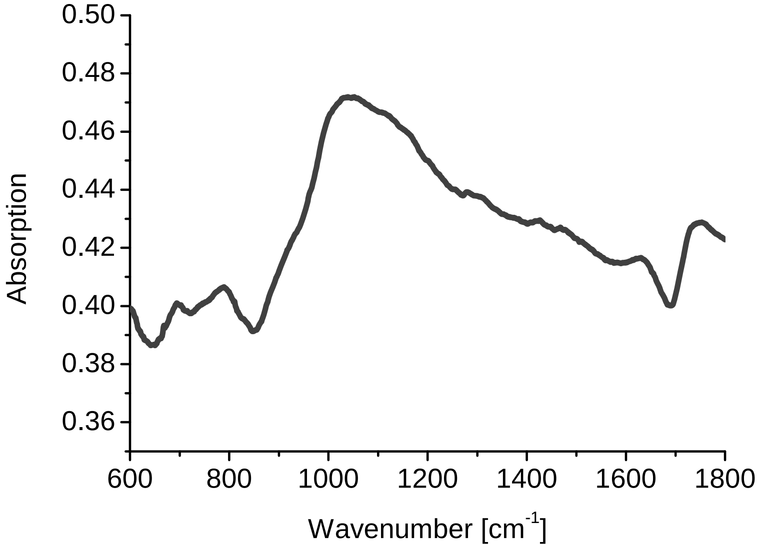

Figure 5.36: IR spectra of dried GLYMO gel heated at 573 K for one hour

The broad band at about 1100 cm^{-1} indicates that the gel body contains mostly Si-O-Si and Si-O-C skeleton.

Figure 5.37 shows the depth profile for the isotopes $^{24}Mg^{+}$, $^{25}Mg^{2+}$, $^{28}Si^{+}$, $^{30}Si^{+}$ and $^{16}O^{+}$ for the GLYMO-coated sample treated at 573 K. The absence of all intensities except oxygen at the beginning and the following sharp increase of all signals at around 150 s is due to the gold layer on top of the sample that was added before the measurement to reduce the charging effects (the gold signal was not recorded); There is, however, some charge remaining as is obvious from the small peaks exhibited by all signals after sputter removal of the gold layer (~200 s). The magnesium signal appears obviously at the surface of the film with intensity only slightly lower than in the bulk material. The silicon signal is constant for about 5000 s and decreases slowly; the actual transition might be sharper as the sample suffers from sputter induced roughening during depth profiling. The oxygen signal is nearly constant over the entire profile, but it has to be pointed out that this is a combination of the oxygen initially inside the sample and the oxygen implanted via the primary ions; the ^{18}O signal was recorded as well but yields too low intensities to be useful.

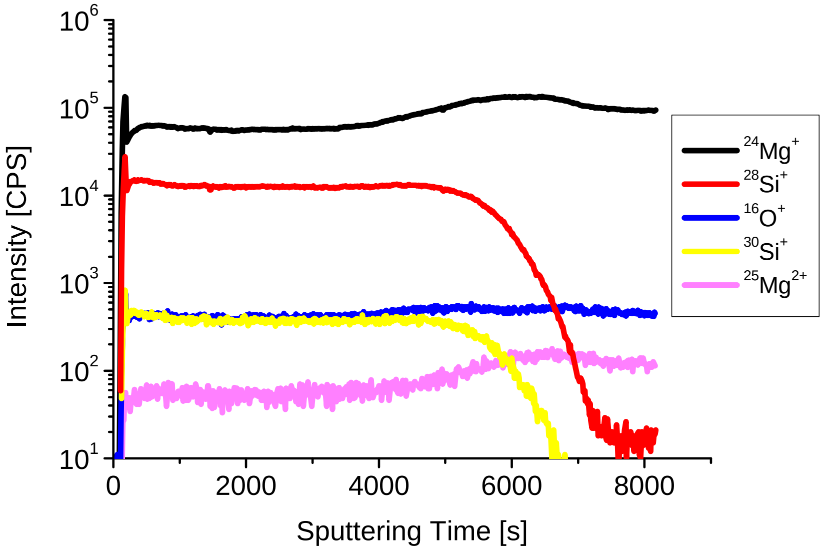

Figure 5.37: SIMS-depth profile of GLYMO-coated magnesium sample after heating at 573 K for 1 hour

Figure 5.38 shows X-ray diffractogram for a coated sample heat treated at 573 K. Reflections at 32°, 34°, 48° and 63° belong to magnesium. Additional reflections at 63.2° which can be assigned to magnesium silicate (with Miller index of (1012)) appearing after the heat treatment. The appearance of the $MgSiO_3$ phase in correlation with the SIMS results again proves a strong diffusion between magnesium and the coating material during the heat treatment resulting in the formation of a mixed oxide layer rather than a pure silicon oxide coating. This interdiffusion layer can act as a well adherent barrier to prevent the magnesium substrate corrosion by aqueous corrosive media.

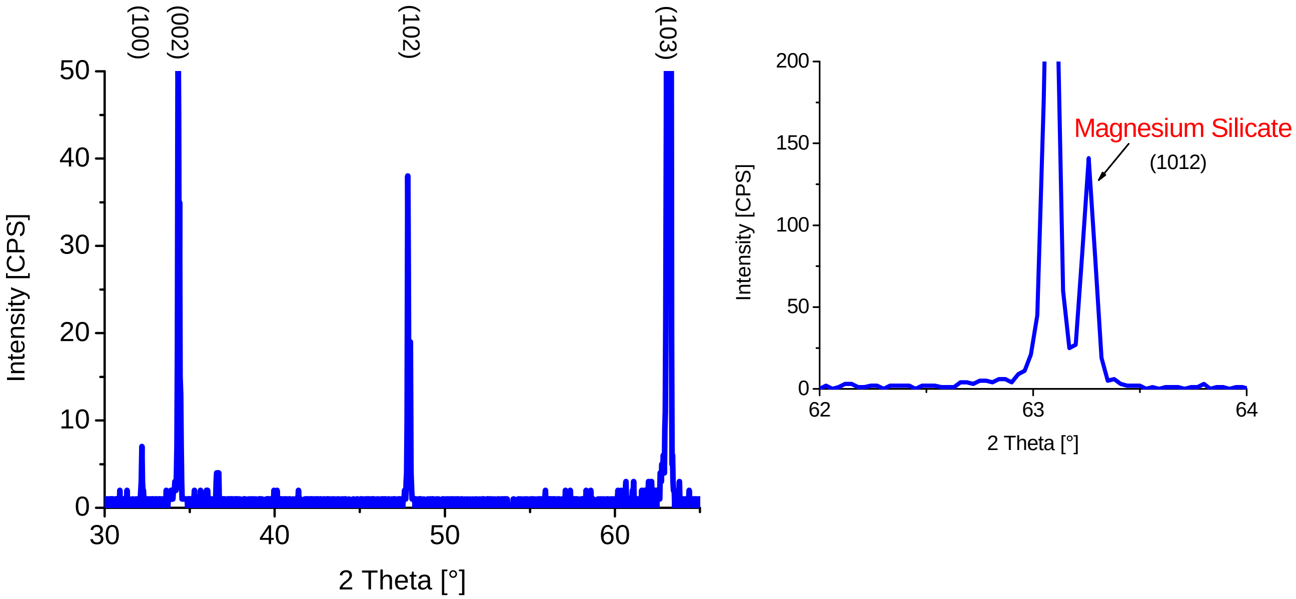

Figure 5.38: XRD analysis of a GLYMO-coated sample after heating at 573 K using 2 θ omega symmetric scan with enlarged area for magnesium silicate reflection

5.4 Vinyl-triethoxysilane (VTES):

For next step Vinyl-triethoxysilane was used as precursor. The organic function of this unsaturated polymer hydrolyzes readily in acetic acid solution to silane triols, and then condenses slowly to oligomeric siloxanols. A fresh aqueous solution of vinyl-triethoxysilane contained 82% monomer, 15% dimer and 3% trimer. [128]

$$RSi(OEt)_3 + 3\ H_2O \xrightarrow{fast} RSi(OH)_3 + 3\ C_2H_5OH \qquad R = (CH_2{=}CH\text{-})$$

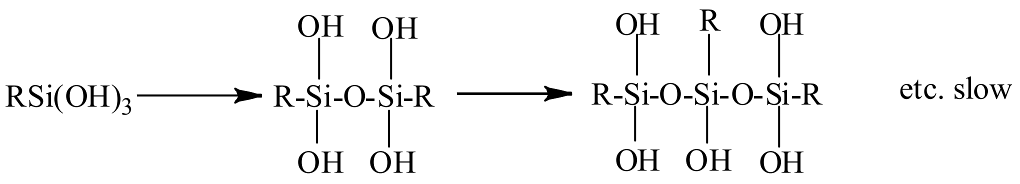

$$RSi(OH)_3 \longrightarrow R\text{-}\underset{OH}{\overset{OH}{Si}}\text{-}O\text{-}\underset{OH}{\overset{OH}{Si}}\text{-}R \longrightarrow R\text{-}\underset{OH}{\overset{OH}{Si}}\text{-}O\text{-}\underset{OH}{\overset{R}{Si}}\text{-}O\text{-}\underset{OH}{\overset{OH}{Si}}\text{-}R \quad \text{etc. slow}$$

5.4.1 Sol-Gel Solution Optimization:

The effect of stabilizing agent was investigated by preparing sol solutions with different molar ratio of acetylacetone (Table 5.6).

Sol	VTES	AcOH	Water	Propanol	AcAc
A	1	1.5	1	4	0.5
B	1	1.5	1	4	1
C	1	1.5	1	4	1.5
D	1	1.5	1	4	3

Table 5.6: The molar ratio of different sols containing different amount of stabilizing agent

Figure 5.39 shows the current density-potential plots of VTES-deposited samples with different acetylacetone molar ratios in 0.1 M acetate buffer after heating at 573 K for 1 hour. Addition of stabilizer to the sol solution reduces the current density by two order of magnitude compared to the uncoated sample.

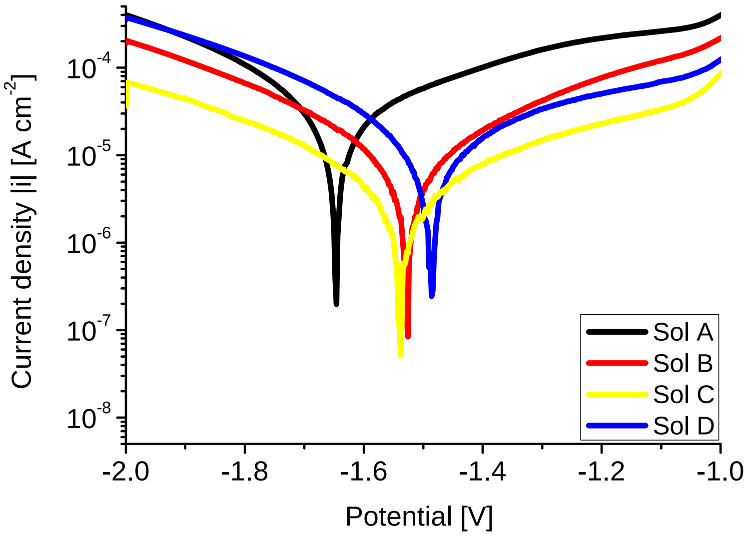

Figure 5.39: Current density-potential plots for VTES-coated samples containing different acetylacetone molar ratio in 0.1 M acetate buffer heat treated at 573 k for 1 hour

Current density ($I_{diss.}$) of VTES-coated samples at different acetylacetone ratios is shown in Figure 5.40.

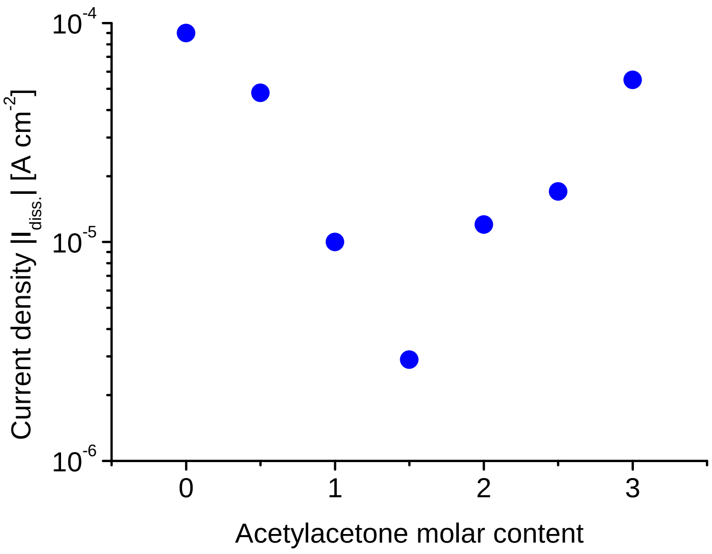

Figure 5.40: $I_{diss.}$-acetylacetone molar ratio of VTES-coated samples heat treated at 573 k for 1 hour

From the current density values, Sol C was selected for further investigation. The effect of heating temperature on the porosity for deposited samples from sol C is shown in Figure 5.41. Temperatures of 523 and 573 K provide almost the same porosity.

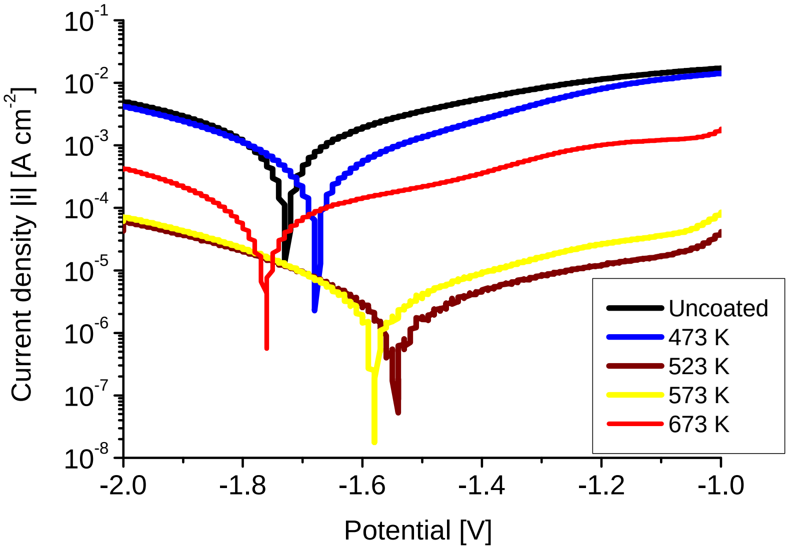

Figure 5.41: Effect of heating temperature on corrosion protection performance of VTES-coated sample in 0.1 M acetate buffer

In order to keep annealing temperature at lower amount and from economical and experimental point of view, 523 K was selected as an optimum temperature for further experiments. With the current density value of $I_{diss.}$ for uncoated magnesium sample as a reference for 100% porosity, the average porosity of the sample annealed at 523 K can be reduced to 2%. Decreasing the amount of porosity can be related to the precursor.

Ability of this system in more aggressive corrosive medium was investigated by depositing of a film prepared at optimized sol solution conditions. Figure 5.42 shows the current density-potential curves of bare and VTES-coated magnesium samples immersed in 0.05 M sodium chloride solution.

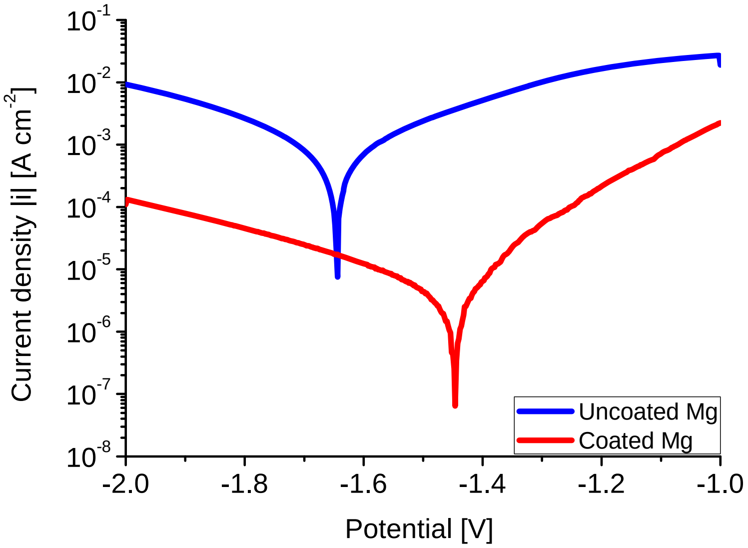

Figure 5.42: Current density-potential plots of bare and VTES-coated magnesium sample in 0.05 M sodium chloride solution after 1 hour heat treatment at 523 K

As can be seen, VTES deposited film is able to enhance the corrosion resistance of magnesium in aggressive environment by 2 orders of magnitude.

5.4.2 Structural Characterization of Deposited Film:

Figure 5.43 shows the IR spectra of pure VTES, sol solution containing VTES as precursor and dried gel after one hour heat treatment at 573 K.

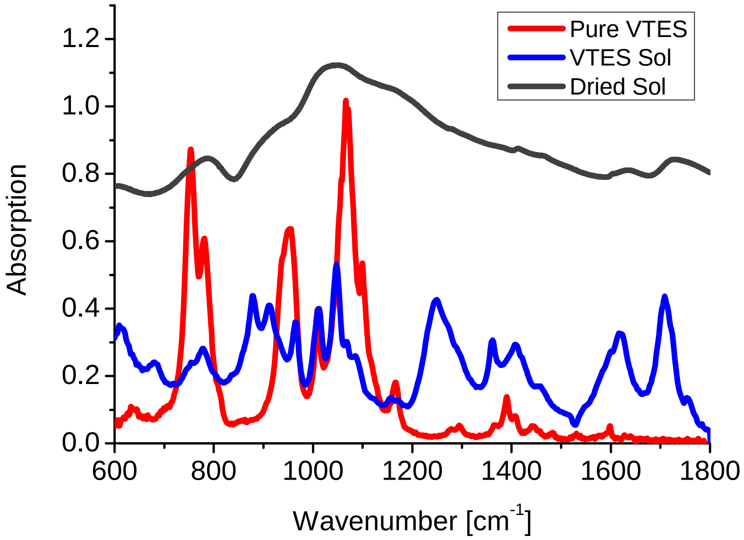

Figure 5.43: Infrared spectra of pure, Sol C and dried VTES

Table 5.7 summarizes the observed IR spectroscopic frequencies along with their vibrational assignment for pure VTES.[140-141] Following the intensity of the very strong band at 1050 cm^{-1} which has been assigned for Si-O bond can be applied for any change during the sol-gel process and heat treatment. [142] As the sol reaction proceeds, the intensity of this band decreases which can be attributed to the asymmetric stretch of Si-O-Si bond. [143-144] Furthermore, the sharp and strong band at about 964 cm^{-1} is assigned to the vibration of Si-O in silanol. As the condensation reaction proceeds, its intensity decreases. In the case of dried gel, the absence of IR band about 1450 cm^{-1} due to the CH_3 deformation of ethoxy group indicates the complete hydrolysis of VTES in sol-gel process. On the other hand, formation of Si-O-Si skeleton can be also recognized by the presence of very strong and broad band at about 1050 cm^{-1}.

IR [cm^{-1}]	Vibrational Assignment
1599 (w)	vinyl C stretch
1483 (vw)	CH_3 asymmetric def.
1443 (w)	CH_3 asymmetric def.
1407 (m sh)	vinyl CH_2 in-plane def.
1392 (m)	CH_3 symmetric def.
1296 (w)	ethoxy CH_2 twist
1168 (ms)	C-C stretch
1050 (vs)	Si-O stretch
962 (s)	vinyl CH_2 wag
785 (s)	Si-C stretch
761 (s)	Si-C stretch
640 (w)	Vinyl CH bend
s=strong, m=mediate, w=weak, v=very, sh=shoulder	

Table 5.7: Observed vibrational frequencies (cm^{-1}) of vinyl-triethoxysilane

Figure 5.44 shows a depth profile of the deposited film annealed at 523 K. Sputtering from the surface downward to the metal substrate, Mg can be detected already at the surface with high intensity throughout the coating, i.e. the final coating does not only consists of Si and O but also of Mg. The appearing of the magnesium signal from the very beginning of SIMS measurements again proves a strong interdiffusion effect between the substrate and deposited thin film. There is a gradual change of the intensities within the layer, with the Si signal slowly decreasing with sputtering time whereas the Mg intensity stays high. After about 1200 s the layer ends with the Si intensity dropping. Both signals are also affected by the amount of oxygen, e.g. the magnesium signal is higher in the layer than in the substrate region, with a peak in the interface region. The effect on the $^{25}Mg^{2+}$ signal, however, is considerably lower, thus it is more likely to represent the concentration. The oxygen in the substrate is mainly due to the use of oxygen primary ions. Variation of the temperature does not significantly change either the film thickness or the ratio of the Mg and Si intensities.

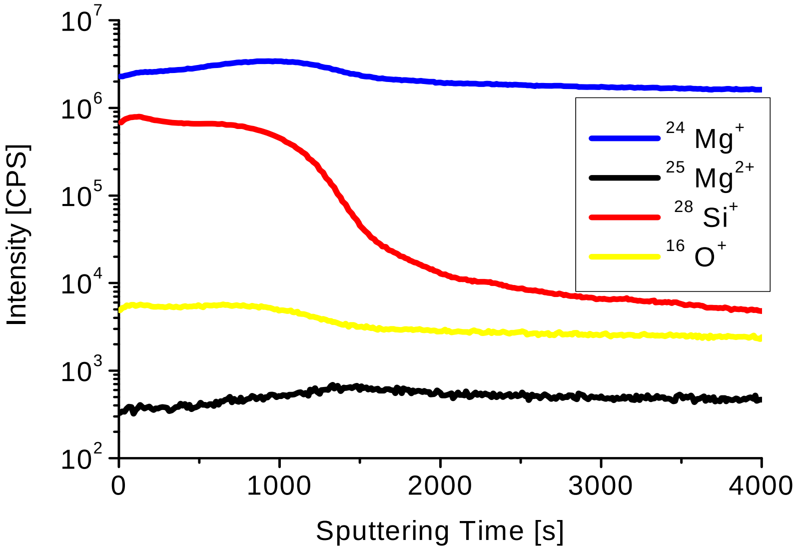

Figure 5.44: SIMS-elemental profile of a VTES-coated magnesium sample after heating at 523 K for 1 hour

In order to prove the presence of inter-diffusion layer, X-ray diffraction analysis was applied to the coated sample for phase analysis. Figure 5.45 shows the diffraction pattern for the deposited sample treated at 523 K using a fixed angle of incidence of 3°. Beside the reflections of the magnesium phase at 32.2° Mg (001), 34.4 Mg (002), and 36.6° Mg (101) an additional reflection at 35.1° (204) appears after the heat treatment which can be related to the tetragonal magnesium silicate phase ($MgSiO_3$). The appearance of this phase supports the SIMS results.

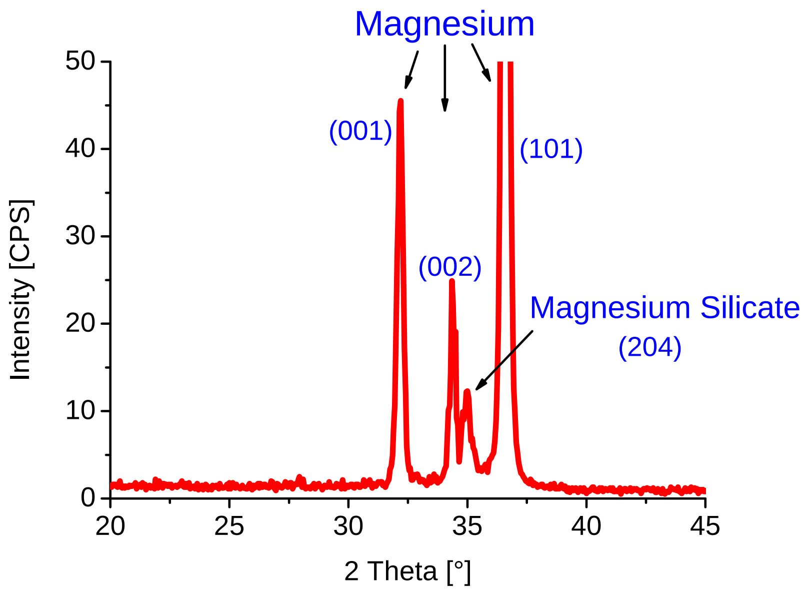

Figure 5.45: X-Ray diffractogram of VTES-coated sample after heating at 523 K using a fixed angle of incidence of 3°

5.4.3 Further Electrochemical Characterization:

Figure 5.46 shows the open circuit potential (OCP) curves for 5 hours immersion time for uncoated and coated magnesium samples in acetate buffer. It can be seen that the OCP of the coated magnesium samples is more positive than of the uncoated substrates which indicate protection ability of the coating.

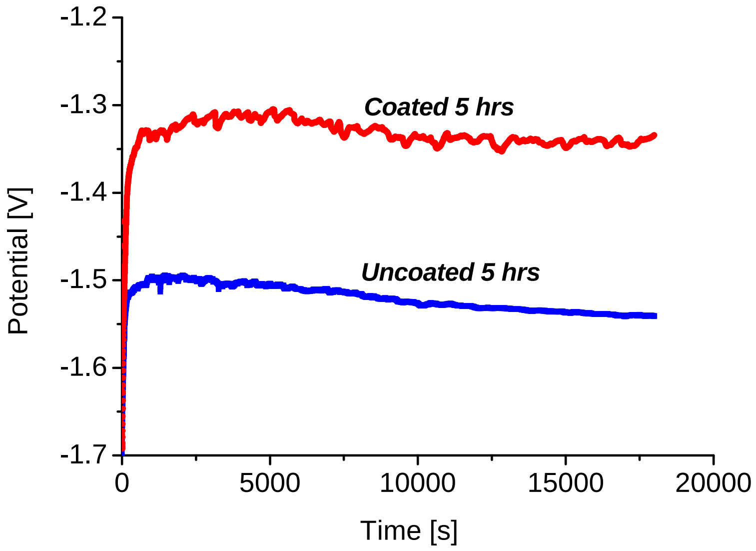

Figure 5.46: Open circuit potential vs. time measurements for an uncoated and VTES-coated magnesium samples immersed in 0.1 M acetate buffer

Figure 5.47 shows the impedance diagrams of pure Magnesium samples at E_{OCP} for different immersion times.

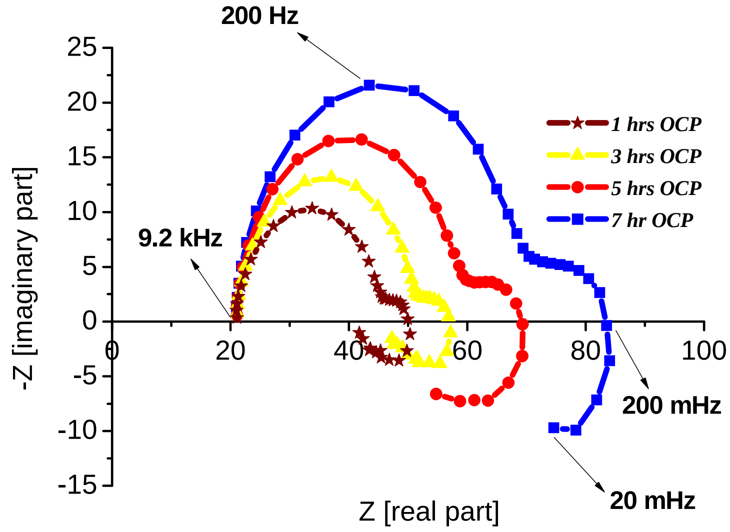

Figure 5.47: Electrochemical impedance diagrams of bare magnesium samples measured after different immersion time in a 0.1 M acetate buffer

All these diagrams are characterized by two well-defined capacitive loops, at high and medium frequencies, followed by an inductive loop at lower frequency domain as mentioned by other authors. [145-146] The high frequency loop appears to be the result of charge transfer and the effect of the natural oxide film because the value of capacitance associated with this loop is low (15-30 μF cm^2) compared to the usual value of double layer capacitance (around 50 μF cm^2). From the capacitance, the thickness of this protective film can be evaluated from:

$$d = \frac{\varepsilon \varepsilon_0 S}{C}$$

where ε_0 is the vacuum permittivity (= 8.85 * 10^{-14} F/cm), ε is the magnesium oxide relative dielectric constant (= 10) and S is the exposed surface area (2 cm^2). The amount of about 1 nm was obtained for the film. The medium frequency capacitive loop can be attributed to the relaxation of mass transport in the solid phase. The characteristic frequency of inductive loop decreases with increasing immersion time and has been attributed to the existence of relaxation processes of adsorbed species. [147] The increase in immersion time at E_{OCP} leads to a size increase in both high and medium frequency capacitive loops and inductive loop.

Detailed interpretation of EIS spectra was performed by numerical fitting of Nyquist plots using the equivalent circuit shown in Figure 5.48.

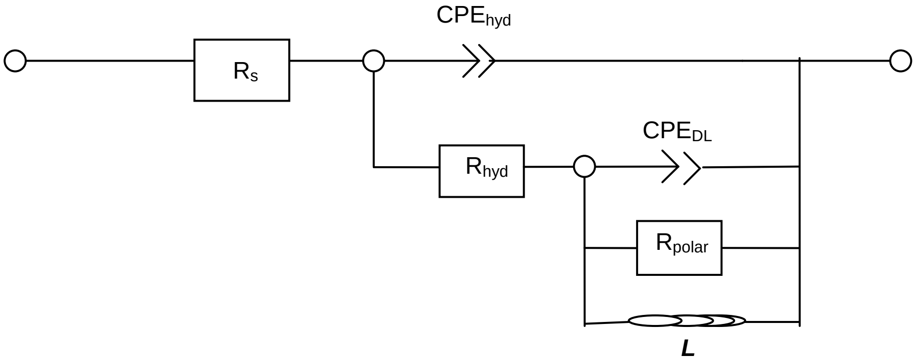

Figure 5.48: Schematic representation of the interface and the equivalent circuit for pure magnesium sample

R_s corresponds to the resistance of electrolyte which has the constant amount of 30 Ω. This circuit is composed of two time constants: the hydroxide resistance R_{hyd} and constant phase element CPE_{hyd} (corresponding to capacitance C_{hyd}) and the polarization resistance R_{polar} and double layer capacitance C_{DL} represented by CPE_{DL}. All the capacitances shown in the equivalent circuits are mathematically modeled using a constant phase element in order to consider the electrochemical behavior of systems which do not correspond exactly to a pure capacitance. The values of C_{hyd} and C_{DL} were calculated by:

$$C = Q(\omega_{\max})^{N-1}$$

where $\omega_{\max}$ is the frequency at which the imaginary impedance reaches a maximum for the respective time constant and Q and N are the component of CPE. [148]

Table 5.8 shows the results of corresponding elements of the equivalent circuit. R_{hyd} increases whereas C_{hyd} decreases with immersion time which can be attributed to the formation of a passive film of corrosion products (mainly hydroxides) on the metal surface. All the impedance spectra show an inductive loop at low frequency which was almost independent of the immersion time. The presence of the inductive loop in the low frequency range involves an adsorbed species. Mg^+ is the simpler species which can be involved in the Mg corrosion as an intermediate.

Time	C_{hyd} F.cm^2	R_{hyd} ohm	C_{DL} F.cm^2	R_{polar} ohm	L H
1	$31.7*10^{-6}$	21.89	0.033	9.541	13.29
3	$21.4*10^{-6}$	27.53	0.028	10.13	16.94
5	$20.9*10^{-6}$	33.28	0.027	23.54	28.34
7	$15.1*10^{-6}$	45.97	0.017	23.32	31.9

Table 5.8: Electrochemical impedance spectroscopy simulation results of pure magnesium immersed in 0.1 M acetate buffer

Figure 5.49 shows the EIS results of VTES-coated magnesium samples after 1 and 5 hour immersion times. Most coatings degrade with time, resulting in a more complex behavior. However, it is sometimes not easy to select the appropriate equivalent circuit to use in the fitting process. [149-150] After a certain amount of time, electrolyte penetrates into the coating and forms a new liquid/metal interface under the coating and corrosion phenomena can occur at this new interface.

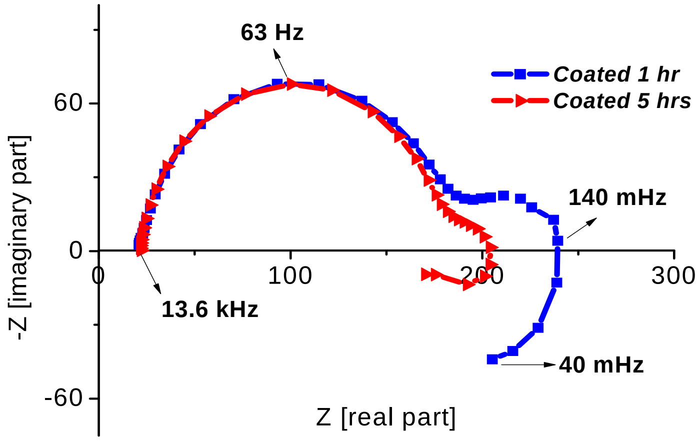

Figure 5.49: Electrochemical impedance diagrams of VTES-coated magnesium samples after 1 and 5 hours immersion in 0.1 M acetate buffer

The impedance spectra were fitted by two time constants equivalent circuit, shown in Figure 5.50.

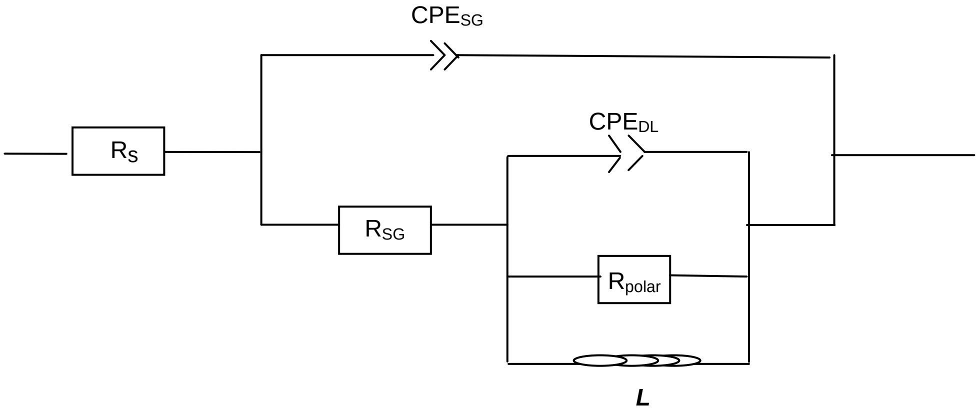

Figure 5.50: Schematic representation of the interface and the equivalent circuit for VTES-coated magnesium samples

Parallel equivalent circuit components were considered to represent the sol-gel coating parameters, R_{SG} and C_{SG} (represented by CPE_{SG}). There was a little change in the coating capacitance C_{SG} which is probably caused by swelling or increase in coating thickness associated with coating relaxation. The fitted values and calculated capacitances using the equivalent circuit shown in Figure 5.50 are summarized in Table 5.9. The coating resistance R_{SG} decreases with time because many coatings are permeable to electrolytes to some extent.

Time	C_{SG} F.cm^2	R_{SG} ohm	C_{DL} F.cm^2	R_{polar} ohm	L H
1	$26.3*10^{-6}$	164.2	$29.5*10^{-6}$	83.03	385.7
5	$18*10^{-6}$	112.5	$6.4*10^{-3}$	39.13	42.67

Table 5.9: Electrochemical impedance spectroscopy simulation results of VTES-coated magnesium samples heat treated at 573 K for 1 hour immersed in 0.1 M acetate buffer

Comparing the R_{SG} of coated sample with R_{hyd} of uncoated sample shows the ability of our system to increase the resistance of the magnesium sample. From the results, it can be concluded that the film is applicable to increase the corrosion resistance of the sample until 10 hours of immersion. For longer immersion time and due to the insufficient protective film on magnesium, the corrosion process will start which can be characterized by drop of R_{SG} amount.

Figure 5.51 shows the SEM picture of coated magnesium sample before and after immersion in acetate buffer for 1 hour.

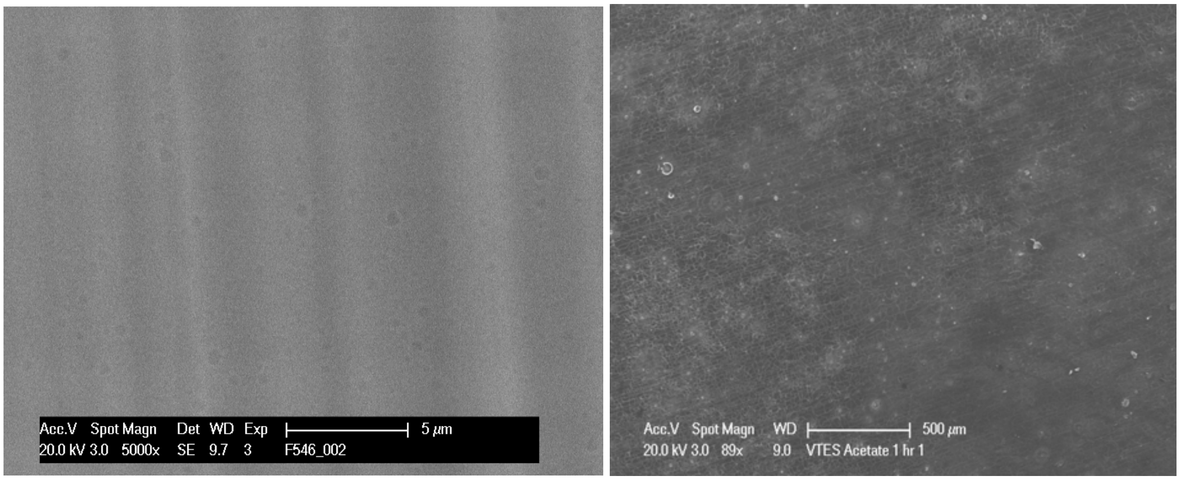

Figure 5.51: SEM picture of VTES-coated magnesium sample before (left) and after immersion (right) in 0.1 M acetate buffer for 1 hours

As can be seen, the coating is completely homogenous and able to cover the roughness of the magnesium samples. After 1 hour, there is a partial solubility of the coating which results in the decreasing of the resistance but is still able to provide some protection as proved by the EIS results.

5.5 SiO_2-ZrO_2 Mixed Oxide:

As shown earlier, thermal mismatch between magnesium and zirconia at relatively high temperature (573 K) caused bad adhesion between the coating and magnesium substrate. Therefore, zirconia was unable to provide any protection on substrate against corrosion. For next step, a mixed sol solution containing silane coupling agent and zirconium (PTES-Zr, VTES-Zr and GLYMO-Zr) was deposited on magnesium samples and ability of silicon to improve the adhesion of zirconia onto the substrate in low temperature range was investigated.

5.5.1 Characterization of Sol Solution:

The effect of heating temperature was firstly investigated on the final structure of the resulting film and the best result obtained at 393 K. Figure 5.52 shows the IR spectra of pure GLYMO, GLYMO with zirconium and the solid body of the mixed gel treated at 393 K for 120 minutes. As explained for GLYMO section previously, the bands at 1050 cm^{-1} and 815 cm^{-1} can be assigned to the Si-O stretching vibration and Si-O symmetric bond stretching. Any decrease of these bands during the sol-gel reaction can be used as identification for the hydrolysis and condensation reactions which result in the formation of Si-O-Si bonds. It has been documented that the Si-O-Si stretching band near 1100 cm^{-1} will shift towards lower values when Zr atoms replace the Si atoms to form Zr-O-Si hetero-linkages. [151-152] Appearance of a band at 950 cm^{-1} has been assigned for Zr-O-Si linkage during the sol-gel reaction. [153-154] In the case of dried gel, the presence of bands at 1050 cm^{-1} and 950 cm^{-1} after heat treatment also indicated that the gel body contains both Si-O-Zr and Si-O-Si skeletons. The same behavior was observed for PTES-Zr and VTES-Zr mixed solutions.

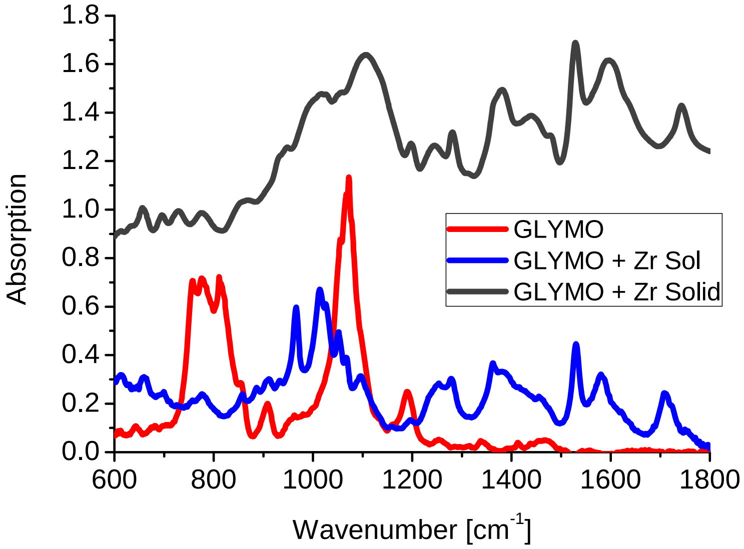

Figure 5.52: Infrared spectra of GLYMO, GLYMO containing Zr in the 1:1 molar ratio and dried gel treated at 393 K

Figures 5.53 and 5.54 show the SIMS depth profile of magnesium samples coated with mixed oxide layers heat treated at 393 K.

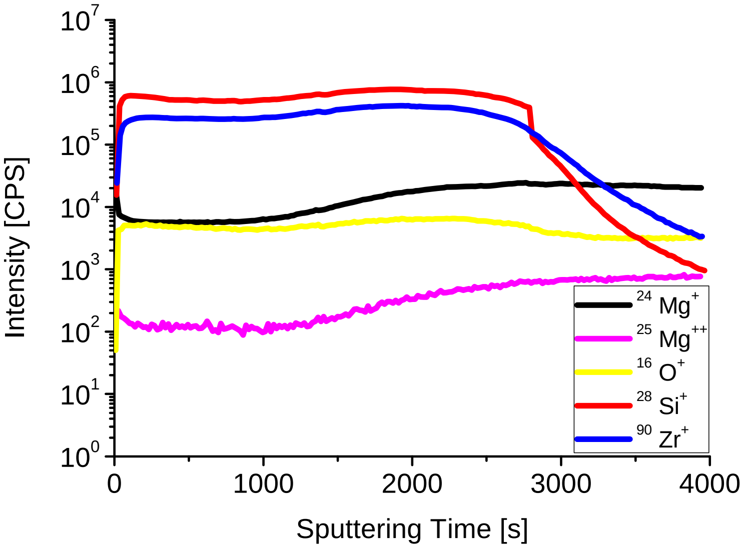

Figure 5.53: SIMS depth profile of magnesium sample coated with GLYMO-Zr mixed oxide layer heat treated at 393 K for 2 hour

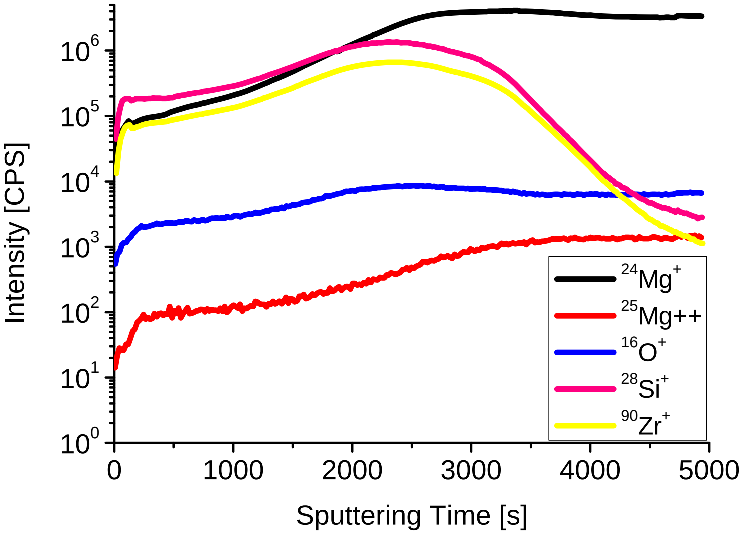

Figure 5.54: SIMS depth profile of magnesium sample coated with VTES-Zr mixed oxide layer heat treated at 393 K for 2 hour

The SIMS profile shows similar intensities for the zirconium and the silicon signal from the surface of the coated sample down to the substrate. This indicates the presence of a mixed-oxide layer.

Figures 5.55 and 5.56 show the XRD diffractograms of magnesium samples coated with mixed GLYMO-Zr oxide layers heat treated at two different temperatures. Despite of the IR and SIMS results, XRD pattern showed no characterized reflection for a Zr-O-Si, ZrO_x or SiO_x structure and only magnesium reflections could be recognized. The absence of XRD reflectiuons suggest that the phase formed is nanocrystalline or quasi-amorphous. The four-element system, containing of two metals and two non-metals seems to remain in an unordered state at the given comparatively low temperature. Further experiments have to be applied to establish a good view about the nature of the film.

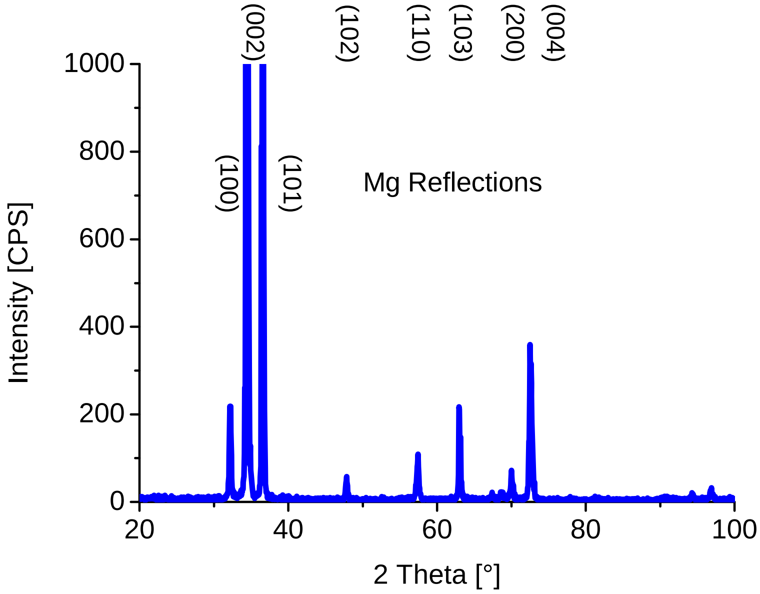

Figure 5.55: XRD diffractogram of mixed Zr-Si oxide layer coated on magnesium heat treated at 393 K for 2 hours

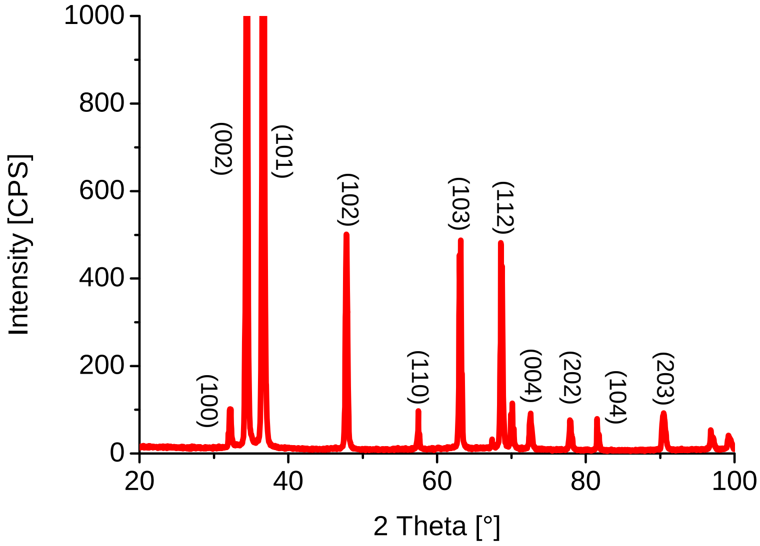

Figure 5.56: XRD diffractogram of mixed Zr-Si oxide layer coated on magnesium heat treated at 473 K for 2 hours

Transmission electron microscopy was used to provide more information about the amorphous nature of the films. The sols were prepared at the same condition as thin film deposition and heat treated at 393 K for 2 hours. The obtained thin flakes were dispersed in ethanol, deposited on a copper grid and examined by TEM method using a 100 kV electron beam. Figure 5.57 shows the digital images of mixed GLYMO + Zr sol treated at 393 K.

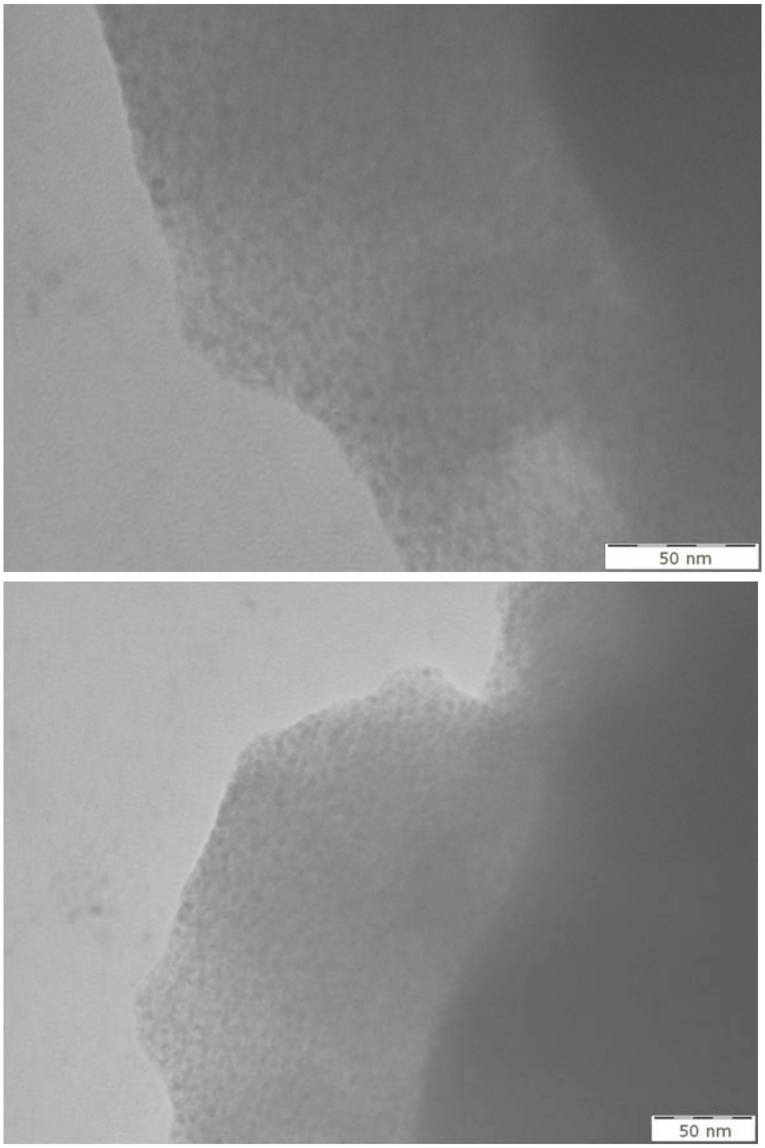

Figure 5.57: TEM pictures of GLYMO + Zr sol treated at 393 K for 2 hours

These pictures clearly show the absence of any crystalline phase; the structures are featureless. Electron diffraction did not give any reflexes which also prove the absence of crystalline structures.

5.5.2 Electrochemical measurements:

Figure 5.58 shows the result of current density-potential measurements of magnesium samples coated with mixed oxide solutions after heat treatment at 393 K for one hour.

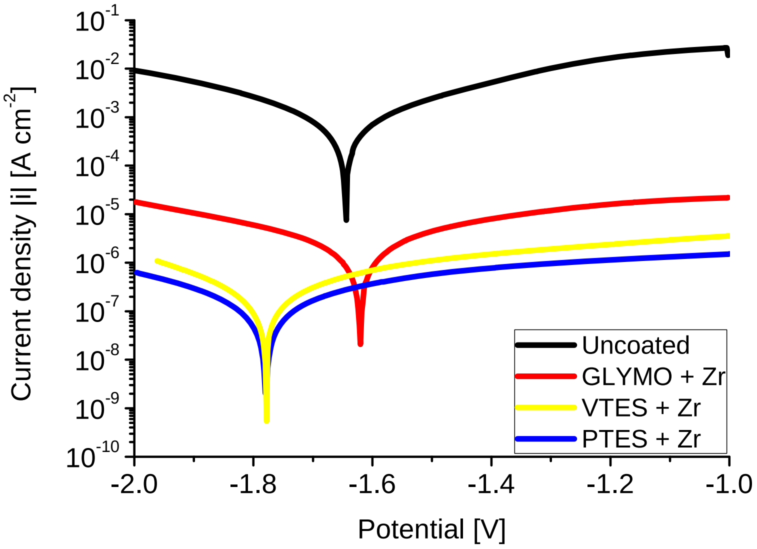

Figure 5.58: Current density-potential curve of magnesium samples coated with mixed Si/Zr oxide layer in 0.1 M acetate buffer treated at 393 K for 2 hour

As can be seen, the deposited film is able to improve the resistance of the magnesium by 3 orders of magnitude. On the other hand, very low heat treatment is necessary compared to the normal sol-gel process which can make it suitable film for heat-sensitive applications. This improvement can be related to two factors. Firstly the hetero-linkages of Zr-O-Si which leads to well adherent and dense coating film and secondly to the amorphous nature of mixed oxide deposited films. It is well-.known that the grain boundaries of crystalline materials can act as the starting site for corrosion and accelerate the corrosion process. The absences of these sites for amorphous materials result in the enhancement of the material against corrosion.

Figure 5.59 shows the impedance diagram of magnesium sample coated with Si(GLYMO)-Zr oxide layer after 1 and 10 hours immersion in 0.1 M acetate buffer.

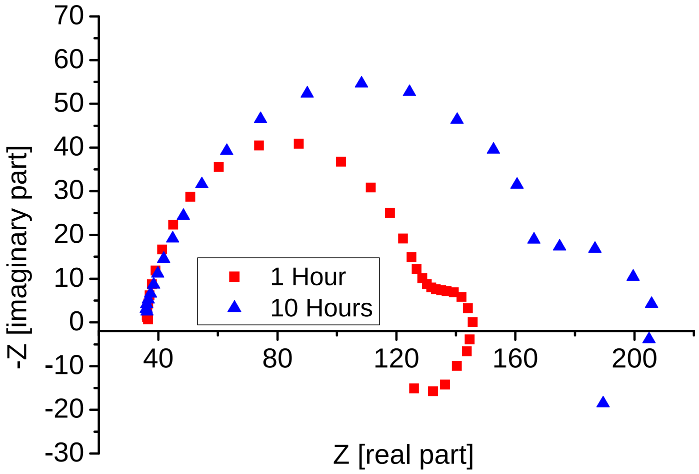

Figure 5.59: Electrochemical impedance diagrams of ucoated magnesium samples plotted after 1 and 5 and 10 hours immersion time in a 0.1 M acetate buffer

As explained earlier, all these diagrams can be characterized by two high and medium frequency capacitive loops followed by a low frequency inductive loop. Same circuit as Figure 5.50 was used to fit the experimental data and the results are shown in Table 5.10.

Time	C_{SG} F.cm^2	R_{SG} ohm	C_{DL} F.cm^2	R_{polar} ohm	L H
1	27.1*10^{-6}	81.29	13*10^{-6}	35.95	190.2
10	31.9*10^{-6}	139.5	5.04*10^{-3}	28.59	135.6

Table 5.10: Electrochemical impedance spectroscopy simulation results of silica base coated magnesium samples in 0.1 M acetate buffer

Increasing the resistance of R_{SG} compared to uncoated sample R_{hyd} can be attributed to the coated Si-Zr film which creates a protective barrier by reducing the conductive pathways between the electrolyte and substrate. The lowest frequency processes observed for the coated samples are likely to be associated with the development of corrosion activity and growth of porous corrosion products. The decrease in C_{DL} and an increase in R_{Polar} compared to the uncoated substrate indicate that the coated films are more protective then the natural films on magnesium.

5.6 Overview of Tafel Experiments:

Table 5.11 shows the Tafel experiment results of investigated systems for 1 hour immersion in 0.1 M acetate buffer pH = 5.5. From the Tafel Plot, corrosion potential, corrosion current and the Tafel slopes can be extracted. For a given Magnesium density, the rate of uniform corrosion (in mm per year) is then calculated.

Sol Solution	$E_{Corr.}$ (V)	$I_{Corr.}$ (μA)	β_a (mV)	β_c (mV)	Corrosion Rate (mmpy)
Uncoated	-1.7	723	294	305	16.5
GLYMO	-1.5	626	166	270	6.8
TPES	-1.7	465	301	258	5
VTES	-1.5	1.77	148	261	0.02
GLYMO + Zr	-1.4	0.2	272	263	$2.46*10^{-3}$
VTES + Zr	-1.2	0.12	324	314	$1.36*10^{-3}$
PTES + Zr	-1.2	0.06	279	347	$6.4*10^{-4}$

Table 5.11: Corrosion rate of magnesium samples coated with different sol-gels immersed in acetate buffer for 1 hour

As can be seen, some systems are capable of decreasing corrosion rate of magnesium by several orders of magnitude. It can be concluded that the porosity and corrosion resistance of the final film is defined by several parameters. Beside of the film porosity, its adhesion to the substrate considerably affects the ability of the film for protection purposes. In the case of porosity, optimization of constituents' concentration in sol solution resulted in the formation of less porous films which in turn could increase the corrosion resistance of the magnesium. As can be seen, the organofunctional group of the precursor plays an important role. It can be said that precursors with unsaturated organic groups lead to less porous films. Also the bulkiness of these groups affect the porous nature of final film. In the case of GLYMO, the presence of epoxy group which opens during the hydrolysis reaction leads to the formation of interconnected network with less porosity. This is shown by the current density-potential measurements where the currents are reduced up to two orders of magnitude. However, the Tafel experiments after 1 hour immersion show only a reduction in the corrosion rate down to 40 %. This discrepancy must again be explained by local adhesive failure. The unsaturated phenyl group in the PTES results in the formation of less porous film which slightly enhances the corrosion resistance of magnesium but again due to the loose adhesion between the resulting film and the substrate and the bulkiness of the phenyl group no good protection can be obtained. In VTES, the presence of unsaturated alyl group with much less bulkiness compared to the PTES and good adhesion of the film to substrate result to the formation of film with much less porosity and good protection ability. Both current density-potential measurements and Tafel experiment give a reduction by 2 or 3 orders of magnitude.

The best results were obtained from mixed oxide layer in which the adhesion problem of zirconia to the substrate can be overcome by addition of silicon to the sol solution. This reduction can be attributed to both less porous nature of the film and good adhesion of the resulting film to the substrate. Since the coating did not show any reflection in XRD and TEM, it is not composed of crystallines. It is well-known that corrosion may proceed along grain boundaries. Open grain boundaries act as pores and promote corrosion. The absence of grain boundaries may be the explanation for the observed superior behavior.

Summarily, all silane coupling agents can enhance the resistance of magnesium to some extent by providing a barrier layer on magnesium. The adhesion problem of zirconium to the substrate could be solved by applying mixed silicon-zirconium oxide layer. This layer acts as a good barrier against electrolyte and is able to dramatically enhance the corrosion resistance of magnesium.

6. Summary and Conclusion

The purpose of this work was to investigate the effect of experimental parameters of film formation on the porosity of oxide coatings, obtained by the sol-gel method, on magnesium. For the best films, their ability to enhance the corrosion resistance of magnesium in aggressive chloride was also investigated. Oxide layers of zirconium and silicon and mixtures of them were deposited on magnesium samples by spin coating method, followed by moderate heat treatment in an oven. The porous nature of sol-gel oxide layers has a main effect on the corrosion of the substrate because it provides direct paths between the substrate and an aggressive environment which leads to an increase of the substrate's corrosion. Several parameters such as the type of sol-gel precursor, amount of the catalyst, amount of stabilizer, amount of water, and heating temperature were investigated to provide films with lower porosity. Electrochemical techniques such as dynamic polarization scans, Tafel measurements and electrochemical impedance spectroscopy (EIS) were applied to investigate the porosity of the film and hence its ability to suppress corrosion. Several methods such as secondary ion mass spectrometry (SIMS), X-ray diffraction analysis (XRD), infrared spectroscopy (IR), optical microscopy and scanning electron microscopy (SEM) were applied to characterize the films.

It was shown that layers of zirconium oxide were unable to increase the corrosion resistance of magnesium. This problem can be explained by poor adhesion arising from the thermal mismatch between magnesium ($26.1 \times 10^{-6}\ K^{-1}$) and zirconium oxide ($5.6 \times 10^{-6}\ K^{-1}$). Shrinkage of the film during the heat treatment process results in stress between the substrate and film which consequently leads to delamination of the film under corrosive attack. SIMS results proved the highly incomplete coverage of the sample by the zirconia layer.

In order to promote the adhesion between the substrate and the film and hence increase the corrosion resistance of magnesium, silane coupling agents were next used as precursor for the sol-gel process. It was shown that films formed with these agents show a lower amount of porosity, combined with reasonable adhesion, and can therefore increase the corrosion resistance of magnesium. Therefore several of these precursors with different organic functionality were used to deposit silicon oxide films on magnesium and their effects on porosity and corrosion resistance were investigated.

First, phenyl-triethoxsilane was used as precursor for film formation on magnesium samples. Electrochemical results showed that this film is able to increase the corrosion resistance of magnesium in aggressive environments by 2 orders of magnitude. As a measure for corrosion susceptibility, the anodic dissolution current at a given potential was used. SIMS and XRD results showed the presence of an inter-diffusion layer (magnesium silicate) after the heat treatment step which acts as a barrier to prevent electrolyte diffusion into the coating and enhance the corrosion resistance of the substrate.

A sol solution containing 3-Glycidyloxypropyltrimethoxysilane (GLYMO) was also deposited on magnesium samples. Again, the SIMS results showed the presence of an inter-diffusion layer on magnesium after heat treatment. IR spectroscopy proved the presence of both Si-O-Si and Si-O-C bonds. The electrochemical measurements showed that the coating is able to reduce the magnesium corrosion in highly aggressive chloride solution by 2 orders of magnitude. Taking the porosity of bare material as 100 %, the film was able to reduce the porosity down to 2 %.

Electrochemical impedance spectroscopy was used to investigate the corrosion of magnesium coated with vinyl-triethoxy silane as sol-gel precursor. The resistances R_{SG} and R_{Polar}, derived from EIS, can be used for judging the film's ability for corrosion protection. The increase of these two resistances until 5 hours of immersion time proved the ability of the coating to prevent electrolyte diffusion into the substrate for a certain period of time. The presence of an inter-diffusion layer was again proved by SIMS results.

The adhesion problem between magnesium and zirconia was approached by applying silane coupling agent in combination with the zirconium precursor. SIMS and IR spectroscopy results proved the formation of hetero-linkage of Zr-Si-O. EIS results showed that these coatings are able to improve the corrosion resistance of magnesium sample until 10 hours obtained from an increase in both R_{SG} and R_{Polar} compared to the bare material.

In a series of Tafel experiments the three silicon-based precursors and binary mixtures between them and the zirconium precursor were compared. It turned out that the mixtures gave considerably better results than the pure silicon-based films.

The best result was obtained for a mixture of phenyl-triethoxsilane and zirconium, formed at a moderate temperature of 390 K. While SIMS had shown a film of a ternary compound with Zr, Si, and O, no reflexes of a crystalline compound were obtained in XRD and TEM. The films were amorphous.

It can be concluded that two factors have a dominant effect on the ability of the resulting film to enhance the corrosion resistance of the substrate: the porous nature of sol-gel thin films, and their adhesion to the substrate. It was shown that by varying the concentration of sol solution constituents such as water, catalyst, stabilizing agent and heat treatment temperature, films with less porosity could be obtained which in turn could enhance the corrosion resistance of magnesium. Along with these parameters, it was shown that the type of precursor also plays an important rule on the porosity of the film. From the results, it can be stated that precursor containing unsaturated polymerizable organofunctional groups leads to the formation of less porous film. The best results were obtained when such a precursor was mixed with the zirconium compound, leading to an amorphous chemically stable well-adhering coating with very low porosity. Amorphous structures have no grain boundaries which are often the places of onset of corrosion.

References

1 Y. Kojima, *Mater. Sci. Forum* 350–351 (2000) 3

2 H. Kuwahara, Y. Al-Abdullat, M. Ohta, S. Tsutsumi, K. Ikeuchi, N. Mazaki, T. Aizauta, *Mater. Sci. Forum* 350–351 (2000) 349

3 Y.W. Song, D.Y. Shan, E.H. Han, *Electrochim. Acta* 53 (2008) 2135

4 S. Ishihara, H. Notoya, A. Okada, Z.Y. Nan, T. Goshima, *Surf. Coat. Technol.* 202 (2008) 2085

5 H.W. Huo, Y. Li, F.H. Wang, *Corros. Sci.* 46 (2004) 1467

6 M. Dabala, K. Brunelli, E. Napolitani, M. Magrini, *Surf. Coat. Technol.* 172 (2003) 227

7 C. Blawert, W. Dietzel, E. Ghali, G. Song, *Adv. Eng. Mater.* 8 (2006) 511

8 M. Hara, K. Matsuda, W. Yamauchi, M. Sakaguchi, T. Yoshikata, Y. Takigawa, K. Higashi, *Mater. Trans.* 48 (2007) 3118

9 H. Tsubakino, A. Yamamoto, S. Fukumoto, A. Watanabe, K. Sugahara, H. Inoue, *Mater. Trans.* 44 (2003) 504

10 J. Senf, E. Broszeit, *Adv. Eng. Mater.* 1 (1999) 133

11 S.I. Stupp, P.V. Braun, *Science* 277 (1997) 1242

12 P. Judeinstein, C. Sanchez, *J. Mater. Chem.* 6 (1996) 511

13 P.V. Braun, P. Osenar, V. Tohver, S.B. Kennedy, S.I. Stupp, *J. Am. Chem. Soc.* 121 (1999) 7302

14 I.M. Notter, D.R. Gabe, *Corros. Rev.* 10 (1992) 217

15 B. Enders, A. Rota, H. Bohni, *Surf. Coat. Technol.* 130 (2000) 224

16 J.Z. Li, Y.W. Tian, Z.Q. Huang, X. Zhang, *Appl. Surf. Sci.* 252 (2006) 2839

17 U.R. Evans, *The Corrosion and Oxidation of Metals*, Arnold, London, 12, 1960

18 G.L. Makar, J. Kruger, *Int. Mater. Rev.* 38 (1993) 138

19 M. Pourbaix., *Atlas of Potential/pH Diagrams*; Pergamon, Oxford, 1962

20 M. Pourbaix, *Lectures on Electrochemical Corrosion*; Plenum Press, New York, 1973

21 R.W. Revie, H.H. Uhlig, *Corrosion and Corrosion Control*, John Wiley & Sons, Inc., 2008, Ch. 4

22 G.G. Perrault, *Electroanal. Chem. Interface Electrochem.* 51 (1974) 107

23 S. Ono, *Metallurgical Science and Technology*; Vol. 16, Nos. 1–2, pp. 91–104, 199

24 H. Jones, S. Joshi, R. G. Rowe, F. H. Froes, *Int. J. Powder Metall.* 23 (1987) 13

25 O. Frühwirth, G.W. Herzog, I. Hollerer, A. Rachetti, *Surf. Technol.* 24 (1985) 301

26 P.R. Roberge, *Corrosion Engineering: Principles and Practice*; Mc Graw Hill, New York, 2008

27 J. Wang, *Analytical Electrochemistry*; Wiley, New York, 2006

28 Stern, A.L. Geary, *J. Electrochem. Soc.* 104 (1957) 56

29 R. Tunold, H. Holtan, M.B. Hägg Berge, A. Lasson, R. Steen-Hansen, *Corros. Sci.* 17 (1977) 353

30 E. Ghali, V.S. Sastri, M. Elboujdaini, *Corrosion Prevention and Protection*; Wiley, 2007

31 H. Hessing, H. L. Logan, *Corr. Rev. Control* 2 (1955) 53

32 F. Keller, M.S. Hunter, D.L. Robinson, *J. Electrochem. Soc.* 100(1953) 411

33 K. Huber, *J. Electrochem. Soc.* 100 (1953) 376

34 O. Khaselev, J. Yahalom, *Corros. Sci.* 40 (1998) 1149

35 Y. Mizutani, S. J. Kim, R. Ichino, M. Okido, *Surf. Coat. Technol.* 169-170 (2003) 143

36 F.A. Lowenheim, *Modern Electroplating*; Wiley, New York, 1974.

37 A.K. Sharma, *Metal Finishing* 87 (1989) 73

38 D. Hawke, D.L. Albright, *Metal Finishing* 93 (1995) 34

39 X. Chen, G. Li, J. Lian, Q. Jiang, *Appl. Surf. Sci.* 255 (2008) 2322

40 M.F. Montemor, A.M. Simoes, M.J. Carmezim, *Appl. Surf. Sci.* 253 (2007) 6922

41 F. Pan, X. Yang, D. Zhang, *Appl. Surf. Sci.* 255 (2009) 8363

42 H. Altun, S. Sen, *Surf. Coat. Technol.* 197 (2005) 193

43 G. Wu, X. Zeng, W. Ding, X. Guo, S. Yao, *Appl. Surf. Sci.* 252 (2006) 7422

44 G. Wu, X. Zeng, G. Yuag, *Mater. Lett.* 62 (2008) 4325

45 J. Mazia, *Metal Finishing* 88 (1990) 466

46 R.G. Jacob, *Agric. Eng.* 3 (1992) 26

47 P.Gomez-Romero, C. Sanchez, *Functional Hybrid Materials*; Wiley-VCH, 2003

48 M. L. Zheludkevich, I. Miranda Salvadob, M. G. S. Ferreira, *J. Mater. Chem.* 15 (2005) 5099

49 H. Umehara, M. Takaya, T.I. Tsukuba, *Aluminium* 75 (1999) 634

50 A.R. Phani, F.J. Gammel, T. Hack, H. Haefke, *Mater. Corros.* 56 (2005) 77

51 Q. Li, B. Chen, S. Xu, H. Gao, L. Zhang, C. Liu, *J. Alloy Comp.* 478 (2009) 544

52 J.M. Fan, Q. Li, W. Kang, S. Y. Zhang, B. Chen, *Mater. Corros*. 60 (2009) 438

53 G. Doetsch, *Laplace Transformation*, Dover, New York, 1953

54 E. Warburg, *Ann. Phys. Chem.* 67 (1899) 493

55 T. Pajkossy, *J. Electroanal. Chem.* 364 (1994) 111

56 F. Mansfeld, M. Kendig, S. Tsai, *Corrosion* 38 (1982) 478

57 C. Sanchez, F. Ribot, *New J. Chem.* 18 (1994) 1007

58 P. Judeinstein, C. Sanchez, *J. Mater. Chem.* 6 (1996) 511

59 A.J. Atanacio, B.A. Latella, C.J. Barbe, M.V. Swain, *Surf. Coat. Technol.* 192 (2005) 354

60 D.L. Kepert, *The Early Transition Metals*; Academic press, London, 1972

61 A. Aelion, A. Loebel, F. Eirich, *J. Am. Chem. Soc.* 72 (1950) 5705

62 R. H. Glaser, G. L. Wilkes, *Polym. Bull.* 19 (1988) 51

63 C.J. Brinker, K.D. Keefer, D.W. Schaefer, R.A. Assink, B.D. Kay, C.S. Ashley, *J. Non-Cryst. Solids* 63 (1984) 45

64 I. Strawbridge, A.F. Craievich, P.F. James, *J. Non-Cryst. Solids* 72 (1985) 139

65 R.P.J. Corriu, D. LeCleck, A. Vioux, M. Pauthe, J. Phalippou, in *Ultrastructure Processing of Advanced Ceramics*, J.D. Mackenzie, D. Ulrich (Eds.), p. 113-126, Wiley, 1986

66 J. Livage, M. Henry, C. Sanchez, *Prog. Solid State Chem.* 18 (1988) 259

67 M.D. Sacks, R.S. Sheu, *Science of Ceramic Chemical Processing*; (L.L. Hench, D.R. Ulrich, Eds.), Wiley, New York, 1986, p 102

68 P.J. Flory, *Principles of Polymer Chemistry*; Cornell University Press, Ithaca, NY, 1953; Chapter IX

69 R. Zallen, *The Physics of Amorphous Solids*; Wiley,New York, 1983, Chapter 4

70 A.J. Vega, G.W. Scherer, *J. Non-Cryst. Solids* 111 (1989) 153

71 B.E. Yoldas, *J. Mater. Sci.* 21 (1986) 1087

72 G.W. Scherer, *J. Non-Cryst. Solids* 87 (1986) 199

73 Z.Z. Vysotskii, D.N. Strazhesko, *Adsorption and Absorbents*; (D.N. Strazhesko, Ed.), Wiley, New York, 1973, No. 1, p 55

74 T.K. Sherwood, *Ind. Eng. Chem.* 21 (1929) 12

75 T.K. Sherwood, *Ind. Eng. Chem.* 21 (1929) 976

76 T. Kawaguchi, J. Jura, N. Taneda, H. Hishikura, Y. Kokubu, *J. Non-Cryst. Solids* 82 (1986) 50

77 S. Whitaker, *Advances in Drying*; (A.S. Mujumdar, Ed.), Hemisphere, New York, 1980, Vol. 1, p 23

78 R.K. Dwivedi. *J. Mater. Sci. Lett.* 5 (1986) 373

79 J. Zarzycki, M. Prassas, J. Phalippou, *J. Mater. Sci.* 17 (1982) 3371

80 T.A. Gallo, L.C. Klein, *J. Non-Cryst. Solids* 82 (1986) 198

81 J. Frenkel, *J. Phys.* 9 (1945) 385

82 G.W. Scherer, *J. Am. Ceram. Soc.* 60 (1977) 236

83 J.D. Mackenzie, R. Shuttleworth, *Proc. Phys. Soc. London* 62 (1949) 833

84 B.E. Yoldas, *J. Mater. Sci.* 10 (1975) 1856

85 L.E. Scriven, *Better Ceramics Through Chemistry III*; C. J. Brinker, D.E. Clarke, D.R. Ulrich, Eds.; Materials Research Society: Pittsburg, PA, 1988, pp. 717–729

86 L.D. Landau, B.G. Levich, *Acta Physicochim.* U.R.S.S. 17 (1942) 42

87 Dislich, E. Hussmann, *Thin Solid Films* 77 (1981) 129

88 D.E. Bornside, C.W. Macosko, L.E. Scriven, *J. Imaging Tech.* 13 (1987) 122

89 E.G. Emslie, F.T. Bonner, L.G. Peck, *J.Appl. Phys.* 29 (1958) 858

90 D. Meyerhofer, *J. Appl. Phys.* 49 (1978) 3993

91 S. Hirai, K. Shimakage, S. Aizawa, K. Wada, *J. Am. Cearm.* Soc. 81 (1998) 3087

92 Y. Tamara, D. Mandler, *Electrochim. Acta* 53 (2008) 5118

93 R.R omero Pareja, R.Lopez Ibanez, F. Martin, J.R. Ramos-Barrado, D. Leinen, *Surf. Coat. Technol.* 200 (2006) 6606

94 L. Fedrizzi, F. J. Rodriguez, S. Rossi, F. Deflorianc, R. Di Maggio, *Electrochim. Acta* 46 (2001) 3715

95 K.S. Mazdiyasni, C.T. Lynch, J.S. Smith, *J. Am. Ceram. Soc.* 50 (1967) 532

96 D.C. Bradley, D.G. Carter, *Can. J. Chem.* 39 (1961) 1434

97 D.C. Bradley, D.G. Carter, *Can. J. Chem.* 40 (1962) 15

98 U.B. Saxena, A.K. Rai, V.K. Mathur, R.C. Mehrotra, *J. Chem. Soc. A* (1970) 904

99 G. De, A. Chatterjee, D. Ganguli, *J. Mater. Sci. Lett.* 9 (1990) 845

100 J.C. Pouxviel, J.P. Boilot, *J. Non-Cryst. Solids* 94 (1987) 374

101 R.A. Assink, B.D. Kay, *J. Non-Cryst. Solids* 99 (1988) 359

102 H. Schmidt, *J. Non-Cryst. Solids* 73 (1985) 681

103 B. Arkles, *CHEMTECH* 7 (1977) 766

104 J.F. Hyde, R.C. DeLong, *J. Am. Chem. Soc*. 63 (1941) 1194

105 K.J. McNeil, J.A.DiCaprio, D.A. Walsh, R.F. Pratt, *J. Am. Chem. Soc.* 102 (1980) 1859

106 R.L. Schowen, K.S. Latham Jr., *J. Am. Chem. Soc.* 88 (1966) 3795

107 L. Matejka, O. Dukh, J. Brus, W.J. Simonsick, B. Meissner, *J. Non-Cryst Solids* 270 (2000) 34

108 K. Piana, U. Schubert, *Chem. Mater.* 6 (1994) 1504

109 Y. Park, M. Nagai, *Solid State Ionics* 145 (2001) 149

110 K. Hirata, A. Matsuda, T. Hirata, M. Tatsumisago, T. Minami, *J. Sol-Gel Sci. Technol.* 17 (2000) 61

111 P. Innocenzi, G. Brusatin, F. Babonneau, *Chem. Mater.* 12 (2000) 3726

112 D. Hoebbel, M. Nacken, H. Schmidt, *J. Sol-Gel Sci. Technol.* 12 (1998) 169

113 D. Hoebbel, M. Nacken, H. Schmidt, *J. Sol-Gel Sci. Technol.* 13 (1998) 37

114 M. Templin, U. Wiesner, H.W. Spiess, *Adv. Mater.* 9 (1997) 814

115 G. Schottner, *Chem. Mater.* 13 (2001) 3422

116 Z. Zhan, H.C. Zeng, *J. Non-Cryst. Solids* 243 (1999) 26

117 M. Nogami, *J. Non-Cryst. Solids* 69 (1985) 415

118 A. Maskishima, H. Oohashi, M. Wakakuwa, K. Kotani, T. Shimohria, *J. Non-Cryst. Solids* 42 (1980) 545

119 M. Nogami, M. Tomozawa, *J. Am. Ceram. Soc.* 69 (1986) 99

120 J. B. Miller, E. I. Ko, *Catal. Today* 35 (1997) 269

121 M. Nogami, K. Nagasaka, *J. Non-Cryst. Solids* 109 (1989) 79

122 Z. Zhan, H.C. Zeng, *J. Mater. Chem.* 9 (1999) 2647

123 S. Amelinckx, D. van Dyck, J. van Landuyt, G. van Tendeloo, *Handbook of Microscopy: Applications in Materials Science; Solid-State Physics and Chemistry*, Wiley, USA, 1996

124 L.S. Birks, *Wavelength dispersion*; In: H.K. Herglotz, L.S. Birks, (Eds.) X-Ray Spectrometry. New York: Marcel Dekker, Inc., 1978

125 R. Ugas-Carrión, F. Sittner, M. Yekehtaz, S. Flege, J. Brötz, W. Ensinger, *Surf. Coat. Technol.* 204 (2010) 2064

126 C.J. Brinker, A.J. Hurd, P.R. Schunk, G.C. Frye, C.S. Ashley, *J. Non-Cryst. Solids* 147-148 (1992) 424

127 A.J. Evans, M,D. Dory, and M.S. Ru, *J. Mates. Res.* 3 (1988) 1043

128 E. P. Plueddemann, *J. Adhesion* 2 (1970) 184

129 E.J.A. Pope, J.D. Mackenzie, *J. Non-Cryst. Solids* 87 (1986) 105

130 S. Doeuff, M. Henry, C. Sanchez, J. Livage, *J. Non-Cryst. Solids* 89 (1987) 206

131 R. Aelion, A. Loebel, F. Eirich, *J. Am. Chem. Soc.* 72 (1951) 5705

132 N.B. Colthup, L.H. Daly, *Introduction to Infrared and Raman Spectroscopy*, 2nd Ed.; Academic Press, New York, 1975, p 257

133 Y.S. Li, Y. Wang, S. Ceesay, *Spectrochimica Acta Part A* 71 (2009) 1819

134 H. Ishida, J.L. Koenig, *Appl. Spectros.* 32 (1978) 469

135 J.G. Grasselli, W.M. Ritchey (Eds.), *Atlas of Spectral Data and Physical Constants for Organic Compounds*, Vol. I.; Cleveland, CRC Press Inc., 1975

136 G. Brusatin, P. Innocenzi, M. Guglielmi, R. Signorini, R. Bozio, *Nonlinear Opt.* 27 (2001) 259

137 P. Innocenzi, A. Sassi, G. Brusatin, M. Guglielmi, D. Favretto, R. Bertani, A. Venzo, F. Babonneau, *Chem. Mater.* 13 (2001) 3635

138 G. Brusatin, P. Innocenzi, M. Guglielmi, F. Babonneau, *J. Sol–Gel Sci. Technol.* 26 (2003) 303

139 R. Guo, C. Hu, F. Pan, H. Wu, Z. Jiang, *J. Membr. Sci.* 281 (2006) 454

140 Y.S. Li, P.B. Wright, R. Puritt, T. Tran, *Spectrochimica Acta Part A* 60 (2004) 2759

141 H. Ishida, J.L. Koenig,, *J. Colloid Interface Sci.* 64 (1987) 555

142 A. Bertoluzza, C. Fagnano, M.A. Morelli, V. Gottardi, M. Guglielmi, *J Non-Cryst Solids 48* (1982) 117

143 R.C. Lord, D.W. Robinson, W.C. Schumb, *J. Am. Chem. Soc.* 78 (1956) 1327

144 D.L. Ou, A.B. Seddon, *J. Non-Cryst Solids* 210 (1997) 187

145 N. Pebere, C. Riera, F. Dabosi, *Electrochim. Acta* 35 (1990) 555

146 G. Baril, N. Pebere, *Corros. Sci.* 43 (2001) 473

147 I.V. Aoki, M.C. Bernard, S.I. Cordoba de Torresi, C.Deslouis, H.G. de Melo, S. Joiret, B. Tribollet, *Electrochim. Acta* 46 (2001) 1871

148 C.S. Hsu, F. Mansfeld, *Corrosion* 57 (2001) 747

149 J. Kang, G.S. Frankel, *Z. Phys. Chem.* 219 (2005) 1519.

150 J. Kang, *Electrochemical Studies of Coatings and Thin Films*, Ph.D. Thesis, Ohio State University, 2006.

151 Z. Dang, B.G. Anderson, Y. Amenomiya, B.A. Morrow, *J. Phys. Chem.* 99 (1995) 14437

152 I.M. Miranda Salvado, C.J. Serna, J. M. Fernandez Navarro, *J. Non-Cryst. Solids* 100 (1988) 330

153 S. Ricol, E. Vernaz, P. Barboux, *J. Sol-Gel Sci. Technol.* 8 (1997)229

154 P.P. Bihuniak, R.A. Condrate, *J. Non-Cryst. Solids* 44 (1981) 331

Publications and Conferences

The following articles in peer-reviewed journals and conferences have been derived and attended during the Ph.D. research:

1 - C. J. Ochs, F. Sittner, R. Ugas-Carrión, M. Yekehtaz, W. Ensinger; Structural and electrochemical characterization of zirconium and silicon based sol-gel coatings for corrosion protection, *Current Topics in Electrochemistry* **13** (2008) 59-65

2 - M. Yekehtaz, K. Baba, R. Hatada, S. Flege, F. Sittner, W. Ensinger; Corrosion resistance of magnesium treated by hydrocarbon plasma immersion ion implantation, *Nucl. Instrum. Meth. B* **267** (2009) 1666-1669

3 - M. Yekehtaz, F. Sittner, R. Ugas-Carrión, S. Flege, J. Brötz, W. Ensinger; Characterization of protective sol-gel coatings on magnesium based on phenyl-triethoxysilane precursor, *Thin Solid Films* **518** (2010) 5223–5226

4 - R. Ugas-Carrión, F. Sittner, M. Yekehtaz, S. Flege, J. Brötz, W. Ensinger; Influence of stabilizing agents on structure and protection performance of zirconium oxide films, *Surface and Coating Technology* **204** (2010) 2064-2067

5 - Corrosion resistance of magnesium treated by hydrocarbon plasma immersion ion implantation'' presented at the 16th International Conference on Ion Beam Modification of Materials, Dresden, Germany, August 31-September 5, 2008

6 - Characterization of protective Sol-Gel coatings on magnesium'' presented at the European corrosion congress, EuroCorr 2009, Nice, France, September 6-10, 2009

Curriculum Vitae

Personal Information

Name:	Mehdi Yekehtaz
Birthday:	13.08.1976
Birthplace:	Tehran
Nationality:	Iran

Education:

1995-1999	Bachelor degree of Pure Chemistry at Imam Khomeini International University (IKIU), Qazvin, Iran
1999-2001	Master degree of Analytical Chemistry at Institute for Advance Studies in Basic Sciences, Zanjan, Iran **Master Thesis:** Determination of trace amounts of some heavy metals by Adsorptive & Anodic Stripping Voltammetry
2006-2010	Ph.D. degree at Technical University of Darmstadt, Darmstadt, Germany **Ph.D. Thesis:** Evaluation of Porosity and Corrosion Protection Ability of Sol-Gel Deposited Oxide Thin Films on Magnesium
From March 2010	PostDoc position in Corrosion Group of Dr. W. Fuerbeth at DECHEMA e.v., Frankfurt, Germany

Eidesstattliche Erklärung

Hiermit erkläre ich an Eides statt, dass ich diese Dissertation selbständig und nur mit den angegebenen und erlaubten Hilfsmitteln angefertigt habe.

Ich habe bisher noch keinen Promotionversuch unternommen.

Darmstadt, den 23.08.2010